# Hard Carbon Anode Materials for Sodium-ion Battery

Zur Erlangung des akademischen Grades eines DOKTORS

DER NATURWISSENSCHAFTEN (Dr. rer. nat.)

der Fakultät für Chemie und Biowissenschaften des Karlsruher

Instituts für Technologie (KIT) genehmigte

DISSERTATION von

**Xinwei Dou**

1. Referent: Prof. Dr. Stefano Passerini

2. Referent: Prof. Dr. Helmut Ehrenberg

Tag der mündlichen Prüfung: 11.12.2018

There are three things extremely hard: steel, a diamond and to know one’s self.

---- Benjamin Franklin

# Table of Contents

# 1. Abstract

Lithium-ion batteries (LIBs) are one of the most important innovations within the last 30 years. Their success accelerated the development in many other industrial fields, such as mobile communication, personal computers, and electric vehicles. However, the massive demand of LIBs exerts high pressure on raw material supplies resulting in the price of lithium rapidly increasing. Thus, sodium, a much cheaper and more abundant element, becomes a reasonable and sustainable alternative to lithium for the large deployment of batteries for large-scale storage applications. Meanwhile, sodium ion batteries (SIBs) and LIBs share the same working principle, which makes the production of SIBs easy to scale-up to large volumes using the well-established LIB production technology.

One of the remaining challenges for the SIBs commercialization is the lack of suitable materials for the negative electrode. Graphite, the most commonly used anode material in LIBs, shows poor electrochemical performance in SIBs. Hard carbon (non-graphizatible carbon) - especially the one derived from biomass waste - due to the relatively low cost and good electrochemical performance is the most promising anode material in SIBs. However, there are still challenges to be overcome for commercialization of hard carbon as anode in SIBs, including both the structural understanding and the $Na^+$ storage mechanism.

In this thesis, three activities lines are pursued to understand the electrochemical performance of hard carbons in SIBs. First, the impact of the biomass precursors on the formed hard carbon is investigated to correlate the nature of the biomass waste

with the performance of the resulting hard carbon as anode in SIBs. Second, the impact of porosity is investigated to reveal the importance and the correlation of the closed porosity on the electrochemical performance of hard carbons. Finally, the impact of the acid treatment, i.e., the biomass pre-treatment method, is studied to further understand the correlation between hard carbon structure and sodium storage mechanism. These studies aim to allow the synthesis of sustainable and low-cost hard carbon anode materials with good electrochemical performance for SIBs.

# Zusammenfassung

Die Entwicklung der Lithium-Ionen-Batterie (LIBs) zählt zu den bedeutendsten Errungenschaften der vergangenen 30 Jahre und Ihre Erfolgsgeschichte spiegelt sich vor allem bei Mobilfunkgeräten, Notebooks und in der Elektromobilität wieder. Aufgrund der stetig wachsenden Nachfrage an LIBs kann es in Zukunft jedoch zu Engpässen bei der Lieferung der Rohmaterialien kommen, welche beispielsweise den Preis für Lithium treiben. Im Gegensatz dazu ist Natrium häufiger in der Erdkruste vorhanden und dementsprechend günstig, wodurch Batterien basierend auf Natrium (Sodium-ion batteries, SIBs) als Ladungsträger zu den nachhaltigen und preiswerten Alternativen gelten. Da beide Technologien auf dem gleichen Funktionsprinzip basieren könnten SIBs in bereits vorhandener Infrastruktur produziert werden, was eine Kommerzialisierung zusätzlich erleichtert.

Eine der größten Herausforderungen für eine erfolgreiche Kommerzialisierung von SIBs ist jedoch, geeignete Aktivmaterialien für die negative Elektrode zu identifizieren. Graphit, das Standard Aktivmaterial in LIBs, kann aufgrund seines niedrigen Potentials und der Größe des Natrium Ions nicht verwendet werden. Hard Carbons (Nicht graphitierte Hartkohlenstoffe), speziell jene gewonnen aus Bioabfällen, sind aufgrund ihrer geringen Anschaffungskosten und der guten elektrochemischen Leistungsfähigkeit die vielversprechendsten Kandidaten für Anodenmaterialien in SIBs. Dennoch müssen für eine kommerzielle Anwendung zunächst verbleibende Herausforderungen wie beispielsweise das genaue Verständnis der Struktur oder der elektrochemische $Na^+$ Speichermechanismus überwunden werden.

Im Rahmen dieser Arbeit werden Hard Carbons im Hinblick auf ein besseres elektrochemisches Verständnis mit dem Fokus auf drei Parameter untersucht.

Zunächst werden unterschiedliche Hard Carbons, gewonnen aus diversen Bioabfällen, charakterisiert, um den geeignetsten Kandidaten zu identifizieren. In einem zweiten Schritt wird der Einfluss der Porosität des Materials im Ganzen, und speziell der Zusammenhang zwischen geschlossenen Poren und der elektrochemischen Leistungsfähigkeit untersucht. Im letzten Teil wird der Einfluss der Säurebehandlung, einem Vorbehandlungsschritt bei der Synthese von Hard Carbons, im Hinblick auf das bessere Verständnis des Zusammenhangs zwischen Struktur des Materials und seinem $Na^+$ Speichermechanismus untersucht. Alle drei Studien zielen darauf ab, in Zukunft nachhaltige, kostengünstige und vor allem leistungsfähige Hard Carbons als Anodenmaterialien für kommerzielle Natrium-Ionen Batterien zu entwickeln.

# 2. Introduction

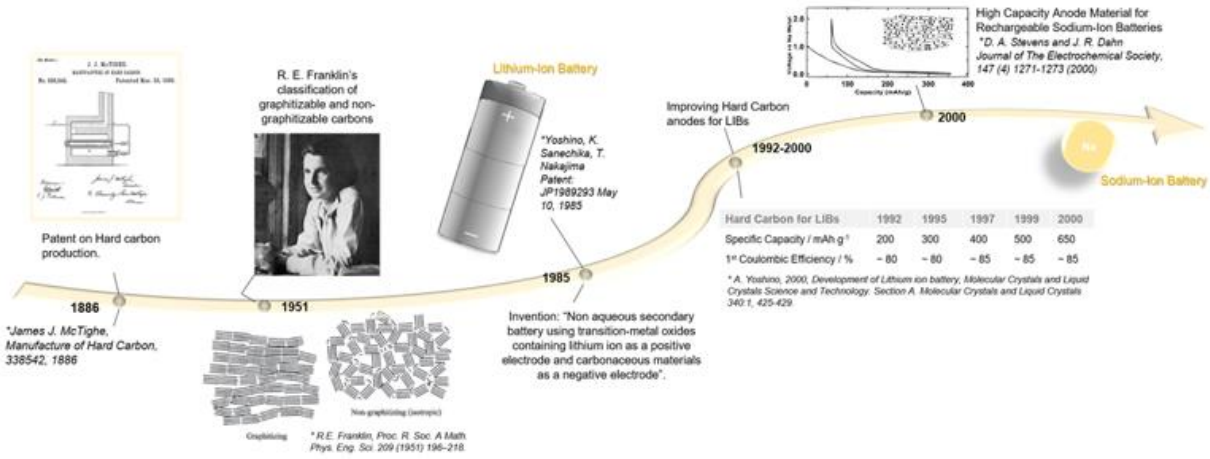


**Table of Content:** Hysterical development of hard carbons.

Rechargeable alkali metal-ion batteries, such as lithium-ion batteries (LIBs) [1], sodium-ion batteries (SIBs) [2] and potassium-ion batteries (PIBs) [3], are widely regarded as the most promising and efficient electrochemical energy storage systems. Particularly, LIBs are considered as one of the most successful innovations in the last thirty years [4–7]. However, the rapidly increasing cost of the raw materials employed in LIBs, *i.e.* cobalt, copper and lithium [8], recently motivated researchers' interest toward technologies using cheaper, abundant as well as evenly distributed resources, *i.e*. SIBs [9–11] and PIBs [12,13]. All three technologies share the same working principle, involving the reversible shuttle of alkali ions between two host electrodes through an electrolyte medium conducting the alkali ions. Such a similarity enabled the direct transfer of the broad experience and knowledge gained on LIBs within the past thirty years, to SIBs and PIBs technologies [12,14,15]. While PIBs are presently at a very early stage of research, there is now substantial evidence that SIBs may represent the future electrochemical energy storage system of choice for large-scale stationary

applications where cost and availability of materials are critical parameters to take into account. Indeed, some pioneering companies and research networks such as the Japanese Sumitomo [16], the English Faradion [17] and the French RS2E network [18] started to demonstrate the feasibility of the technology by producing non-aqueous, large-scale SIBs.

Recently, significant advances have been made in the development of advanced materials for application in SIBs, as highlighted by the increasingly growing number of scientific publications in the research field. A relevant number of suitable materials have been identified including cathodes [19–24], anodes [9,25–28] and electrolytes [29–32].

At the negative electrode, carbon based materials always play a fundamental role for alkali ion batteries. Carbon and its allotropes represent an intriguing class of compounds, characterized by low cost, large abundance and uniquely tunable electronic and structural properties. The implementation of graphite as anode material in LIBs represented the turning point for the LIB technology, which represents one of the greatest successes in the field of electrochemical energy storage devices. In 1980 J. Goodenough filed his patent on $LiCoO_2$ as a lithium intercalation cathode material [33], while only one year after, in 1981 at Sanyo, H. Ikeda, was the first to patent the use of graphite as a lithium intercalation material in organic solvent-based electrolytes [34]. The golden combination was close to be achieved and in 1991 Sony Energytec Inc. began to produce commercial cells based on the Asahi patents [35].

Nowadays LIBs are regularly produced with graphite as negative electrode active material, characterized by low toxicity, acceptable price and high abundance. In contrast, the use of graphite as anode in SIBs has been so far inhibited by the inability of sodium (Na) ions to form binary graphite intercalation graphite (b-GICs). The higher ionic radius of Na when compared to lithium (Li) does not represent an obstacle for

intercalation, indeed larger alkali ions such as potassium (K), cesium (Cs) and rubidium (Rb) have demonstrated the ability to form b-GICs [36–38]. Na is being an exception [39,40], most likely due to the lower energetic stability of Na-GICs and formation potentials calculated to be below that of sodium metal [36,41–43].

It has been reported that only the formation of stage eight Na-GICs ($NaC_{64}$) is occurring by applying extreme conditions, while lower stages were prepared by controlling the amount of impurities in graphite, the temperature and pressure applied. However, only low electrochemical activity in Na cells has been reported[44–46]. More recently, it has been found that graphite can be used in Na cells by employing glyme-based electrolytes, enabling the formation of ternary GICs via the co-intercalation of solvated Na ions, exhibiting excellent reversibility at low overpotentials and superior power performance [39,40,47], but limited capacity. In search of high energy density anode materials, alloying, conversion and mixed alloying-conversion type electrodes have been proposed [9,25,26,48].

Among them, silicon represents the next generation anode of choice of LIBs in view of the low-cost and high specific gravimetric and volumetric capacity [49,50]. However, the few reports on the use of silicon in SIBs indicate that silicon exhibit poor electrochemical performance [51,52].

For the above mentioned reasons, the anode of choice in the most common configuration of SIBs is represented by non-graphitizable carbon, generally called “hard carbon” [27,53–56]. Hard carbon was successfully studied also for application in LIBs, indeed the Sony Corporation‘s second generation LIBs included hard carbon at the negative electrode to be later replaced by graphite in the third generation LIBs [7,57].

In the past, numerous studies have been performed to investigate the interactions between carbon materials and sodium. The primary goal was to understand the

behaviour of carbon cathodes in the aluminium smelting process [58]. Indeed, the ability of carbon to store sodium ions was originally investigated as the process occurs during the standard industrial method for aluminium smelting employing the Hall-Heroult reduction cell. In fact, it was observed that sodium could interact with carbon causing carbon-electrode blocking, eventually leading to electrode swelling. This unwanted process, known as tap-out, constituted one of the major safety issues during operation. Thus, a more fundamental understanding of the interaction between carbon and sodium was of primary importance to avoid production inefficiency, costs increase and safety concerns. [58–60]

In the recent years, hard carbon has drawn great attention for application as anode material in SIBs, which is demonstrated by the numerous research articles and review papers published [56,61–69]. Up to date, hard carbon represents the most promising negative electrode for SIBs due to its high storage capacity and cycling stability. Besides, hard carbon can be obtained from environmentally friendly, cheap and renewable bio-sources [70–72], which represents a great advantage in terms of costs as well as large scale production and commercialization.

Despite several promising materials being proposed and tested, a basic comprehension of the sodium storage mechanism, the ion transfer processes and the SEI stability combined with the electrolyte interaction is still missing. The driving force of the vivid ongoing scientific discussion is certainly linked to the uncertainties about the hard carbon's structure, which extend to the interaction between sodium ions and carbon.

Several models have been proposed trying to link the structural and morphological properties of hard carbons with the observed electrochemical behaviour. However, despite the great efforts done toward a more fundamental understanding, still a

universal storage mechanism has to be proposed. The difficulty in developing such a universal model originates from the discrepant observations made by researchers, using different characterization tools to investigate carbon structures, which led to different interpretations of the gained knowledge. The introduction part is a comprehensive overview on the basic definition and structural models of hard carbons proposed so far as well as the most useful state-of-the-art characterization techniques available. The interpretation and limits of the analysis are discussed in relation to the structural analysis and electrochemical behaviour in sodium cells. In addition, the sustainability of hard carbon materials is examined as a fundamental parameter for the future large scale production of hard carbons. Finally, an overview of the remaining challenges and associated perspectives is given in the conclusion part.

## 2.1 Definition, synthesis and structure of hard carbons

### 2.1.1 Definition and terminology related to hard carbons

Hard carbon received its popular name due to its mechanical hardness compared with soft carbon, leading to the common use of these expression in early academic and patent literature [73]. Rosalind Franklin's made one of the greatest scientific contributions toward the understanding of carbon structures. In 1942 she joined the British Coal Utilisation Research Association, being involved in a research program aimed at understanding the structure of coal through density and porosity studies [74]. In 1950 she began the X-ray diffraction (XRD) studies on the graphitization process of carbons being the first one to study the process at temperatures up to 3000 °C [75,76]. Franklin's contribution to the definition and nomenclature of carbons was among the most influential without any doubt. Her studies led to the demonstration that carbon

materials prepared by pyrolysis of organic compounds can be generally classified into two main categories, namely, graphitizable and non-graphitizable carbons [77].

Nowadays, the terminology “hard” carbon is used to describe carbonaceous materials which do not transform into graphite even at temperatures higher than 3000 °C. The definition of “non-graphitizable carbon” is generally used synonymously [78]. It is worth noting that carbons with high mechanical hardness can be graphitizable while non-graphitizable carbons may also be very soft. For example, the carbon electrode used in aluminium production cells is an extremely hard material, but still graphitizable.[79]

Besides “hard-” and “non-graphitizable-” carbons, several alternative terms are commonly used in literature to describe these materials, such as amorphous-, disordered-, non-organized and non-graphitic carbon. The rich terminology employed, according to the different research fields in which they are employed, has generated in the years mismatching definitions with respect to the related carbon structures. For instance, despite non-graphitizable carbons do not reveal a long range ordered structure, the term “amorphous” carbon cannot be used to describe non-graphitizable carbons, as the term amorphous is restricted to carbon materials which comprise localized π-electrons according to the description of the Nobel laureate Philip Warren Anderson [79,80]. An example of amorphous carbons are diamond-like carbon films (DLC), which are also named “hard amorphous carbons”. The term “non-graphitic” has a broader meaning than “non-graphitizable” since graphitizable carbons are, as a matter of fact, non-graphitic before graphitization. Thus, this term should be avoided for describing specific non-graphitizable carbons/hard carbons.

### 2.1.2. Hard carbon formation: The carbonization process

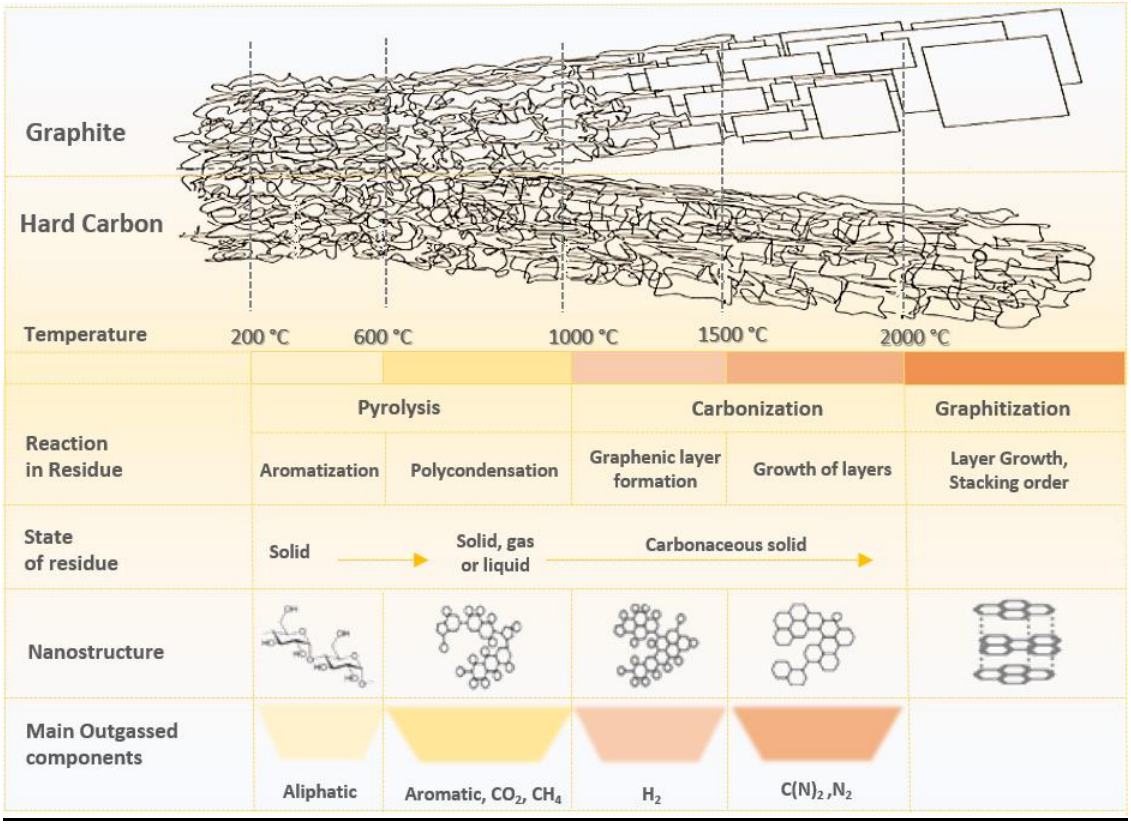


**Figure 2-1.** Hard-carbon formation scheme in relation to temperature. Idea and illustration is strongly based on and derived from Marsh et al. [79]. The circle-like placeholders in the polymeric-structure schemes represent moieties like functional groups and side chains.

In the electrochemical energy storage systems research field, hard carbons are mainly obtained by a thermal [81] or chemical [82] process of pure organic compounds or biomass derived precursors. Precursors such as macromolecular polymeric structures (natural or synthetic) decompose under increased annealing temperatures. This process is generally defined carbonization since it involves an increased relative carbon content in the material. Upon carbonization of the precursors, small molecules such as $H_2O$, $CO_2$ and $N_2$ among others are released [83,84] (see **Figure. 2-1**), often leading to materials characterized by high porosity (1,000 $m^2\ g^{-1}$) [84], low true density (mass over the bulk volume including open and closed pores [85]) of about 2.0 g $cm^{-3}$ [71,77,86] and low bulk density (mass of a solid particle divided by its volume excluding open and

close pores[85]) of about 1.5 g $cm^{-3}$ [87], alongside with the retention of the original polymeric structure. It is important to consider that the nature of the pores created upon carbonization is not necessarily open, especially if the process is conducted at high temperatures (>1200 °C), which leads to decreased BET (Brunauer, Emmett and Teller) surface areas (<<50 $m^2$ $g^{-1}$) [83,88]. The carbonization is a complex process with several concurrent reactions such as dehydrogenation, condensation, hydrogen transfer and isomerization (see **Fig. 1**). Moreover, the macromolecular and partially polymeric structure of the precursor for non-graphitizable carbons persists and does not convert into a fluid phase upon heat treatment as in the case of graphitizable carbons [84]. Consequently, the structure of the derived hard carbon has more or less the same morphology of the parent material, but with lower bulk density. A reported example interestingly shows the morphology replication of hard carbon obtained by pyrolysis of walnut shells (see **Fig. 2**) [89].

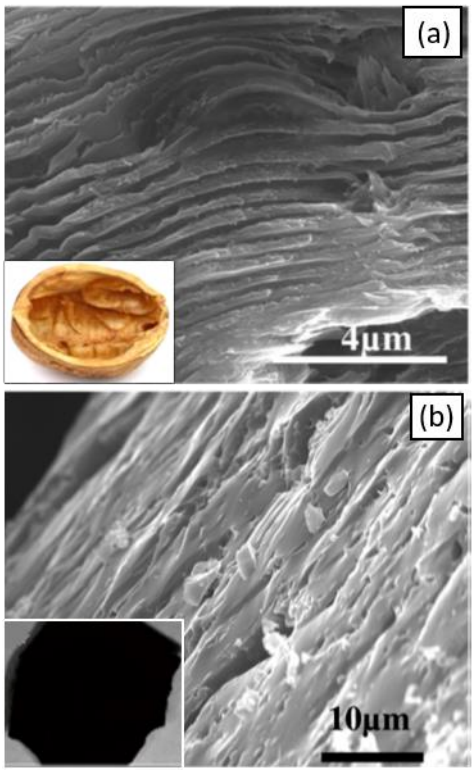

**Figure 2-2.** (a) Walnut shell used as a precursor for hard carbon and related cross sectional morphological image. (b) Derived hard carbon after pyrolysis at 1000 °C with retained morphological features. Adapted from Ref. [89] and reproduced with permission of Copyright © 2017 from American Chemical Society.

The solid-phase carbonization process, which finally produces hard carbons, ceases when the heat treatment is stopped. Increasing heat treatment temperature (HTT) generally results in the formation of progressively more stable internal structures. The structure of a carbon obtained at a defined HTT can be considered as “frozen” at that HTT [79]. Thus, very different carbon materials can be obtained from the same precursor, which gives a valid reason to explore different carbonization conditions for the obtainment of carbon materials with specific structural and morphological properties [83,90,91].

Upon carbonization, i.e., during the decomposition process of the macromolecular structure of the precursors, some carbon atoms present a degree of mobility (< 1 nm), which enables atomic reorganization (e.g., formation of six-membered ring systems) in turns conferring greater stability to the overall carbon network. The obtained atomic configuration, which also include the presence of eventual heteroatoms such as hydrogen and oxygen, constitutes the new carbon network, which constitutes the structure of the obtained carbons. The latter one is certainly dependent on the initial precursor. Every different precursor decomposes in a different way by reaching a more stable energetic configuration through carbon migration, co-bondings creation and vacancies formation by heteroatoms evolution. The new spaces (of atomic dimensions) created by the aforementioned phenomena constitute the porosity of the new carbon network. The commonly accepted nomenclature to define porosity is related to the

dimension of the pores. The latter ones are defined microspores and mesopores when their dimensions are respectively < 2.0 nm and < 50.0 nm. However, recently, particularly in the alkali-ion battery research field, the type of porosity created in non-graphitizable carbons is generally referred as nanoporosity, which is characterized by pore size < 1.0 nm and is responsible of the activated diffusion processes of alkali ions [79].

Differently from porous non-graphitizable carbons, mainly produced by solid-phase carbonization, graphitizable carbons are produced by gas or liquid-phase carbonization of aromatic compounds or polymers generally leading to essentially non-porous carbons. As a result, graphite has a significantly higher true density (e.g., 2.25 g $cm^{-3}$) than non-graphitizable carbons.

### 2.1.3. Structure of hard carbons

Hard carbons, as already indicated by the name, present a significantly high degree of mechanical hardness. The reason is found in the structural properties of these materials, generally retaining the precursor morphology to a high degree [84].

Hard carbons are indeed generally obtained by precursors presenting a strongly cross-linked structure, which even after high temperature treatment will not allow the formation of graphitic structure, conferring isotropic structure to the final product. The degree of crosslinking depends on the state of aggregation of the intermediate phase during pyrolysis. After the carbonization step, involving the graphenic layer formation and successive stacking, (see **Figure. 2-1**) the graphenic sheets cannot be unfolded or flattened to increase the stacking of graphenic lamellae[84,86]. Stevens and Dahn described these regions as aromatic fragments with lateral dimensions of 40 Å stacked with multiple layers (2 to 3) parallel to each other[56], while Liu et al. proposed the

presence of 3 to 5 layers of small graphene sheets stacked randomly [92]. In 1951, R. Franklin [77] reported that the number of layers may range between 2 and 4, which further increases up to 11 at pyrolisis temperatures higher than 3000 °C. The layers are characterized by an extensive interlayer cross-linking, with the links already being created at temperatures lower than 1000 °C [77]. Although the precise nature of the cross-linking has not been identified in depth yet [93], it is assumed that covalent C-O-C bonds are playing a major role and are responsible of the hardness and inability to graphitize.[84]

Macroscopically, the structure of hard carbon can be described by discrete fragments [93] of non-planar[84] curved [86,93,94] bent[84] buckled[87] twisted[84,93] and rumpled [86] graphenic sheets. It has been reported that the average radius of curvature for graphene sheets is about 16 Å [95]. The graphene layers cannot be unfolded or flattened [86], but are partially stacked due to the existence of van der Waals forces [93]. The orientation of the graphene layers is therefore, despite the partial stacking, rather randomic[56] and turbostratic[86], resulting in voids [86] and pores [84] in a wide range of size and forms[84].

Further attempts to describe the structure of hard carbons proposed that the carbon lamellae could be potentially better described as fullerene-like structures[96] consisting of $sp^2$-hybridized carbon[84] in a network of hexagons, partially disrupted by pentagons and heptagons[93] as well as defects. J.M. Stratford et al. reported a relatively small concentration of these features[95] while the presence of a high concentration of $sp^3$-hybridized carbons in the inter-layer bonding region is still under discussion[96]. Furthermore, the graphenic/fullerenic sheets may also present other types of defects and distortions like single anddouble vacancies, (inverse) Stone-Thrower-Wales defects and adatoms[97–100] as well as (interstitial) heteroatoms (e.g., H, B, N, O, S, P) [84,86,99,101,102] and empty sites[103], destroying the regularity of the graphenic sheets

[84,86,97,99,100,102,104]. It is worth mentioning that despite the existence of these defective features, which are responsible of structural inhomogeneity when compared to graphitic like structure, the lamellae are smaller in size, ranging from 5 to 500 nm, making hard carbon more anisotropic than soft carbon. Moreover, graphenic layers might be additionally linked over short distance by chains and “bridges” as a results of interlayer double vacancy (Wigner defects) [98,100,105], which may further contribute to the non-graphitizable behaviour[84].

Having in mind the structural complexity of these materials, hard carbons have been described as “carbon-carbon composites”[106], “carbon alloys”[107] or carbon allotropes[86] with nanodomains (<500 nm) of small ordered volumes (pseudo-graphitic, high degree of anisotropy), alongside with larger disordered (isotropic) regions[84]. In addition, hard carbons also exhibit a complex “crystalline” nature, texture (influencing the material’s processability and density), micro/meso/macro structure (resulting in numerous variants for stacking degree and pores), and overall morphology.[107]

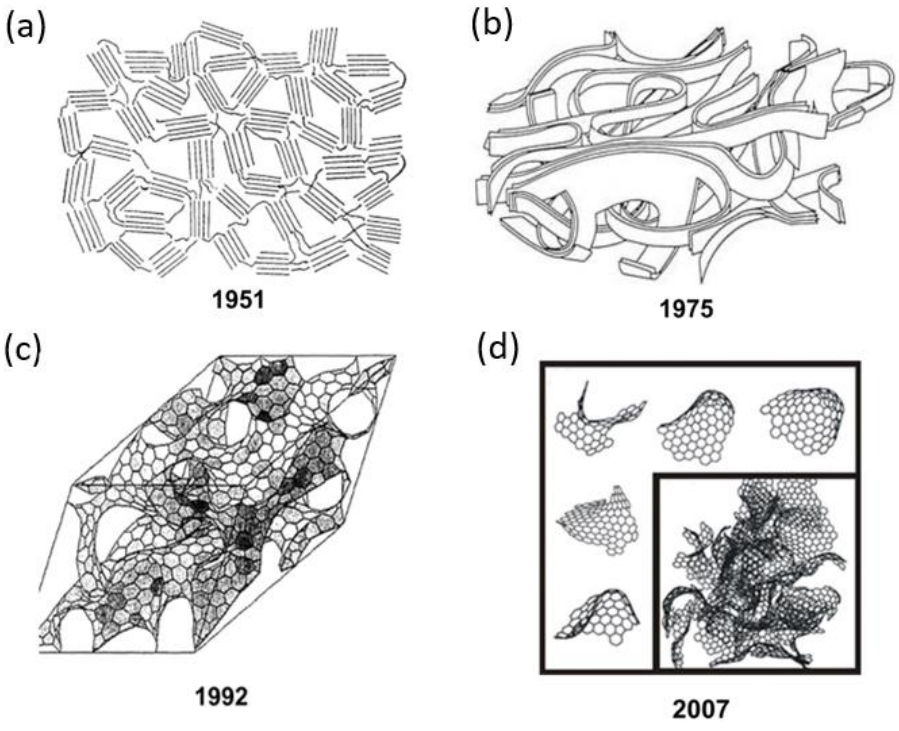

**Figure 2-3.** A selection of models/schemes/illustration of the (atomic) structure of hard carbon with the year of publication. (a) Franklin [77], reproduced with permission of Copyright © 2017 The Royal Society. (b) Ban et al. [108], reproduced with permission of Copyright © 2007, John Wiley and Sons. (c) Townsend et al. [109] reproduced with permission of Copyright © 1992 The American Physical Society, d) Terzyk et al.[110] reproduced with permission of Copyright © 2007 Royal Society of Chemistry.

Attempts to graphically represent the structural features of hard carbon have been made by R. Franklin since 1951 (see **Figure. 2-3a**)[77]. However, the complex structures more recently observed are insufficiently represented by this 2D depiction of planar sheets. More advanced 3D models have been presented showing the nature of fullerenic/graphenic-lamellae ordering more properly (see **Figure. 2-3(b-d)**)[74,96,111]. It is worth mentioning that during the years several other structural models have been proposed[112,113], each of them emphasizing different properties. One of the key properties of these structures is without any doubt the porosity, however, the definition of a structural model taking into account the complex nature of porosity in hard carbon is still under discussion.

Until today, one of the greatest mainstay in this regard, is the “house of cards” (or “falling cards”) model, which has been developed by Dahn *et al.*[56,62,78,112] to describe the lithium and sodium storage mechanism into hard carbons. The “house of cards” model is actually based on two aspects. The first deals with the development of a conceptual model to describe the structure of carbons[112]. The second aspect concerns the description of the Li/Na storage mechanism in these hard carbons, when serving as electrode material for LIBs or SIBs[56,78,114]. With respect to the first aspect, the “house of cards” model states that hard carbons are comprised of a combination of

graphite-like micro-crystallites (*i.e.*, parallel graphene layers; $sp^2$-hybridized) and amorphous regions (edges, defects of the graphene layers; $sp^3$-hybridized). However, it is worth mentioning, that nowadays uuncertainties and open discussions are related to the presence of graphitic crystallite domains within the hard carbon structure. For instance, D. M. Ruthven [115] described these domains as elementary crystallites of graphite stacked in random orientation creating spaces defined as porosity. On the other hand, H. Marsh suggested that, despite the model proposed by Dahn et al. makes a link between porosity and structure, its assumptions have to be reconsidered[79].

Indeed, Marsh suggests that the theory involving the existence of graphitic crystallites is more suitable for the description of graphitic carbons such as carbon black rather than non-graphitizable carbons (hard carbons). Marsh suggested that non-graphitizable carbon should be defined as carbons that never exhibit three dimensional XRD lines (hkl) at any carbonization temperature. According to his definition, the theory of graphitic crystallites is inert to explain the structure of carbons obtained at low carbonization temperature. Indeed, as an example, carbons obtained at low heat treatment temperature (HTT) such as 500 °C, show similar broad XRD peaks as carbons obtained at 1000 °C. However considering that at 500 °C graphitic structure cannot be formed, he proposes that broad XRD peak of hard carbons is caused by the curvature and imperfect layering of the highly defective micro-graphene layers.

### 2.2. Analysis of hard carbons

The structural and morphological features of carbon-based materials for application in electrochemical energy storage systems has been investigated using several

analytical techniques [116]. For the specific case of hard carbons used in SIBs, one of the greatest challenge is the fundamental understanding of the sodium storage mechanism and the associated structural changes [117]. Both ex-situ and in-situ bulk and surface sensitive characterization techniques have been largely reported for the characterization of the sodiation process. However, controversial interpretations (or misinterpretations) of the several characterization methods, most frequently offering complementary information gained under different experimental conditions, persists, making very difficult the definition of a universally accepted reaction mechanism. Accordingly, in the following section an overview on the most powerful techniques is given with a focus on the main information delivered by their application as well as a guideline for the interpretation of their results.

### 2.2.1. Gas-adsorption/desorption

Gas adsorption/desorption is a classical method to investigate two key materials' properties, i.e., porosity and surface area. However, it is worth mentioning that there is not a clear model for the porosity in hard carbons thus, there is no direct method to measure their porosity and surface area [79], since the analysis based on gas sorption/desorption isotherms uses simulations. Therefore it is very important to exercise some care while using a model or a theory to describe the investigated system, indeed every theory has some limitations and specific boundary conditions which have to be taken into account when investigating specific individual materials [115,118]. The BET method is widely used for analyzing the surface area of carbonaceous materials. However, two carbon materials with the same BET surface area could show different adsorption isotherms. For this reason, in a comparative study, it is important to always present the adsorption isotherms alongside with the BET values.

The porosity values obtained from gas adsorption isotherms are generated by the adsorption of gas molecules on the material's surface. Different gas molecules show different adsorption behaviors and some pores may be inaccessible for nitrogen ($N_2$) but "open" for helium (He). Ionic species (Li or Na ions) can diffuse through the solid phase of hard carbon and accumulate into "closed pores". As a matter of the fact, a patent from the Panasonic Corporation reveals that the "closed pores" in gas adsorption/desorption measurement have a strong effect on the sodium storage performance at low potentials[119]. A study on pectin-free apple pomace derived carbon as SIB anode confirmed the trend[120]. Consequently, the porosity values from gas adsorption measurements should be transferred with care into the electrochemical studies.

### 2.2.2. High-resolution Transmission Electron Microscopy (HR-TEM)

HRTEM is a very powerful tool for the investigation of nanoscale features of hard carbon's structure. **Figure 2-4a** displays a HRTEM micrograph of a typical hard carbon obtained by carbonizing peanut shells at 1100 °C[70,121]. The HRTEM micrograph reveals an assembly of curved lines, randomly intertwined together. These are frequently interpreted as curved edges of randomly oriented, but stacked graphene layers.[122–126] Accordingly, in many studies the interlayer spacing between the graphene layers is derived from the distance between these curved lines, which represents the edges of the graphene layers. However, a rough mental exercise illustrates nicely that this information may be misleading. Let us consider a graphene layer of about 100 hexagonal honeycomb rings, for which the carbon-carbon bond is 0.142 nm. Consequently, the area of one hexagonal ring is about 0.05 $nm^2$ and the area of the whole layer is approximately 5 $nm^2$. With respect to the given scale, the

HRTEM micrograph shown in **Figure 2-4a** should provide a clear evidence for the presence of such layer beneath the observed curved lines – but it does not. As a matter of fact, it has been reported that the graphene-like structure is the least thermodynamically stable phase until arrangements of about 6,000 carbon atoms[127], which directly translates in approximatively 1,000 hexagonal rings with an overall area of 50 $nm^2$. Consequently, the curved lines observed cannot be assigned to the edges of randomly oriented graphene layers, but instead reveal the surface of (highly defective) graphene-like layers, as already stated more than three decades ago[128]. This is further highlighted by lower resolution TEM micrographs, as displayed in **Figure 2-4b** and **2-4c**, for which the presence of sufficiently large layers is very evident. In addition, **Figure 2-4c**, shows that these layers are partially overlapping and may be curved. However, no perpendicularly oriented layers are observed – even on this larger scale.

We may thus conclude that these layers are highly defective and disordered structures, as earlier proposed by Marsh and colleagues[128]. Such a highly defective structure is illustrated in **Figure 2-4d** (inspired by Shinn.[129]). The model suggests that the curved lines observed in HRTEM micrographs are chains of cyclic carbons rather than the edges of graphene layers.

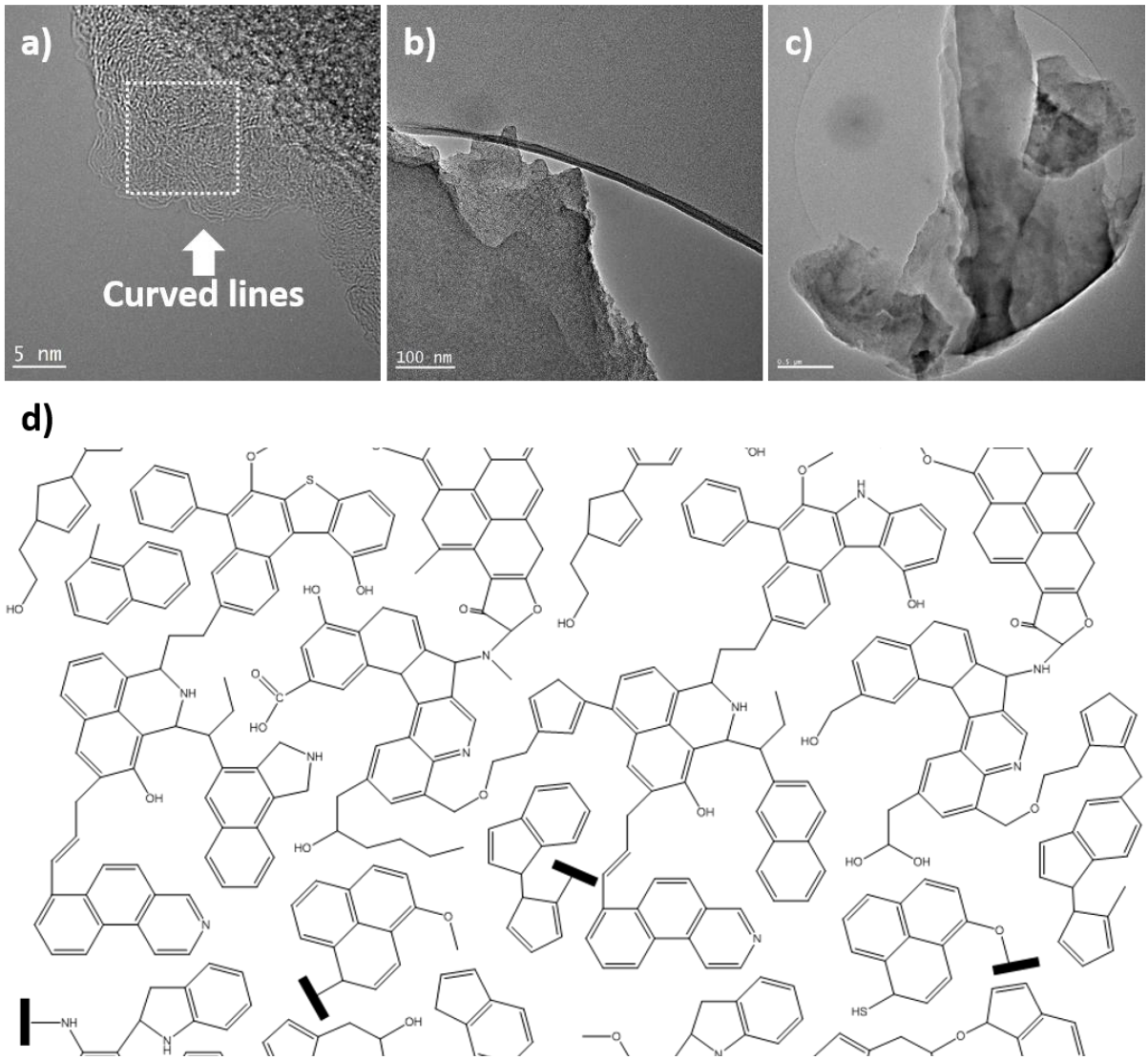


**Figure 2-4.** (a) HRTEM micrograph of a peanut-derived hard carbon, highlighting the "curved lines", frequently referred to as the edges of perpendicularly oriented graphene layers. (b) and (c) TEM micrographs of the same sample at lower magnifications. (d) Schematic illustration of a highly defective 2D graphene-like layer in hard carbons. Idea and illustration is strongly based on and derived from Shinn.[129] Adapted and reproduced from [129] with permission of Copyright © 1984 Butterworth & Co. (Publishers) Ltd.

### *2.2.3. X-ray diffraction related measurement*

X-ray diffraction (XRD) is the technique of choice to study the structure of crystalline materials. The X-rays focused on the materials are scattered by the atomic lattice. Positive and negative interferences lead to a pattern of diffraction, which can be used as a projection of the reciprocal space in the plane or axis of the detector, with peaks corresponding to crystalline periodicity according to Bragg's law [130,131]. Semi crystalline as well as amorphous materials can be studied by XRD, giving information at local scale, although the amount of accessible information decreases analogously to crystallinity. This technique allows to easily differentiate the various types of $sp^2$ and $sp^3$ carbons, such as diamond, graphite, hard carbon, soft carbon or graphene. It also enables researchers to study the graphitizability, i.e., the ability of turbostratic carbon materials to evolve toward a graphite structure at high temperature[77]. As mentioned earlier, this is fundamental piece of information as it is the property that separates soft carbons from hard carbons.

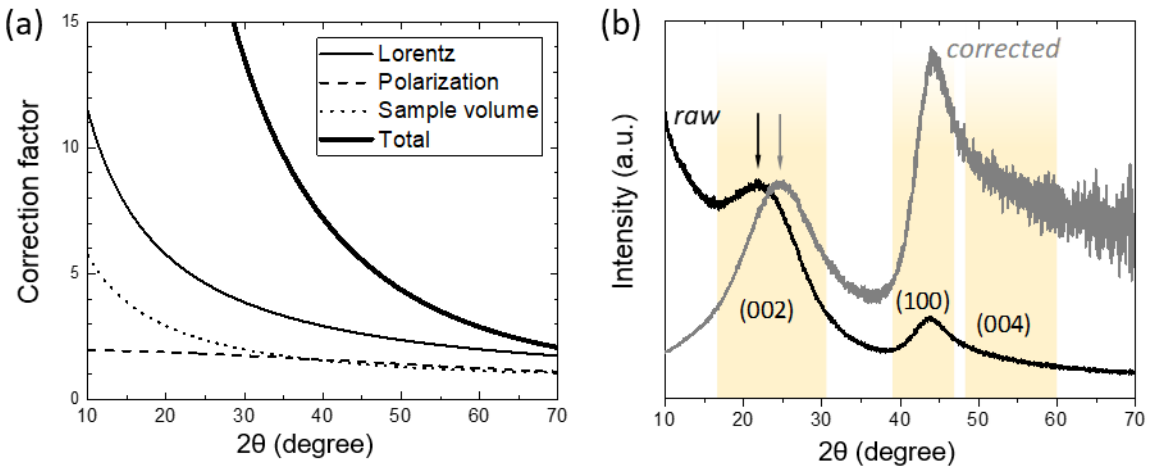


**Figure 2-5.** a) Angular-dependent factors influencing the intensity in a typical powder X-ray diffraction experiment. b) Typical powder X-ray diffraction pattern of a hard carbon, with (grey) and without (black) correction by the factors presented in (a). The arrows indicate the apparent (002) peak position.

The local structure of hard carbon can be described as highly turbostratic and disordered 2H graphite[75,132]. As a consequence, the typical XRD pattern of hard carbon (see, e.g., **Figure 2-5b**) presents broad features referring only to the (00l) and (hk0) reflections due to the loss of layer-to-layer crystalline coherency[132,133]. Moreover, a raising background is typically present at low angle owing to the presence of a large amount of fine structure microporosity, which overlays the main interlayer's reflection (002) [75]. The traditional geometry used for lab-scale XRD diffraction induces an angular dependency of the detected intensity as the product of three factors: the Lorentz factor, related to the solid angle of detection, the illuminated sample volume which varies with the source-sample angle, and the polarization factor (see **Figure. 2-5a**) [134]. For highly crystalline materials these factors affect the relative reflections intensity and are usually taken into account in the refinement methods based on the Rietveld theory. In the case of poorly crystalline materials, such as hard carbon, these factors may additionally distort the peak's profiles and induce a shifting of the apparent peaks' center positions. The shift is more pronounced when the reflections are broad and observed at low angle. This can be clearly seen in **Figure-5b**, in which the uncorrected (002) reflection position is observed at 22.3º, corresponding to an apparent interlayer distance *d*002 of 4.0 A. After correction, however, the reflection is observed at 24.8º, corresponding to an interlayer distance of 3.6 A.

Since carbon is a light element, carbon based materials tend to be relatively transparent to X-rays. In the case of hard carbon, due to the very large width of its diffraction features, XRD measurement are also very sensitive to the background, as an angle dependent background can change the apparent shape of the diffraction features, including their apparent positions. Most of the plastic materials, such as

poly(methyl methacrylate), Kapton, Mylar, etc., currently used by XRD sample holders manufacturers present a broad diffraction peak at low angle overlapping the (002) reflection of hard carbons. The choice of the sample holder is thus of primary importance. A deep sample holder may avoid background contribution, but will induce an extra broadening of the diffraction features due to the deep penetration depth of the XRD in carbons. A shallow sample holder avoids the latter issue, but it requires to be made of a material that generates zero background, such as single crystal silicon. Compared to crystalline materials, the characterization of hard carbon by powder X-ray diffraction (PXRD) is thus more critically dependent on the choice of the sample holder and the proper application of the relevant angular dependent intensity corrections in relation with the chosen instrument geometry.

#### *2.2.3.1. Pair Distribution Function (PDF) analysis of PXRD data*

The analysis of PXRD patterns from hard carbon is usually only qualitative due to the absence of adapted refinement programs for such highly disordered and locally anisotropic structures. An alternative method consist in the reverse Fourier transformation of diffracted data in order to extract the PDF, which consists in the radial distribution function of the structure in the real space in terms of radial density. This requires high-quality data, recorded over a broad angular range and corrected for any background, parasitic signal or angle dependent intensity factors. It allows for instance to verify assumptions on the structural model, the origin of low crystallinity (strains, disorder, defects, crystallite size, etc.) or the range of the crystalline order, being a powerful analysis method for low-crystallinity materials. One of the earliest examples of such analysis are found in Rosalind Franklin's work from 1950 on non-

graphitic carbon material[75]. More recently, the use of PDF analysis of PXRD data allowed reaching important advances in the description of the structure and microstructure of hard carbon as well as its mechanism of sodium uptake [86,95,135].

#### 2.2.3.2. Small-angle X-ray scattering *(SAXS)*

The raising background typically observed at low angle in the XRD patterns of hard carbon ( seen e.g. in inset of **Figure 2-6b**) was soon demonstrated to be due to fine structure microporosity [75], which is a typical feature of hard carbons closely related to their inability to graphitize [69,77,113,136] as well as of their larger specific capacity compared to other $sp^2$ carbons [62,137]. In order to properly study the low angle scattering, the range needs to be extended toward low angles, which requires a specifically designed geometry. For this purpose, as presented in **Figure 2-6a,** the SAXS technique uses transmission geometry, collimated incident beam path, a 2D detector centered in the incident beam axis, and a beam stop avoiding the direct beam to saturate the detector. Evacuated beam path down to at least secondary vacuum is also of prime importance in order to avoid background and intensity loss from the scattering and absorption by the air. The typical SAXS pattern obtained for hard carbon after integration of the 2D detector image is represented in **Figure 2-6b** as a function of the scattering vector ($Q = 4\pi \sin(\theta) / \lambda$), together with a schematic representation of the microstructure of a hard carbon at various scales. The smaller the Q values, the larger the size of the features (pores, particles) that scatter X-ray intensity. As can be seen in **Figure 2-6b**, at lowest Q values the intensity drops as $Q^{-4}$, which is typical behavior for sharp interfaces of large objects [138,139]. In the case of hard carbon this can be ascribed to the macroscopic surface area of the particles (in

brown in the schematics of **Figure 2-6b**) [91,140,141].[ At intermediate Q values (1-10 $nm^{-1}$) the intensity evolution shows a plateau followed by a kink, which is typical of the presence of micropores (in blue in the schematics of **Figure 2-6b**)[91,114,140,142]. Finally, at large Q values the first diffraction peaks ((002), (100) and (004)) can be observed, which are related to the carbon structure at molecular scale.

SAXS is a powerful complementary analysis to gas adsorption techniques as it allows the detection of the total porosity, i.e., the surface (open) porosity as well as the bulk (closed) porosity[69,91,143]. A well performing hard carbon is required to exhibit a low external surface area to minimize the first cycle irreversible charge loss related to the SEI formation, and a high concentration of internal (closed) microporosity to maximize the specific charge storage[69]. Gas adsorption only probes the open surface porosity, thus not being sensitive to the internal, closed porosity. The earlier models for the microstructure of hard carbon were established by R. Franklin in early 50's based on the combination of PXRD and SAXS [75,77]. Later on, the group of J. Dahn intensively used SAXS for the study of hard carbons for application in LIBs and SIBs[62,137,140,144,145], as well as S. Komaba in their seminal paper of 2011 [146]. Since then, several publications focusing on the study of hard carbon for SIBs include SAXS analysis[91,147–149], although only a few present quantitative analyses of the amount of porosity[91]. This requires an intensity-calibrated instrument, which is rarely the case for lab-scale instruments.

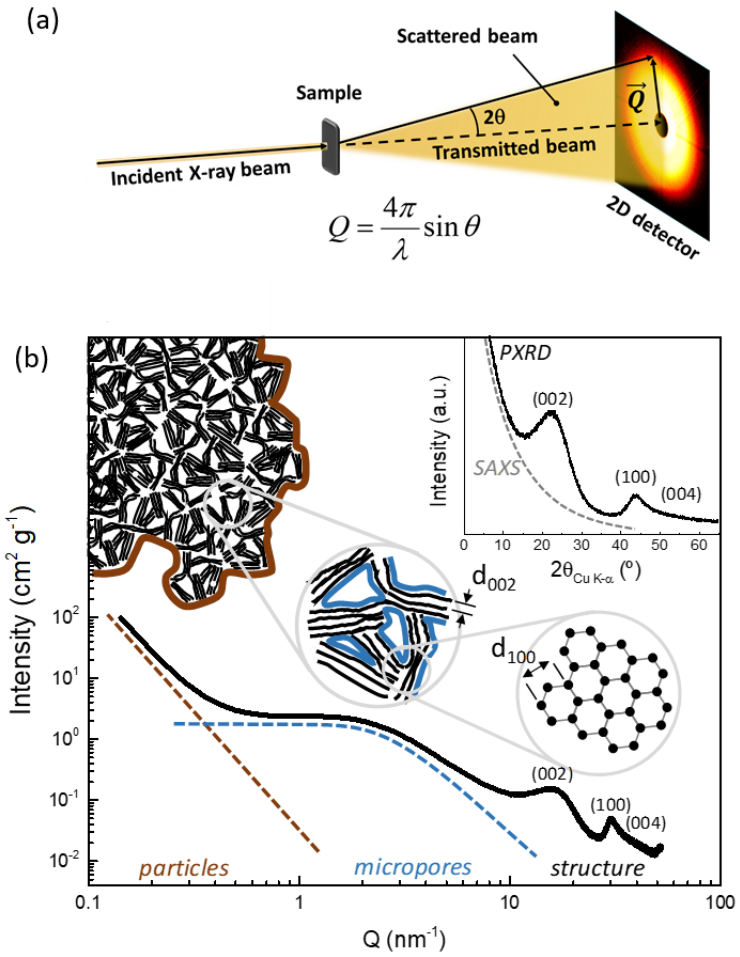


**Figure 2-6.** (a) Typical transmission geometry used for SAXS experiments. (b) Main panel: Full range plot of scattering pattern from SAXS to PXRD, represented as absolute intensity versus scattering vector Q in log-log scale; the schemes represent the structure and microstructure at various scales, from macroscopic surface area (left), to micropores (center) to atomic structure (right). Inset: Typical PXRD pattern of hard carbon, with main reflections indexed according to the 2H graphite structure; the grey discontinuous line indicates the SAXS background signal.

### *2.2.4. Ex-situ, in-situ and operando XRD and SAXS:*

Intercalation of alkali metals typically induces structural changes in the host electrode material, which generate a signature in their XRD patterns, thus making XRD a fundamental tool to study the storage mechanism [150]. Such measurements can be

performed with (ex-situ) or without (in-situ) extracting the material from the cell after electrochemical reaction. The measurements can also be performed in operando conditions, i.e., while the electrochemical reaction is occurring. Many examples can be found of such studies on cathodes and anodes of LIBs and SIBs, including graphite and soft carbon anodes [62,150,151]. In the case of hard carbon, however, the width of the diffraction peaks, the weakness of the intensity and the poor intensity/background ratio make such measurements very intricate [83,152]. A few reports can be found with operando measurement of XRD in hard carbon, see e.g. [62,83,92], with Stevens and Dahn reporting a significant change of intensity suggesting sodium intercalation. However, no changes of the peaks positions have been found by these authors, possibly due to the width of the peaks and the poor signal over noise ratio induced by the diffusion diffraction pattern of hard carbon. Ex-situ measurements, which do not present restriction on the acquisition time, have allowed a clearer observation of actual changes in the (002) reflection position[71,135,146] although the strong background signal due to the sample holder (typically Kapton film or tape to avoid contact with the air) and the other electrode components (binder, metal foil) could hardly be avoided.

The use of in-situ SAXS is far from common, probably due to the scarcity of lab-scale SAXS instruments. A notable in-situ SAXS experiment is that of Stevens and Dahn reported in 2000[62,137], reporting operando SAXS in sugar-derived hard carbon using a standard PXRD configured in transmission mode. They observed a clear change in the intensity of the SAXS signal, which led them to propose the historical model of sodium insertion into the micropores as origin of the low-voltage plateau typically observed in galvanostatic cycling measurements of hard carbon electrodes.

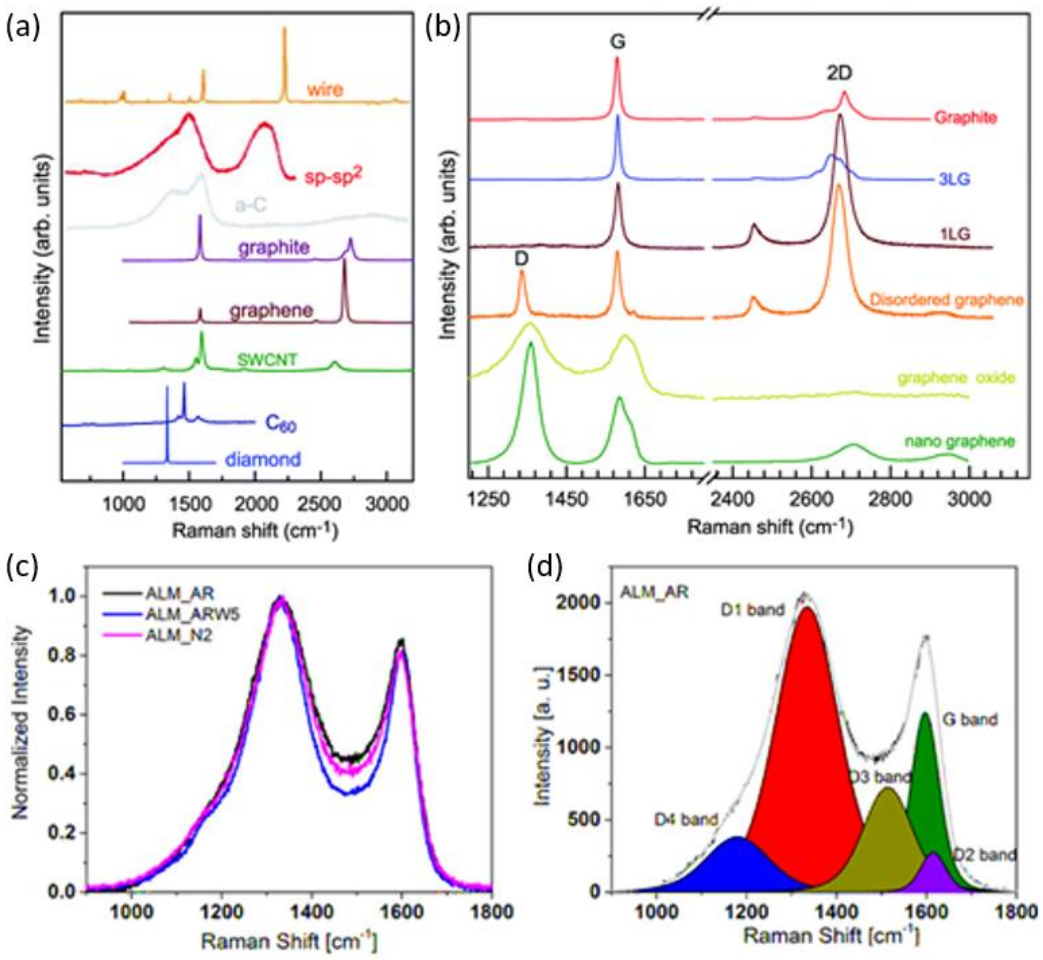


**Figure 2-7.** (a) Typical Raman spectra of carbon based materials and nanostructures, (b) Raman spectra of graphene-based materials. [153] (c) Raman spectra of lignin-based carbonaceous materials and (d) proposed spectra deconvolution. [154]. References [153,154] are licensed under a Creative Commons Attribution-Non Commercial 3.0 Unported Licence.

### *2.2.5. Raman Spectroscopy*

Over the years, Raman spectroscopy has become a key technique for the characterization of various carbon allotropes and disordered structures (see **Figure. 2-7 (a, b)**) [155–157]. Raman is a non-destructive technique and, due to the sensitivity to

the local changes in the carbon structure and the high resolution, is a powerful tool for the investigation of the ordering of the carbon-based electrode materials as well as the understanding of the structural changes occurring on carbon electrodes employed in rechargeable batteries [66,69].

The large variety of carbon structures and the derived different physical properties is directly related to the ratio of $sp^3$ and $sp^2$ bonds. Among the $sp^2$-bonded carbons, several materials with various degrees of graphitic ordering can be obtained going from microcrystalline graphite to glassy carbon. The Raman spectra reported in most of the studies of carbon based materials are dominated by $sp^2$ contributes [156,157]. Indeed, the commonly used excitation in Raman spectroscopy is visible light (633 nm or 514 nm), which always resonates with the π states. As a consequence, even for amorphous carbon structures dominated by $sp^3$ contributes, the visible Raman spectra are due to $sp^2$ vibrations. The cross section for the amorphous $sp^3$ C-C vibrations is negligible for visible excitation, thus its Raman signature can only be seen using UV excitation[156,157].

For this reason, amorphous and nanocrystalline carbons, even the ones containing small domains of graphitic ordering, present Raman spectra mainly dominated by two features, i.e., the G and the D band. The G band is related to the bond stretching of all pairs of $sp^2$ atoms in both rings and chains while the D band is related to the breathing modes of $sp^2$ atoms in ring.[158] The presence of the D band is often assigned to structural edges defects, indeed highly-oriented pyrolytic graphite (HOPG), which presents the highest degree of three-dimensional ordering, does not exhibit the D band. Accordingly, the intensity ratio between the G and the D band ($I_G/I_D$) is generally used to define the degree of defectiveness and disorder in the investigated carbons. In addition, the $I_G/I_D$ is also used to calculate the average lateral graphene domain size,

using an equation firstly proposed empirically by Knight and White [159] for a specific excitation of 514.5 nm and later generalized by Cançado[160] for any excitation laser energy in the visible range as follows:

$$L_a = 2.4 \cdot 10^{-10} \lambda_{nm}^4 \left(\frac{I_G}{I_D}\right)$$

It is worth mentioning, that other techniques are also employed to calculate the crystallite size, such as XRD and TEM. However, the values observed are slightly different. The values obtained by XRD by using the Scherrer equation, are generally smaller than those obtained by Raman and TEM, most likely due to the different physical basis of the three techniques.[161]

It is important to point out also that the $I_G/I_D$ ratio appears not the best parameter to evaluate the amorphous nature of the investigated carbons as it is not directly linked to the presence of $sp^3$ domain. However it can be indirectly related to the fraction of $sp^3$ sites as exhaustively described by Ferrari [157].

A proper deconvolution and fitting procedure of the Raman spectra may offer insights in the $sp^3$ content. For instance, the D and G bands can be generally deconvoluted in 5 components, namely G, D1, D2, D3 and D4[158,162] (see **Figure. 2-7(c, d)**). Interestingly, while the D1 and D2 bands are assigned to the vibration mode of microcrystalline graphite and disordered graphitic lattice respectively, the D3 and D4 band are attributed to the presence of amorphous carbon. Specifically, the D3 band is associated to the presence of large amounts of amorphous carbon [158] while the D4 band is related to C-H termination groups or, more in general, to adsorbed molecules or molecular fragments [163]. Recently, the deconvolution process and the calculation of the peak areas ratio was applied by Marino et al.[154] to lignin-derived hard carbon for application in SIBs (see **Figure. 2-7(c, d**)).

The second-order overtone and combinational Raman modes of graphitic-like structures are rarely reported and investigated in studies of hard carbons for application in SIBs are.[71,164] At about 2700 $cm^{-1}$, the G' band typically appears for graphite containing carbons. The G' band is the second order of the D band and thus also called 2D band.

Interestingly, the 2D band presents shape, splitting and position changing according to the number of graphene layers along the hexagonal axis representing an optimal parameter to be investigated for the study of short or medium range ordered stacking[156]. Additionally, Raman analysis can successfully elucidate the presence of curved and folded graphene respect to flat graphene layers. Reported studies shows that for scrolled graphene, the D band is enhances and the G band splits into three distinct peaks.[165].

In light of the large amount of information that Raman spectroscopy can give, it is without any doubt considered as an invaluable tool for the investigation of the structural properties of hard carbon materials for application in electrochemical fields. Ex-situ and in-situ Raman applied to SIBs may enable the elucidation of the sodium storage mechanism by highlighting the structural domains involved upon sodiation, specifically disclosing the role of graphitic-like and amorphous carbon domains.

### 2.3. Sustainability

In line with the SIB philosophy, the sustainability of the employed materials represents a key parameter for the successful implementation of the developed materials in commercially viable SIB prototypes [166]. Indeed, the use of biomass waste as hard carbon precursors could efficiently increase the sustainability of the final system. **Figure 2-8a** reveals that processing biomass (organic) waste offers reduced

environmental impact than other precursors, e.g., petroleum coke[167]. Meanwhile, around 730 Tg of biomass is burned in a typical year with about 250 Tg contributed by crop residues burned in the open fields [168,169]. This results in the generation of $CO_2$ and other local pollutants, which are responsible for the high concentration of smog in many developing countries[170]. As a consequence, biomass waste is not only an ideal precursor for hard carbon in SIBs, but it may allow an active $CO_2$ removal from the atmosphere thus enabling a sustainable future[120,148,171–180]. Considering the large abundance, low cost, high carbon content, easy collectability and poor usability in conventional biomass recycling technologies[181–185], lignocellulosic materials are the best candidate as hard carbon precursors. Furthermore it has been reported that lignocellulose-derived hard carbon exhibit improved electrochemical performance when compared to other types of biomass waste[70,91,154,186,187]. Lignocellulose is the main component of plant cell walls[188] (**Figure. 2-8 (c)**), which is the most abundant bio-material. Besides the materials' sustainability study, further works on the energy consumption of the bio-derived hard carbon pyrolysis process have been reported. Barelli and co-workers addressed the energy sustainability of pectin-free apple pomace-derived hard carbon materials used as SIB anodes [120,189]. In their study, the components of the pyrogas was reported (see **Figure. 2-8 (d)**) and a pyrolysis efficiency of 79.5% was calculated according to the simulated equation for energy balance. A recent study of the impact of acid activation of hard carbons on sodium storage performance reported that applying long-time phosphoric acid treatment could clearly improve the sodium-storage behaviour at low potentials. The combination between long-time (2 weeks) acid treatment of lignocellulosic hard carbon precursors (peanut shells) and relatively low carbonization temperature (1000 °C) could lead to a hard carbon with improved rate capability as anode for SIBs[121]. Sustainability studies

around hard carbons are increasing, however, more comprehensive studies should be done on many interdisciplinary aspects of hard carbon materials production and cost analysis

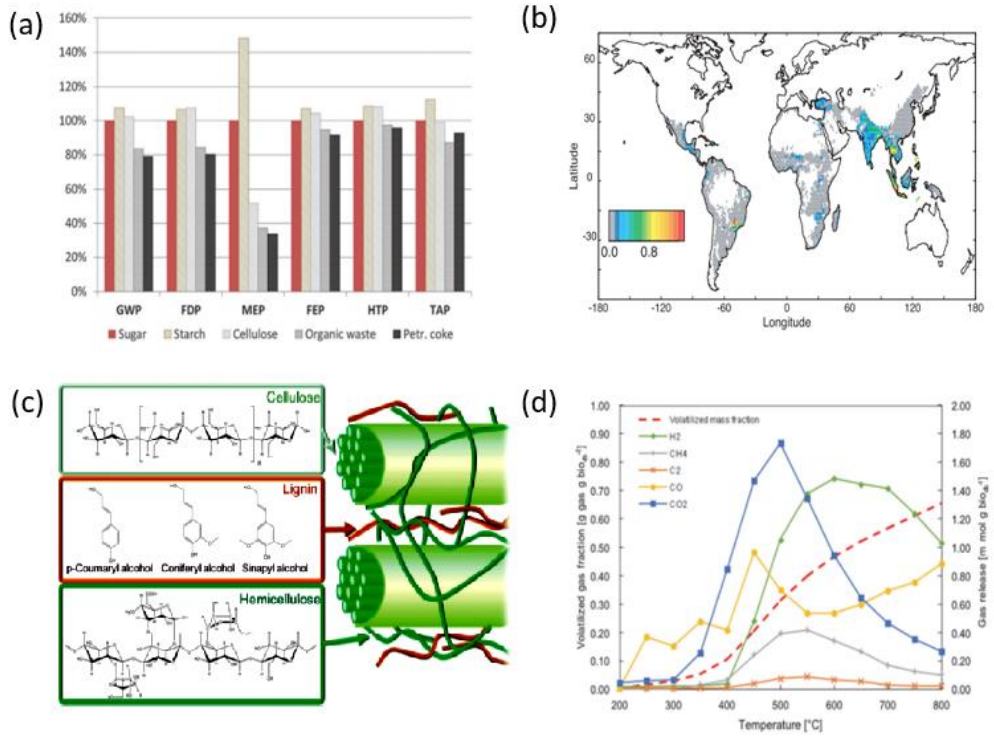


**Figure 2-8.** (a) Influence of the hard carbon precursor on the total environmental impacts associated with SIB production. GWP = global warming potential, FDP = fossil depletion potential, MEP = marine eutrophication potential, FEP = freshwater eutrophication potential, HTP = human toxicity potential, TAP = terrestrial acidification potential [167]. Reproduced from [167] licensed under a Creative Commons Attribution-Non Commercial 3.0 Unported Licence. (b) Burning agricultural residue in the fields in the developing world distributed on a grid of 1° latitude by 1° longitude with units Tg dry matter.[169] Reproduced with permission from Copyright © 2003 John Wiley and Sons. (c) Structure of lignocellulosic biomass.[188] Reproduced with permission of Copyright © 2012 The Royal Society of Chemistry. (d) Pyrogas components release as a function of process temperature: temperature-dependent volume flowrates of main gas components and gas release cumulate curve, pectin-free apple pomace as

hard carbon precursor.[189] Reproduced with permission of Copyright © 2018 The Royal Society of Chemistry.

### 2.4. Electrochemistry of hard carbons in SIBs: mechanism and challenges

Several promising hard carbon materials have been proposed for application as anode for SIBs. Despite new material development represents a crucial research field in search of improved rechargeable batteries, it is worth mentioning that the fundamental understanding of the sodium storage mechanisms in the host structure represents the most important task for a rational development of high performance anode materials [71,83,86,92,94,103,135,190–195]. An in depth understanding of the sodium uptake upon cycling will enable the achievement of invaluable knowledge for the definition of the key properties characterizing advances electrode materials. Indeed, the uncertainties related to the detailed processes occurring in the hard carbon structures upon cycling so far hindered an efficient improvement of the materials' electrochemical performance, additionally aggravated by the wide variety of factors influencing the electrochemical behavior, including the role of different precursors and temperature treatment [77,84,92]. Several mechanism have been proposed over the years. **Figure 2-9** reports some of the schematic models proposed so far toward the understanding of the sodium ions interaction with hard carbon upon cycling.

Early works on the mechanism reported by Stevens and Dahn stated that both sodium and lithium exhibit a similar storage mechanism in hard carbon, mainly consisting of two steps. The first one related to intercalation of ions into graphitic regions at higher potential, resulting in a sloping potential curve, and he second one involving nanoplating in micropores formed by the graphitic domains, resulting in a voltage plateau at low potentials[56,58,62,137].

This mechanism was explained taking into account R. Franklin's structural model [77], and was actually aimed to explain sodium migration into carbon electrodes in the aluminum production, with a side focus on assisting research on lithium-storage mechanisms[58]. During the same period, also other lithium-storage mechanisms[114,196–199] were proposed, however, the "house of cards" model appeared to be able to correlate both the Li and Na storage mechanism, thus, current reports mainly refer back to the "house of cards" model.

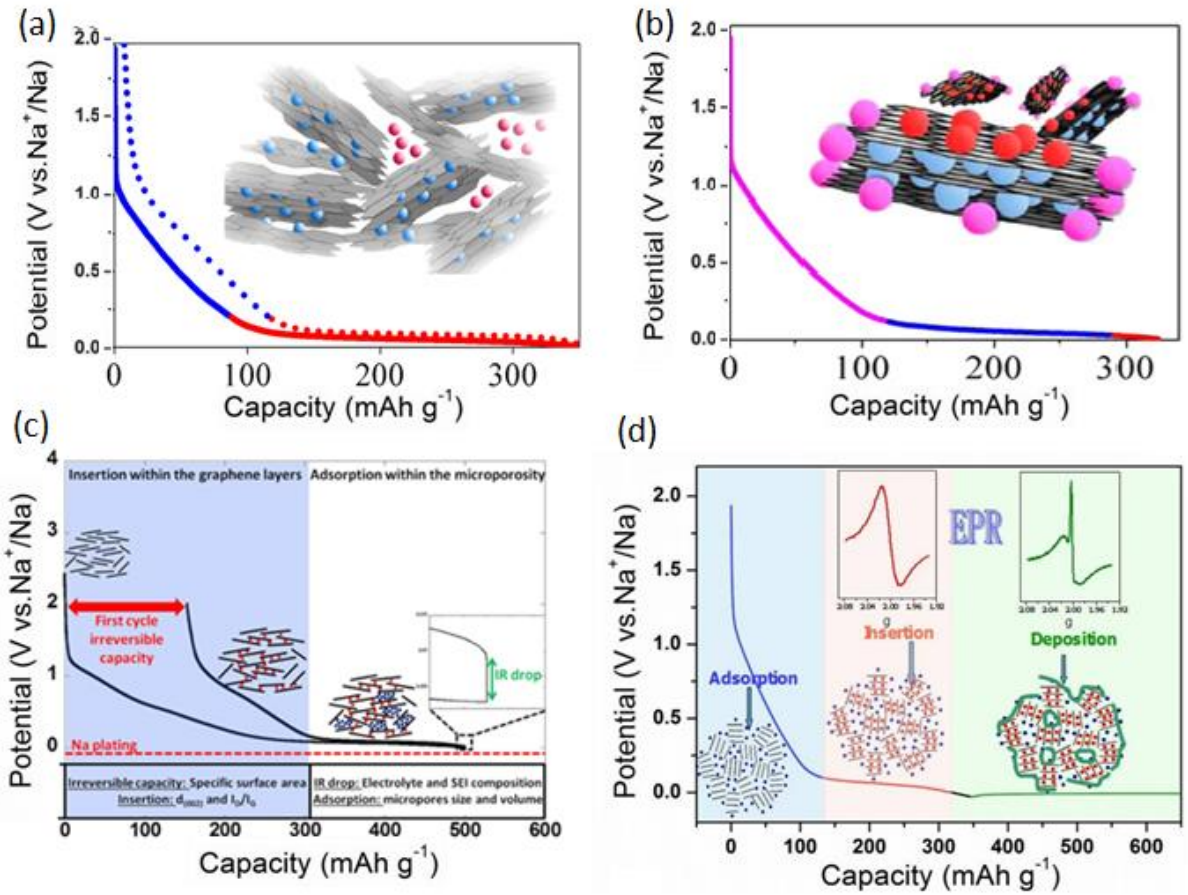


**Figure 2-9.** Representative model proposed so far for the sodium storage mechanism in hard carbon. (a) Visual representation of the "house of card" model. The two distinct phases are reported in blue and red: i.e. intercalation inside turbostratic nanodomains and pore filling.[135] Reproduced with permission of Copyright © 2015, American Chemical Society (b) Mechanistic model involving sodium ion storage at defect sites

in the sloping region, and intercalation between graphene sheets and minor phenomenon of Na-ion adsorption on pore surfaces in the low voltage region.[135] Reproduced with permission of Copyright © 2015, American Chemical Society. (c) Typical potential vs. capacity profile for hard carbon in sodium cells with associated parameters of interest such as irreversible capacity, IR drop, Na plating. The study proposes the well known insertion of sodium within the graphene layers followed by adsorption within the microsposity.[68] Distributed under e Creative Commons Attribution 4.0 License. (d). Schematic illustration of the Na-ion storage in hard carbon according to the "adsorption-intercalation" mechanism[200]. Reproduced with permission of Copyright © 2017 ECS-The Electrochemical Society.

Nowadays it is generally accepted that despite the similarities, the Li and Na chemistries may be very different, as already demonstrated with the case of graphite and silicon anodes, $Na_xCoO_2$ cathodes and the Na-$O_2$ batteries among others [14,25,47,201,202]. The Li storage mechanism in hard carbons cannot be directly transferred to Na based systems, however, the knowledge gained in the Li field is certainly helpful and gives some insights on the multiple processes which play a fundamental role also in the Na storage mechanism in hard carbons. Below we report a list of the main factors and processes which may occur upon sodiation:

- Na ions ad-/chemi-sorption at defects in the graphenic sheets.
- Influence and role of heteroatoms.
- Inter-lamellae Na-ion intercalation and the role of inter-layer *d*-spacing as well as the role of defects and heteroatoms in the graphenic sheets.
- Nanopore filling, i.e. plating and deposition of sodium (metal) on pore walls.
- Formation of sodium (metal) clusters at low potentials.

- Irreversible capacity and potential-curve hysteresis.

The understanding of these processes and the definition of the potential dependence upon cycling is crucial and will enable a clever and rational design of advanced and high performance next generation hard carbon anodes for SIBs.

It is known that the graphenic/fullerenic sheets in hard carbon include edges (mostly H-terminated) [78], functional groups [84], defects [95] and heteroatoms [84,86] in which Na ions are assumed to be reversibly ad-/chemisorbed, resulting in a sloping potential curve at potentials above 0.1 V vs. $Na/Na^+$ [86,92,103]. The sloping nature of the potential profile is explained considering a continuous/homogenous [92] process at sites with a wide energy distribution [92]. The heteroatoms act as electron donors toward the graphenic sheet [86], increasing the electron density at defect sites in the graphenic layer and thus creating favorable locations for Na bonding [86]. However, the role of ordered/stacked vs. disordered/free graphenic sheets for not-intercalated Na ions is still unclear and under discussion.

As already mentioned in the introduction section, graphite does not represent a feasible anode material in SIBs due to the energetically unfavorable formation of b-GIC, which is thought to be a consequence of the mater of chemical potential of Na intercalated carbon vs. that of plating but not only the mismatch between the Na ions size and the graphitic structure.[203] In hard carbons, the inter-layer (002) *d*-spacing is significantly increased, often around 360-400 pm, when compared to the one of graphite, i.e. 335 pm[92]. It is reported that an optimal interlayer distance for Na-ion storage lies within the 370–380 pm range [92], which would enable a facilitated access of Na ions to energetically stable sites near defects [204]. Defects and heteroatoms reduce the planarity of the graphenic layers and therefore in some regions may enhance the space for Na ions to migrate in between the layers. In addition, as

previously mentioned in presence of heteroatoms and defect sites the electron density is enhanced and therefore can promote the intercalation and hosting of Na ions [84,86]. The intercalation processes are observed as plateau-like regions in the voltage profile at potentials below 0.1 V vs. $Na/Na^+$ [86]. The nature of the plateau profile is associated to a two-phase reaction well matching with an intercalation process [92].

Another Na ions storage process observed in hard carbons is the pore filling. Qiu et al. reported that calculated formation energies indicate that ad-/chemisorption near defects would generally occur at first, followed by intercalation and finally pore filling[92]. However, the occurrence of pore filling remains unclear and the potential dependence on the phenomena is still under discussion. Similarly to pore-filling, the evolution of pseudo-/quasi-metallic clusters upon sodiation has been proposed and discussed. In detail, pooling of Na-clusters of 2-3 atoms and coherence lengths >10 Å have been reported to occur at low potentials after adsorbing of Na ions into surface pores, defects and between graphenic layers[95,103]. This would inevitable affect the interlayer arrangements and generate new regions available for Na insertion [95]. However, it is worth mentioning that other reports did not detect the presence of such features[92]. The latter reported results are a clear example on how challenging and still open for discussion is the understanding if the Na storage mechanism in hard carbons.

In addition, another fundamental question still to be answered is the temporal evolution of these processes. Are these phenomena to be seen as individual storage processes occurring in a consecutive order or they should be regarded as concurrent features?

In fact, the ad-/chemisorption at defect sites is in some cases described to occur simultaneously to intercalation into the graphenic sheets and in between stacked sheets[103]. Reported density functional theory (DFT) calculations have indicated that the sloping profile region could be explained by only considering intercalation

processes[95]. However, it is worth mentioning that intercalation is sometimes further defined as intercalation with adsorption at defect sites and regular intercalation, simply enabled by the increased *d*-spacing[86].

At last, the irreversible capacity observed during the initial cycle has been widely attributed to the large surface area of mesoporous hard carbon, however, recent studies on hard carbons with extremely low surface areas (<1 $m^2 g^{-1}$) lead to the assumption that the irreversibility is correlated with bulk rather than surface processes [71]. Moreover, the irreversibility was identified to be related with the decomposition of sodium carbonate formed by the reaction of Na and oxidized sites on/in hard carbon rather than the solid electrolyte interphase formation[103].

### 2.5. Aim and tasks of this thesis

Despite studied alongside with LIBs in the 80's, SIBs were sidelined due to the lower electrochemical performances. However, recently, concerns related to the supply of lithium as well as the transition metals commonly used in cathode materials for LIBs, have triggered the research and industrial community to focus their interest also in alternative chemistries to lithium. The uneven and limited distribution of the raw materials employed in the LIB technology is often used as the main reason for the renewed interest in the Na chemistry, however, it should be mentioned that several studies and future projection predict that a lithium shortage supply should not occur in the next 50 years, which would be even delayed when optimizing the recycling process of LIBs. On the other hand, one pressing concerns is certainly related to the high cost of extraction of lithium supplies and the increasingly high demand of lithium which brings uncertainties related to the inability to face the high demand with consequent fluctuation of the price and market related risks. The latter ones does not represent

unfavorable factors for the SIB technology, which is characterized by the use of earth abundant and cheap raw materials.

For these reasons, nowadays, SIBs are considered the next generation electrochemical energy storage system of choice. While from the sustainability and cost perspective SIBs are considered the most promising alternative to LIBs, further improvement and optimization in terms of electrochemical performance, mostly in terms of energy density, are needed. In this context, the development of high performance electrode materials is fundamental. At the anode side, hard carbon represents an excellent candidate. Several promising materials have been proposed with satisfactory results, however many issues still need to be addressed for the development of the next generation high performance SIBs.

The obtainment of advanced hard carbon anodes relies on a comprehensive understanding of the sodium storage mechanism as well as the function-structure correlation. In this thesis, systemic studies focusing on impact of different parameters on hard carbon structure and electrochemical performance of SIBs are reported. Impact of biomass precursors, closed pore and acid treatment of hard carbons are discussed in detail in Chapter 3, Chapter 4 and Chapter 5, respectively.

# 3. Impact of biomass waste based precursors on hard carbon anodes for SIBs

## 3.1. Introduction

Biomass appears to be a very appropriate source for hard carbon. A study[168] performed in 2003 revealed that around 730 Tg (1 Tg = $10^{12}$ g) biomass is burned in a typical year, with about 34% (i.e., ca. 250 Tg) contributed by crop residues burned in the fields. The open-air burning to dispose biowaste generates $CO^2$ and other local pollutants, e.g., soot, VOCs (volatile organic compounds) and sulphur dioxide, which are responsible for the heavy smog in some Asian and South American countries.[170] Consequently, recycle and reuse of waste biomass is becoming a consensus worldwide. Biofuels draw substantial attention in both academic and industrial circles.[205] However, the use of the cheapest and most abundant form of biomass, lignocellulose, is limited by the lack of low-cost processing technologies, which can efficiently convert lignocellulosic biomass into liquid fuels.[206] Thus, technical processes involving the large-scale application of lignocellulosic materials are highly desirable and urgently needed. Additionally, biomass waste can be considered a reliable large-scale carbon source because the intensive “industrialization’ of agriculture, due to the ever-increasing world population and improved living standards, leads to huge amounts of well-defined biomass and food wastes. [207]

Besides the low price and environmental friendliness, some biomass materials have specific microstructures, which can be retained after carbonization. According to literature, hard carbon materials derived from different biomasses deliver specific capacities ranging from 100 mAh $g^{-1}$ to 350 mAh $g^{-1}$ at low current densities.[71,208]

Compared with commercial precursors such as glucose, sucrose and polymers,[209] biomass-waste may represent an ideal carbon source. As a matter of fact, several biomass wastes have been investigated, such as banana peels,[71] pomelo peels,[176] rice husks,[210] ox horn[211] and peanut shell[173]. However, to the best of our knowledge, no studies have been performed to evaluate the impact of different biowaste on the structural properties and electrochemical behaviour of the derived hard carbons in order to establish a more rational material design.

Of course, biomass waste is not a pure chemical. It is, in fact, composed of several components, but it is frequently free of charge if not subsidized (disposing industrial bio-waste disposal carries, frequently, additional costs). Generally, the major component of plant-derived biomass is cellulose. Cellulose molecules align to form microfibrils, which themselves are aligned and bound into macrofibrils by a matrix of hemicellulose, pectin or lignin.[212] In consequence, cellulose based biomass, in a simplified manner, can be categorized into the three sub-classes belonging to pectin-, hemicellulose- and lignin-based materials. **Table 3-1** reports a summary of different carbon sources according to the above-mentioned classification.

Thus, a comparative study between hard carbons derived from waste materials belonging to the three different sub-classes, i.e., peanut shells (lignin-based), corncobs (hemicellulose-based) and apples (pectin-based). The impact of these carbon sources on the physical characteristics and the electrochemical performance of the derived hard carbon materials (namely P-HC (pectin-based), H-HC (hemicellulose-based) and L-HC (lignin-based)) is evaluated. It is shown that the carbon source strongly affects the structural characteristics and the electrochemical behavior of the hard carbons.

**Table 3-1.** Main binder component as well as amount of cellulose and main binder in the different dried carbon sources.

| Hard carbon | Carbon source | Main binder component | Content of main binder component / %[213–215] | Content of cellulose / % |
|---|---|---|---|---|
| P-HC | Apple waste | Pectin | 11.7 % | 43.6% |
| H-HC | Corncob | Hemicellulose | 35 % | 45 % |
| L-HC | Peanut shell | Lignin | 27-40 % | 34-45 % |

## 3.2. Experimental section

### *3.2.1 Synthesis of biowaste-derived hard carbon*

Peanut shells and corncobs were cut into pieces and dried at 80℃ for 72 hours. The resulting materials were manually ground into powders, then completely wetted with phosphoric acid (80 wt.%) and stored for 2 weeks under ambient atmosphere in a fume hood (for P-HC, apple biowastes were wet with phosphoric acid (80 wt.%) for 3 days[175]). Afterwards, deionized water was added and the suspension was filtered. Subsequently, the solid fraction was rinsed with deionized water until the pH was close to 7.0, then dried at 80℃ overnight, transferred into a quartz tube and annealed at 1100℃ under argon atmosphere for 1 hour (heating rate 1℃ $min^{-1}$) and furnace cooled.

### *3.2.2 Material characterization*

The structure and morphology of hard carbon materials were investigated by means of X-ray diffraction (XRD, Bruker D8 Advance diffractometer with CuK□□ radiation) and scanning electron microscopy (SEM, Zeiss Auriga®). The Brunauer-Emmett-Teller

(BET) surface area and pore width was determined by nitrogen adsorption measurements using an ASAP 2020 (Accelerated Surface Area and Porosimetry Analyzer, Micrometrics). CHN elemental analysis was performed with an Elementar vario MICRO cube. Raman measurements were performed with a confocal InVia Raman micro spectrometer with a 633 nm laser (Renishaw; each spectrum was taken as the average of three 10-second accumulations). The X-ray Photoelectron Spectroscopy (XPS) characterization was performed with a PHI 5800 MultiTechnique ESCA System, using monochromatized Al-K□ (1486.6 eV) radiation. The measurements were performed with a detection angle of 45°, using pass energies at the analyser of 187.85 and 29.35 eV for survey and detail spectra, respectively. All XP spectra were calibrated to the signal of amorphous carbon (hard carbon) at 284.8 eV and processed using CasaXPS software.

### *3.2.3. Electrode preparation and cell assembly*

Electrodes were prepared with a dry composition of 80 wt.% hard carbon, 10 wt.% conductive carbon (SuperC45®, Imerys) and 10 wt.% sodium carboxymethyl cellulose (CMC, WALOCEL®CRT 2000 PPA 12, Dow Wolff Cellulosics). CMC was first dissolved in deionized water to obtain a 5 wt.% solution. The conductive additive and hard carbon were added to the CMC solution and the resulting mixture was dispersed via ball milling for 2.5 h (70 min and 10 min rest; 1 repetition; speed main disk: 400 rpm; speed rotating planets: -800 rpm). The obtained slurry (solid content: 14.3 %; wet thickness of 150 µm) was casted with a doctor blade on a dendritic copper foil at room temperature. Afterwards the coated electrodes were dried at 80℃ for 10 minutes and then at room temperature overnight under ambient atmosphere. Disk electrodes (Ø = 12 mm) were punched and dried for 2 h at 20℃ and 10 h at 150 ℃ under vacuum in a

glass oven. The average active material mass loading of the electrodes was around 1.5 mg $cm^{-2}$.

### *3.2.4. Electrochemical characterization*

Three-electrode Swagelok® cells were assembled using the hard carbons as the working electrode (WE) and sodium metal (99.8%, Acros Organics) as the counter (CE) and reference (RE) electrodes. All potential values given in this manuscript refer to the $Na/Na^+$ quasi-reference electrode. Whatman® glass fiber GF/D disks were used as separator and soaked with 240 µL of electrolyte (1M $NaClO_4$ in EC: PC (1:1 wt.%)). Sodium perchlorate $NaClO_4$ (98% Sigma Aldrich) propylene carbonate (PC, Sigma Aldrich), and ethylene carbonate (EC, UBE) were used as received. Electrolyte preparation and cell assembly were carried out in a glove box (MBraun) with oxygen and water contents below 0.1 ppm.

Galvanostatic cycling tests, between 0.02 V and 2.0 V (vs $Na/Na^+$), were carried out with a battery tester (Maccor series 4000, U.S.A). The specific current of 200 mA $g^{-1}$ is defined as 1 C. Cyclic voltammetry was performed between 0.02 V-3.0 V (vs $Na/Na^+$) using a multi-channel potentiostat-galvanostat (VMP3, Biologic Science Instruments). All electrochemical tests were performed in climatic chambers at 20 ± 1°C.

## 3.3. Results and discussion

*3.3.1. Synthesis, structural and morphological characterization of biomass derived hard carbons.*

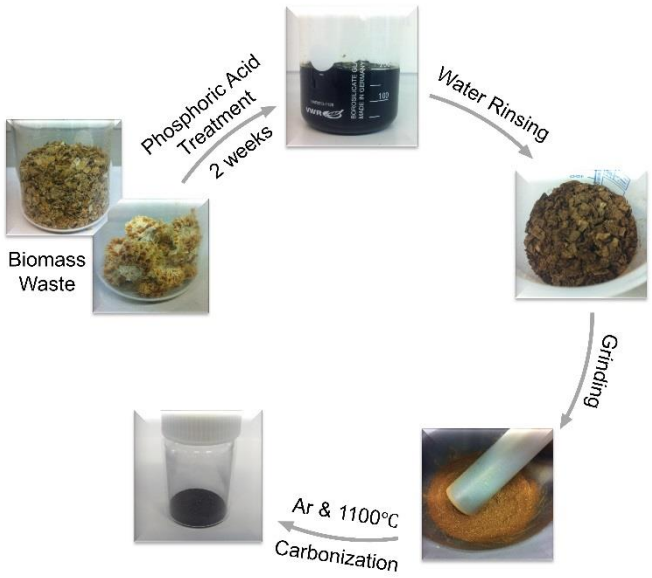


**Figure 3-1** : Synthesis scheme for the different biowaste-derived hard carbons.

The synthesis route of corncob and peanut shell biomass derived hard carbons is schematically reported in **Figure 3-1**, while that for waste apple has been reported previously.[175] It should be noted, however, that the synthesis of P-HC (from waste apples) involved the phosphoric acid treatment for only three days, since longer treatments resulted in very low yields (below ≤ 0.5% for two weeks treatment).

Phosphoric acid is used as activating agent, playing a key role in the process as described later.[176,216] It is observed that the suspensions containing apple biowaste and corncob turned black and jelly-like after one day, while the suspension of peanut shells remained transparent and liquid-like. This difference is explained considering that apples contain pectin, besides glucose and fructose, and corncob contains hemicellulose. Both these chemicals contain α-connected units (i.e., connecting oxygen in axial position), which are known to be prone to hydrolysis in aqueous

solutions.[217] Consequently, the treatment in concentrated phosphoric acid leads to the destruction of the polysaccharides and, hence, of the fibril structure of the biomass, which explains the formation of jelly-like suspensions. In contrast, lignin (peanut shells) is more stable against hydrolysis or protonation in acids. As a matter of fact, no black colloids are formed upon acid treatment of peanut shells, resulting in a large fraction of the compact fibril structure retained.[217] The water-rinsing step is performed to remove the black colloids and other water-soluble impurities. The subsequent thermal treatment leads to the carbonization of the acid treated biomass, involving the release of $H_2O$, $CO_2$ and other gaseous species. As a consequence, the carbonization step leads to different yields of 38.2%, 24.7% and 33.2%, respectively, for L-HC, H-HC and H-HC, reflecting the stability of the biomass in acid and its heteroatoms content. The yields have been calculated with respect to the dried acid treated and water rinsed biomass.

The structural properties of L-HC and H-HC have been investigated by XRD (**Figure 3-2 a** and **b**) and Raman spectroscopy (**Figure 3-2 c** and **d**) while the morphology has been investigated by SEM analysis (**Figure 3-2 e** and **f**).

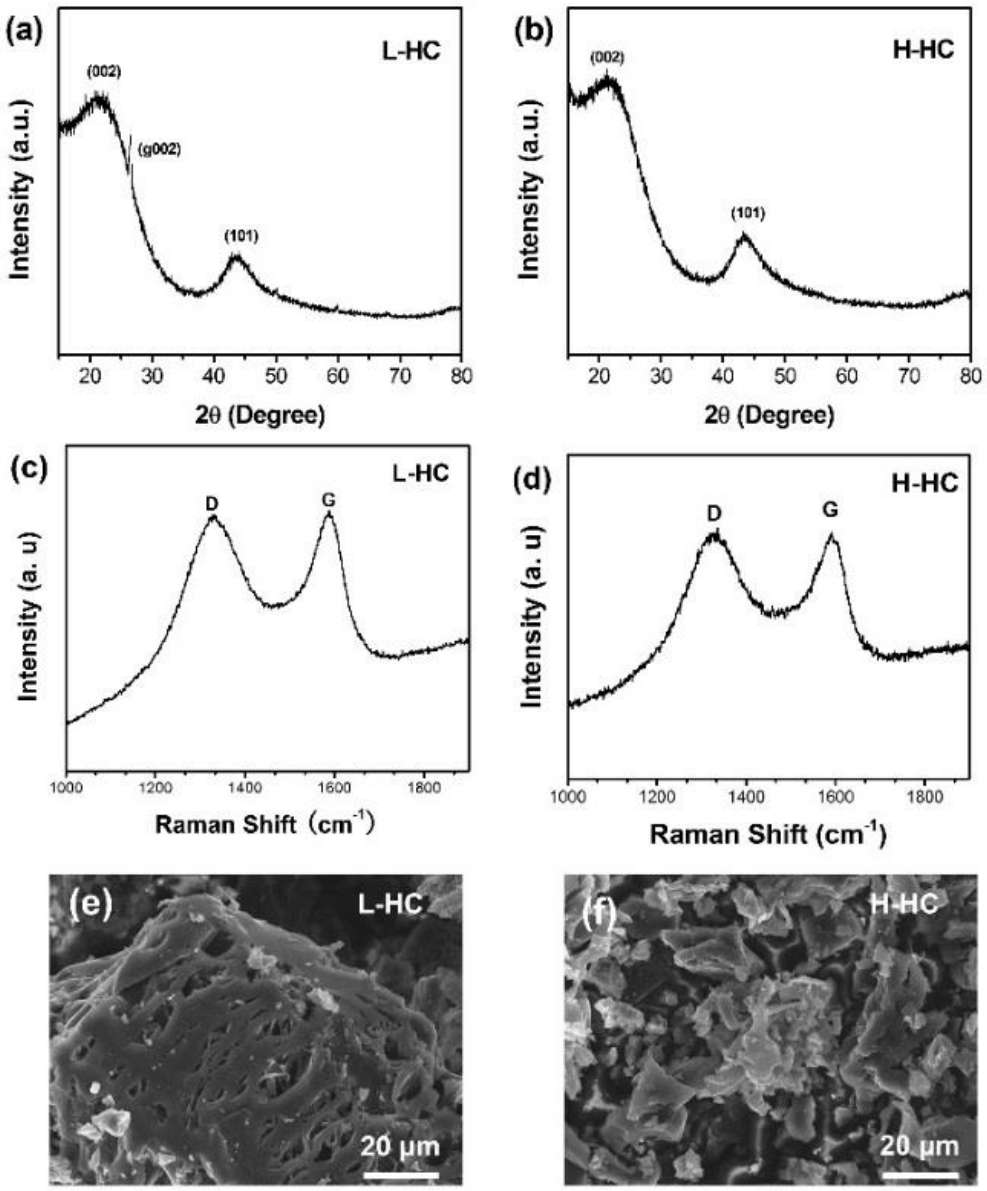


**Figure 3-2:** Structural and morphological characterization of L-HC and H-HC hard carbons. X-ray diffraction patterns (a and b), Raman spectra (c and d) and SEM images (e and f).

**Figures 3-2 a** and **b** show the characteristic (002) and (101) reflections of hard carbons, respectively, at 22° and 43° (2θ). The calculated average interlayer spacing ($d_{002}$) of L-HC and H-HC, obtained from the (002) reflection via the Bragg equation, is rather similar (about 0.408 nm and 0.406 nm, respectively). The additional reflection

at 26.5° (2θ) in the diffraction pattern of the L-HC material is attributed to the (002) reflection of graphitic carbon. Interestingly, this is not observed in H-HC. [78] This may be due to the higher acid stability of the lignin-based precursor, leading to the large extent of the macrofibrillar structure being retained. The presence of graphitic carbon might be beneficial for the electrochemical performance due to the enhanced electronic conductivity. The Raman spectra (**Figure 2 c** and **d**) of L-HC and H-HC exhibit a broad D-band (around 1340 $cm^{-1}$), ascribed to a defect-induced mode, and G-bands (around 1580 $cm^{-1}$), ascribed to the $E_{2g}$ graphitic mode. The intensity ratio of these bands ($R=I_D/I_G$) is commonly used as an index of the carbon materials disorder.[218] The intensity ratio of L-HC is 0.98, i.e., lower than that of H-HC (1.01), indicating a more ordered structure of the former material [219,220]. The SEM images reveal that L-HC (**Figure 2e**) still contains a fibril-like structure, while H-HC (**Figure 2f**) is composed of inhomogeneous particles.[175] Summarizing, the morphological and the structural results presented above confirm the highest stability of the lignin-based biomass against hydrolysis.

Characteristics of L-HC, H-HC and P-HC are summarized in **Table 3-2**. P-HC shows a lower calculated average interlayer spacing (about 0.385 nm) and higher structural disorder ($I_D/I_G$ = 1.26) than L-HC and H-HC. On the other hand, nitrogen adsorption/desorption measurements (BET) reveal the surface area of H-HC and P-HC to be rather similar and substantially higher than that of L-HC, reflecting the higher acid stability of lignin-based biomass. The comparison of the elemental composition of L-HC and H-HC proves higher nitrogen and carbon contents in the former material, but a higher residual content, typically considered as good indicator for the oxygen content, in H-HC. On the other hand, P-HC contains more hydrogen and carbon and

less residual elements than L-HC and H-HC. This can be explained by the shortest storage time in phosphoric acid (i.e., 3 days *vs* two weeks).

**Table 3-2.** Characteristics of L-HC, H-HC and P-HC.

| | L-HC | H-HC | P-HC |
|---|---|---|---|
| **Elemental Analysis C,H,N content / wt.%** | C: 89.57<br>H: 0.48<br>N: 1.24<br>Residual: 8.71 | C: 85.37<br>H: 0.53<br>N: 0.61<br>Residual: 13.49 | C: 94.50<br>H: 1.57<br>N: 0.53<br>Residual: 3.40 |
| **Raman Spectroscopy $R=I_D/I_G$** | 0.98 | 1.01 | 1.26 |
| **X-Ray Diffraction calculated average interlayer spacing $d_{002}$ / nm** | 0.408 | 0.406 | 0.385 |
| **BET Surface Area/ $m^2\ g^{-1}$** | 29.8 | 222.6 | 187.3 |

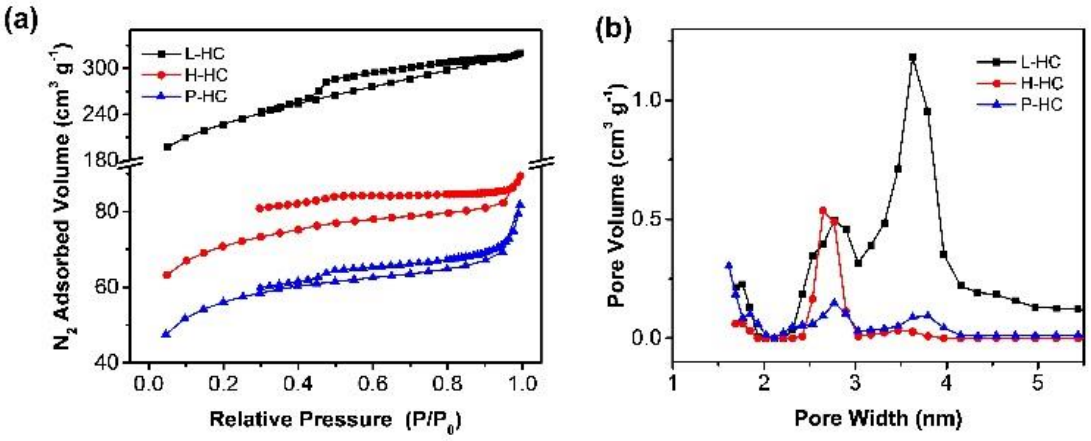


**Figure 3-3:** (a) Nitrogen adsorption–desorption isotherms and (b) DFT pore size distribution for L-HC, H-HC and P-HC.

The porosity of the as-prepared hard carbons was investigated via nitrogen adsorption-desorption measurements (**Figure 3-3a**). The DFT pore size distribution (**Figure 3-3b**) shows the existence of small mesopores with an average pore width of

about 2.7 nm in all hard carbons. However, the lowest fraction is observed for P-HC, while H-HC and L-HC show a similar pore volume. Interestingly, a significant fraction of slightly larger mesopores (3.7 nm) is observed for L-HC. Instead, P-HC and H-HC show, respectively, a low fraction and nearly no mesopores of this width. A recent work by Tarascon and coworkers[83] demonstrated the meso-porosity, rather than the micro-porosity, to be crucial for the reversible Na-ion storage in hard carbons along the plateau (0.02-0.1 V). Based on these finding a different electrochemical behavior can be anticipated for the different biowaste derived hard carbons.

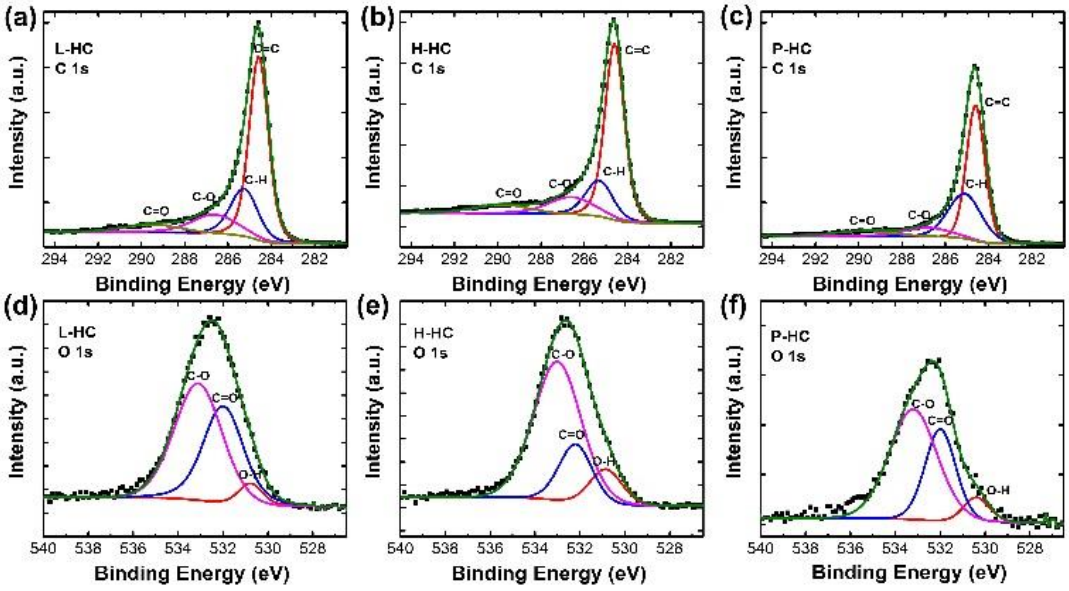


**Figure 3-4:** XP spectra of L-HC, H-HC and P-HC. (a – c) C 1s core level spectra; (d – f) O 1s core level spectra.

In order to further understand the impact of the various biomasses on the resulting hard carbon, XPS analysis of L-HC, H-HC and P-HC was performed in the carbon and oxygen regions (**Figure 3-4**).

**Figures 3-4 a-c** and **d-f** show the C 1s and O 1s core level spectra, respectively. In the C 1s region, four peaks are observed at binding energies of 284.6 eV, 285.1 eV,

286.5 eV and 290.0 eV, which are associated to C=C, C-H, C-O and C=O groups, respectively. In the O 1s region, three peaks are seen at binding energies of 530.8 eV, 532.3 eV and 533.2 eV respectively associated to O-H, C=O and C-O containing species.[221–223]

The percentage share of the various carbons is summarized in **Table 3-2**. However, it should be noted that the binding energy of the C-C ($sp^3$) bond falls in between that of C=C ($sp^2$) and that of C-H ($sp^3$), which makes the fitting of their C 1s core level spectra not possible. Thus, the quantitative determination of the C-C ($sp^3$) carbon species was not performed. Instead, their contribution was considered together with either C-H ($sp^3$) (C-H + C-C) or C=C ($sp^2$) (C=C + C-C) species (see **Table 3-2**).

In general, the XPS elemental analysis (**Table 3-2**) is in good accordance with the results obtained from CHN analysis. The slight differences can be attributed to the fact that XPS is limited to the surface region, while the elemental analysis probes the bulk composition. The difference in the amount of carbon detected employing the two techniques is negligible for L-HC and P-HC. However, for H-HC rather different values are obtained, in accordance with the higher amount of impurities, as indicated by the high residual content in CHN analysis, in this material. The lower nitrogen and higher residual contents found by CHN analysis can be explained via the higher content of adsorbed impurities[224] and is in good accordance with the higher surface area of H-HC compared to L-HC. The impurities, of course, affect the electrochemical properties like, e.g., the irreversible capacity, as it will be shown later on.

Consequently, L-HC and H-HC contain similar amounts of $sp^2$- and $sp^3$- hybridized carbons, but H-HC contains more impurities and P-HC more $sp^3$- hybridized carbons. These results are in good agreement with the data reported in **Table 3-3**. Summarizing, it can be stated that the nature of the biomass (and the main binder component therein)

has a strong impact on the composition and structural characteristics of the resulting hard carbons.

**Table 3-3.** Atomic percentage of carbon and oxygen as well as the relative amount (in percent) of C=C/C-C, C-H/C-C, C-O and C=O containing species as obtained from the XPS analysis of the C 1s and O 1s core level spectra.

| Spectra | | L-HC | H-HC | P-HC |
|---|---|---|---|---|
| C 1s | *Overall carbon content* | *88.7 at. %* | *89.2 at. %* | *93.6 at. %* |
| | *C=C + C-C* | *57.7 %* | *60.1 %* | *53.7* |
| | *C-H + C-C* | *21.4 %* | *17.0 %* | *32.0* |
| | *C-O* | *14.2 %* | *14.2 %* | *8.6* |
| | *C=O* | *6.7 %* | *8.3 %* | *5.8* |
| O 1s | *Overall oxygen content* | *10.6 at. %* | *10.3 at. %* | *6.1 at. %* |
| | *O-H* | *15.6 %* | *11.9 %* | *7.3 %* |
| | *O=C* | *39.9 %* | *19.4 %* | *32.3 %* |
| | *O-C* | *54.5 %* | *68.2 %* | *60.4 %* |
| N 1s | *Overall nitrogen content* | *0.7 at. %* | *0.5 at. %* | *0.3 at. %* |

*3.3.2 Electrochemical characterization of L-HC and H-HC*

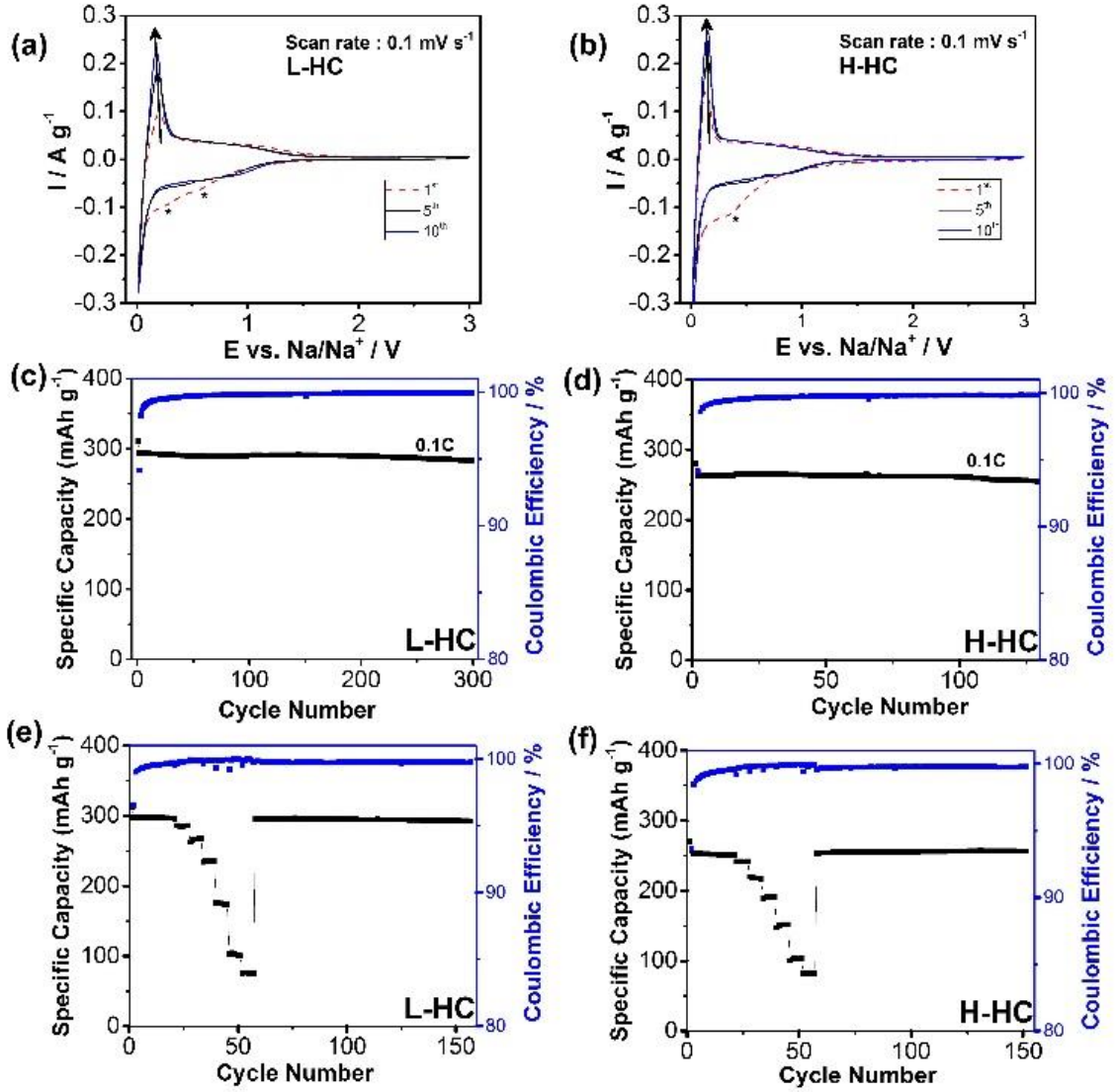


**Figure 3-5:** Electrochemical performance of L-HC and H-HC. (a, b) cyclic voltammograms (1st, 5th, 10th cycle) of L-HC and H-HC at a scan rate of 0.1 mV $s^{-1}$ in a potential range from 0.02 V to 3.0 V (vs $Na/Na^+$); (c, d) Galvanostatic long-term cycling at 0.1 C.

In order to understand the impact of composition and structural characteristics on the electrochemical performance, L-HC and H-HC were investigated via cyclic

voltammetry (CV) performed at a scan rate of 0.1 mV $s^{-1}$ within the 0.02-3.00 V (vs $Na/Na^{+}$) potential range (**Figures 3-5 a** and **b**).

Generically, i.e., after the 1st cycle, the peak couple below 0.3 V in the cathodic and anodic scans is attributed to the charge accumulation occurring in the pores, although, as mentioned in the Introduction, this interpretation of the voltammetric features is still debated.[177] The current observed between 0.2-1.5 V is associated to the storage of sodium at defect sites and between disordered graphene sheets.[62,83,135,225]

The cathodic scans of the first cyclic sweep reveal that almost no electrochemical reaction occurs from open circuit voltage (OCV) until 1.0 V. The current increase between 1.0 V and 0.1 V is associated to both the sodium storage mechanism and the SEI formation.[62,83,135,225] In contrast, the current peaks at 0.3 V and 0.6 V for L-HC and at 0.35 V for H-HC were not observed in the first cathodic scan of P-HC in our previous study.[175] They are probably related to the sodiation of impurities, which are present in L-HC and H-HC to a higher extent than in P-HC, as evidenced by elemental analysis. During the first anodic scan, a broad current peak is observed for both L-HC and H-HC between 0.02 V and 0.20 V, which increases upon consecutive sweeps, suggesting progressive structural changes of the hard carbon upon sodium uptake/release.[71]

In order to investigate the electrochemical behaviour of the developed materials, galvanostatic cycling tests were performed in sodium metal cells. **Figures 3-5** (**c** through **f**) report the electrochemical cycling performance of L-HC and H-HC. In the first cycle, a rather low current (0.02C) was used to activate (SEI formation) the electrodes. Panel c and d depict the electrochemical behaviour of L-HC and H-HC, respectively, upon long-term cycling at 0.1 C. During the 1$^{st}$ cycle, the coulombic efficiency for L-HC and H-HC is 68% and 57%, respectively, while the initial coulombic

efficiency for P-HC in our previous study was 61%.[175] The low first cycle efficiency is usually related to electrolyte decomposition, leading to SEI formation, and irreversible sodium uptake by heteroatoms, such as oxygen. The coulombic efficiency results are, overall, in good agreement with the differences in BET surface area and elemental composition of the hard carbon materials. Indeed, L-HC presents the highest 1$^{st}$ cycle coulombic efficiency and the lowest BET surface area. P-HC and H-HC have similar surface area, but H-HC contains more heteroatoms than P-HC, showing, in fact, the lowest 1$^{st}$ cycle coulombic efficiency. Nevertheless, both L-HC and H-HC show good coulombic efficiencies, up to 99%, already after 5 cycles. In terms of sodium storage performance (at 0.1C) a neat difference is observed between L-HC, which delivers a capacity of 298 mAh g$^{-1}$, and H-HC, exhibiting a capacity of only 257 mAh g$^{-1}$. Additionally, L-HC showed an excellent capacity retention (98%) after 300 cycles.

**Figures 3-5 e** and **f** compare the rate capability of L-HC and H-HC. L-HC delivers a capacity of around 299, 287, 266, 236, 175, 104, 77 mAh g$^{-1}$ and H-HC a capacity of 254, 242, 218.6, 191, 151, 103, 83 mAh g$^{-1}$, respectively, at 0.1 C, 0.2 C, 0.5 C, 1 C, 2 C, 5 C and 10 C. When the current rate is decreased back to 0.1 C, i.e., after the rate test, the specific capacity of L-HC and H-HC turned back to 297 mAh g$^{-1}$ and 254 mAh g$^{-1}$, respectively. The almost complete capacity retention demonstrates the good stability of the materials towards high rates. **Figure 3-6 a** and **b** shows selected potential profiles of L-HC and H-HC measured during the C-rate test at different current rates (from 0.1 C to 10 C). Considering the previous results reported for P-HC,[175] it is worth noting that all hard carbons deliver very similar capacities at high current rate such as 5 C and 10 C. Their potential profiles show that the plateau at about 0.1 V shifts below the lower cut-off potential at high currents, resulting in the slope region to contribute to the delivered capacity. [175]

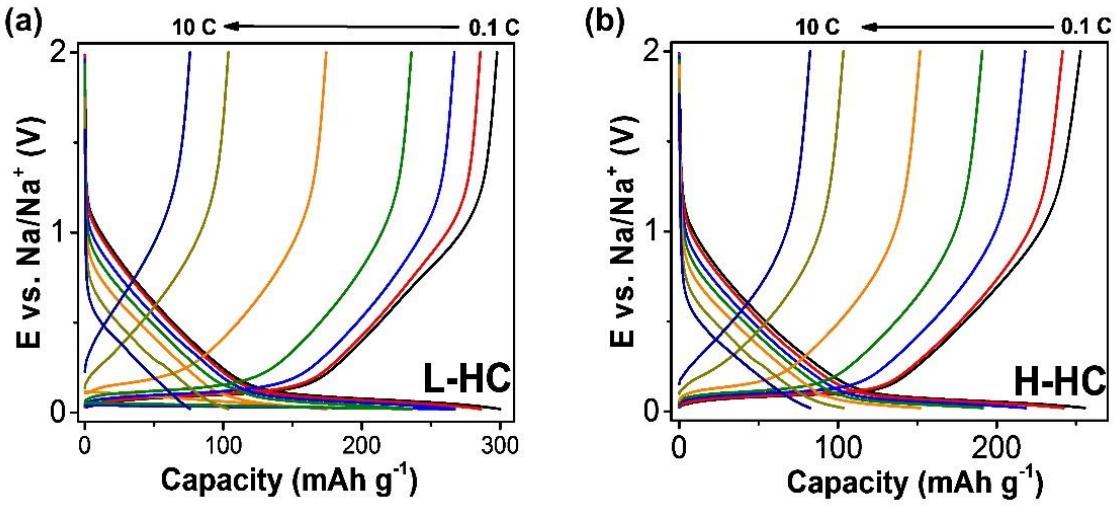


**Figure 3-6.** Selected potential profiles of L-HC (a) and H-HC (b) obtained during the C-rate test at different current rates (from 0.1 C to 10 C).

*3.3.3 Impact of biomass source on the electrochemical properties*

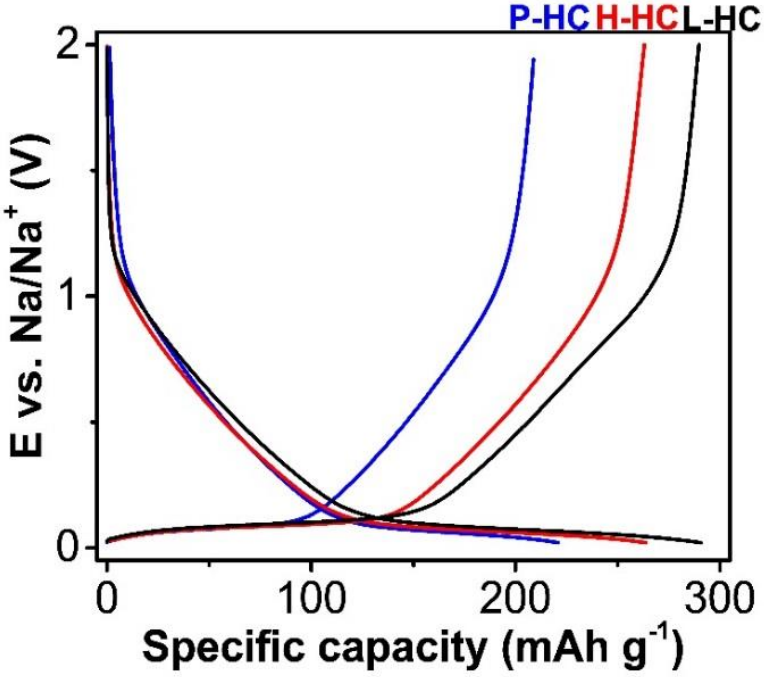


**Figure 3-7:** Comparison of the electrochemical performance of L-HC, H-HC and P-HC with charge/discharge profiles at 0.1 C in the 5$^{th}$ cycle.

To further link the electrochemical performance of the different hard carbons to their structural characteristics, the charge/discharge voltage profiles recorded in the 5$^{th}$ cycle of L-HC, H-HC, and P-HC are compared (**Figure 3-7**). All hard carbon electrodes show the typical sodium storage behavior with a sloping potential profile between 1.0-0.12 V and a subsequent plateau below 0.12 V. The sloped part of all hard carbons is practically overlapping, however, the low voltage plateau (i.e., below 0.12 V) of L-HC is more extended than that of H-HC and, especially, P-HC. The specific capacities between 1.0-0.12 V (slope) and 0.12-0.02 V (plateau) during the 5th discharge are shown in **Table 3-4**. The electrochemical behaviour of the different hard carbons can be understood comparing their capacities and connecting these with the measured structural properties. The slope region (1.0 V-0.12 V) is most frequently explained by the reaction of sodium with O and N heteroatoms as well as further sodium uptake via insertion into and adsorption on graphene-like sheets.[62,83] The capacity delivered/consumed within this voltage range (1.0-0.12 V) only slightly decreases upon going from L-HC to P-HC. L-HC shows the highest capacity in this voltage range, most likely because it has a higher interlayer spacing (XRD), a higher amount of O and N heteroatoms (CHN, XPS), and a better electronic conductivity, due to the presence of graphite (XRD), and finally a higher structural order (Raman $I_D/I_G$). H-HC shows a slightly lower capacity, which fits well to the slightly lower structural order (Raman) and the absence of graphitic carbon (see XRD), but similar average interlayer spacing and content of heteroatoms on the surface (XPS), and finally a higher content of impurities (high residual content in CHN). Finally, P-HC offers the lowest capacity due to the smallest average interlayer spacing (XRD), lowest content of heteroatoms

O and N (CHN, XPS), and, additionally, the most disordered structure (i.e., high amount of $sp^3$- hybridized carbon and no graphitic carbon Raman, XPS).

The plateau region (0.12 V- 0.02 V) is commonly explained by charge accumulation in the pores.[62,226] Recent work demonstrated that the extent of this region strongly depends on the hard carbon's mesoporosity. The formation of small mesopores significantly occurs at carbonization temperatures above 950°C.[227] Actually, the amount of mesopores goes along that of graphitic carbon upon increasing carbonization temperature. Note that at carbonization temperatures of 2800°C, mostly mesopores are present in hard carbons.[83] Thus, a higher content of graphitic carbon, i.e., $sp^2$- hybridized carbon, points to a higher amount of available mesopores and, hence, a larger extent of the low voltage plateau upon (de-)sodiation.[83] This is the case for L-HC, which, in fact, shows higher structural order (Raman), higher content of $sp^2$-hybridized carbon (XPS) and the presence of graphite (XRD). Indeed, nitrogen adsorption-desorption measurements revealed the highest intensity of small mesopores (i.e., those between 2.7 nm and 3.7 nm) in L-HC. H-HC has a similar structural order (amount of $sp^2$- hybridized carbon), but does not contain graphitic carbon, has a higher amount of impurities and a much lower fraction of small mesopores of 3.7 nm, all resulting in the lower capacity delivered/consumed by such a material in the low potential range. Finally, P-HC contains the largest amount of $sp^3$-hybridized carbon, shows the largest structural disorder and the lowest intensity of mesopores, which agrees well with the low capacity in this range.

Summarizing, these results show that a stable and reproducible electrochemical performance can be obtained for biowaste derived hard carbons. Moreover, our investigation strongly indicates that the mesoporosity of hard carbons determines the extent of the plateau below 0.12 V, whereas the sloping part (1.0-0.12 V) of the

potential profile mainly depends on the amount of heteroatoms and interlayer spacing. All those parameter depend on the composition and structure of the biomass source as shown via typical representatives of hemicellulose-, lignin- and pectin- rich biomass.

**Table 3-4.** Specific capacities consumed upon sodiation in the sloping region (1.0-0.12 V) and the plateau (0.12 V- 0.02 V) of L-HC, H-HC and P-HC.

| | Capacity (1.0V-0.12V) | Capacity (0.12V-0.02V) |
|---|---|---|
| L-HC | 131.79 mAh $g^{-1}$ | 158.81 mAh $g^{-1}$ |
| H-HC | 119.58 mAh $g^{-1}$ | 144.11 mAh $g^{-1}$ |
| P-HC | 111.76 mAh $g^{-1}$ | 108.24 mAh $g^{-1}$ |

### 3.4. Summary

Different waste biomasses, distinguished with respect to their main binder component, i.e., lignin, hemicellulose or pectin, have been investigated as precursor for the synthesis of hard carbons. In particular, peanut shells and corncobs, respectively containing lignin and hemicellulose, were successfully transformed into hard carbons. Their characteristics and electrochemical performance have been compared with those of apple (pectin) derived hard carbon.

The acid treatment has been identified as an important step in the synthesis, as the various binder components are differently sensitive towards hydrolysis, which strongly affects the characteristics of the derived hard carbons. The composition and structure of the various biomasses crucially influences the process yield, surface area, elemental composition (bulk and surface), structural disorder and impurity content of the resulting hard carbons.

In this work, the electrochemical behaviour of the various hard carbons, in terms of reversible and irreversible capacities, shape of the potential profile upon sodiation and desodiation, and cyclability, could be clearly linked to characteristic properties of the waste biomass precursors. Among the investigated materials, that derived from peanut shells, i.e., L-HC, shows the best specific capacity (298 mAh $g^{-1}$), highest capacity retention (98% after 300 cycles at low current rate (0.1 C)) and highest 1$^{st}$ cycle coulombic efficiency (68%) among all materials. The results reported herein demonstrate that biowaste not only represents an appealing renewable resource for carbonaceous materials, but may yield also high-performance anodes for sodium-ion batteries. In particular, the good electrochemical performance of hard carbons derived from peanut shells needs to be highlighted as lignocellulosic biomass waste cannot simply be used for the generation of bio fuel.

# 4. Impact of closed pores on hard carbon anodes for SIBs

## 4.1. Introduction

The use of waste as hard carbon precursor attracts wide attention. Various raw materials were investigated such as pomelo peels[176], corn cobs[228] and ox horns[211] for hard carbons. The use of industrial waste such as tires[90] has been reported but is still relatively unexplored although its use is certainly beneficial with respect to cost, availability (e.g. megaton-scale), quality (composition, homogeneity) and logistic efforts (collection, processing and transport). In our recent study we showed that the use of waste for the synthesis of hard carbons can decrease the environmental impacts that are associated with their production which finally results in more environmental-friendly batteries.[167] In another of our works we could show that waste-apple derived hard carbon, in fact, can be used as anode material in SIBs.[175] Furthermore, we recently determined the influence of the biomass waste composition, e.g. the content of pectin, lignin and hemicellulose, on the electrochemical performance and behavior of the corresponding hard carbons.[70]

Herein, we report the use of industrial biowaste, i.e. pectin-free apple pomace, as raw material for the synthesis of hard carbons with high electrochemical performance. The pectin-free apple pomace derived hard carbon (AP-HC) is thoroughly characterized and results are compared with our previous work on waste-apple derived hard carbon.

## 4.2. Experimental section

### *4.2.1. Synthesis of biowaste-derived hard carbon*

Apple pomace was transferred into a quartz tube and annealed at 1100℃ under argon atmosphere for 1 hour (heating rate 1℃ $min^{-1}$) and furnace cooled. The apple pomace derived hard carbon (AP-HC) was then manually ground and used without any further purification for the electrode preparation.

### *4.2.2. Material characterization*

The structure and morphology of hard carbon materials were investigated by means of X-ray diffraction (XRD, Bruker D8 Advance diffractometer with CuK□ radiation) and scanning electron microscopy (SEM, Zeiss Auriga®). $N_2$ absorption-desorption isotherms of samples were determined and analyzed by the Brunauer-Emmette-Teller (BET) method (Autosorb-iQ, Quantachrome). Raman measurements were performed with a confocal InVia Raman micro spectrometer with a 633 nm laser (Renishaw; each spectrum was taken as the average of three 10-second accumulations). The X-ray Photoelectron Spectroscopy (XPS) characterization was performed with a PHI 5800 MultiTechnique ESCA System, using monochromatized Al-K□ (1486.6 eV) radiation. The measurements were performed with a detection angle of 45°, using pass energies at the analyser of 187.85 and 29.35 eV for survey and detail spectra, respectively. All XP spectra were calibrated to the signal of amorphous carbon (hard carbon) at 284.8 eV and processed using CasaXPS software.

### *4.2.3. Electrode preparation and cell assembly*

Electrodes were prepared with a dry composition of 80 wt.% hard carbon, 10 wt.% conductive carbon (SuperC45®, Imerys) and 10 wt.% sodium carboxymethyl cellulose (CMC, WALOCEL®CRT 2000 PPA 12, Dow Wolff Cellulosics). CMC was first dissolved in deionized water to obtain a 5 wt.% solution. The conductive additive and hard carbon were added to the CMC solution and the resulting mixture was dispersed via ball milling for 2.5 h (70 min and 10 min rest; 1 repetition; speed main disk: 400 rpm; speed rotating planets: -800 rpm). The obtained slurry (solid content: 14.3 %; wet thickness of 150 µm) was casted with a doctor blade on a dendritic copper foil at room temperature. Afterwards the coated electrodes were dried at 80℃ for 10 minutes and then at room temperature overnight under ambient atmosphere. Disk electrodes (Ø = 12 mm) were punched and dried for 2 h at 20℃ and 10 h at 150 ℃ under vacuum in a glass oven. The average active material mass loading of the electrodes was around 1.5 mg $cm^{-2}$.

### *4.2.4. Electrochemical characterization*

Three-electrode Swagelok® cells were assembled using the hard carbons as the working electrode (WE) and sodium metal (99.8%, Acros Organics) as the counter (CE) and reference (RE) electrodes. All potential values given in this manuscript refer to the $Na/Na^+$ quasi-reference electrode. Whatman® glass fiber GF/D disks were used as separator and soaked with 240 µL of electrolyte (1M $NaClO_4$ in EC: PC (1:1 wt.%)). Sodium perchlorate $NaClO_4$ (98% Sigma Aldrich) propylene carbonate (PC, Sigma Aldrich), and ethylene carbonate (EC, UBE) were used as received. Electrolyte preparation and cell assembly were carried out in a glove box (MBraun) with oxygen and water contents below 0.1 ppm.

Galvanostatic cycling tests, between 0.02 V and 2.0 V (vs $Na/Na^+$), were carried out with a battery tester (Maccor series 4000, U.S.A). The specific current of 200 mA $g^{-1}$ is defined as 1 C. All electrochemical tests were performed in climatic chambers at 20 ± 1℃.

### 4.3. Results and discussion

The hard carbon was synthesized via a facile synthesis route that is schematically illustrated in **Figure 4-1a**. Compared to our previous works on waste apples[70,175], no phosphoric acid treatment of the industrial-waste was performed because during the pectin extraction process acid treatment has been applied.[229]

The morphology of AP-HC is shown in **Figure. 4-1b** and **c**. Interestingly, SEM reveals unique spherical bubble-like structures on the surface of the hard carbon particles. TEM measurement and EDX mapping are used to further understand the structure and component of this unique bubble-like morphology (**Figure. 4-1d** and **e**). The transmission picture reveals the bubble-like structure are empty inside and EDX mapping shows the surface is very homogenous. So far, similar structures have not been observed for other biomass derived hard carbons and also have not been observed in our previous study on waste–apple derived hard carbon. Consequently, this special structure should be related to the particular pectin-free composition of the biomass. A possible explanation is that the absence of pectin as cross-linking component facilitates the formation of a semifluid.[78] The decomposition of the biomass and resulting gas formation then leads to this particular surface morphology.

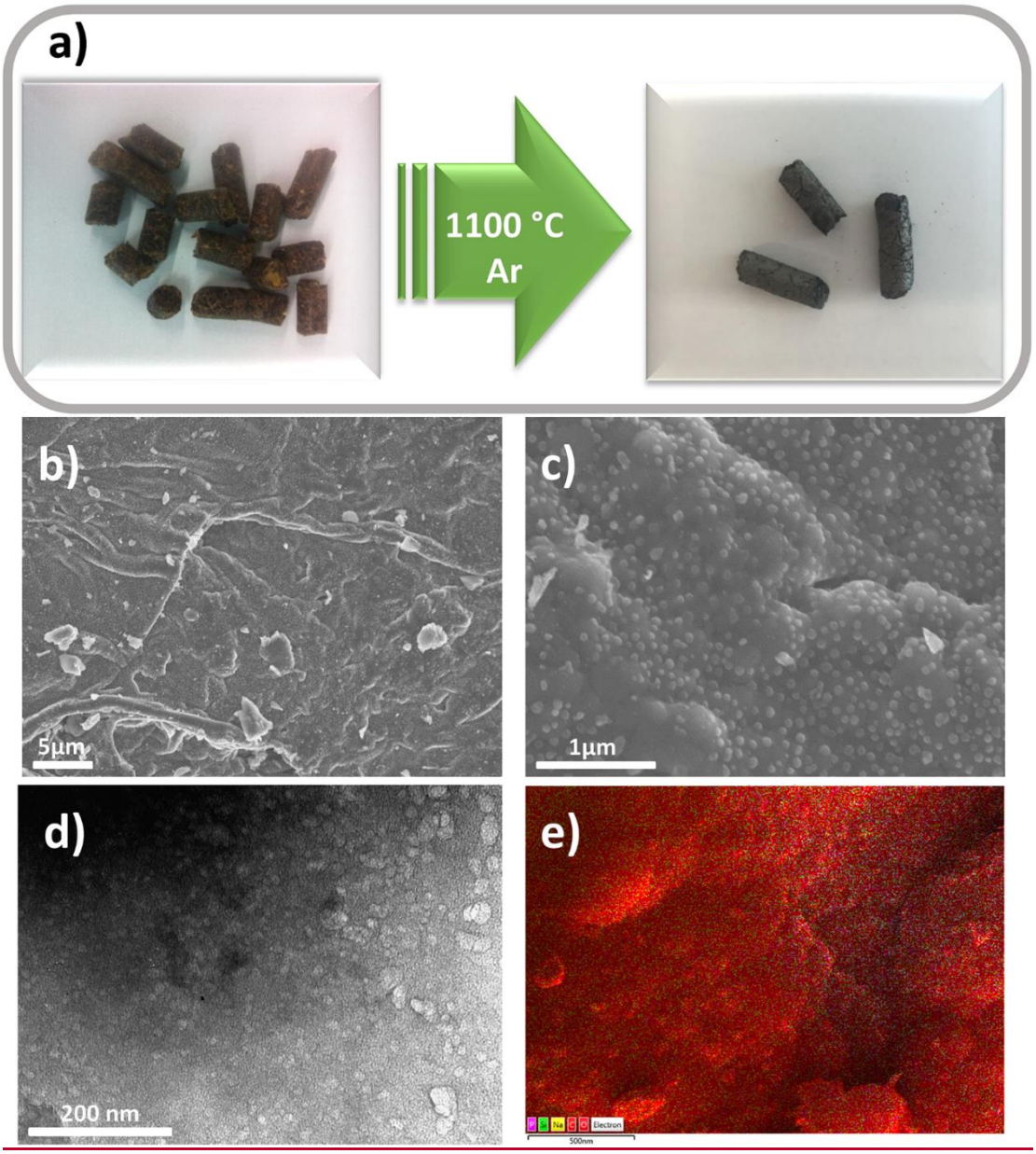


**Figure 4-1.** a) Schematic synthesis of pectin-free apple pomace derived hard carbon and images of educt and product. SEM morphology of AP-HC at a magnification of (b) 10kx and (c) 70kx. (d) TEM morphology of AP-HC and (e) EDX mapping of bubble-like surface.

The structural properties of AP-HC were characterized by Raman spectroscopy, X-ray diffraction (XRD), $N_2$-adsorption measurements and X-ray photoelectron spectroscopy (XPS). Results are displayed in **Figure 4-2**.

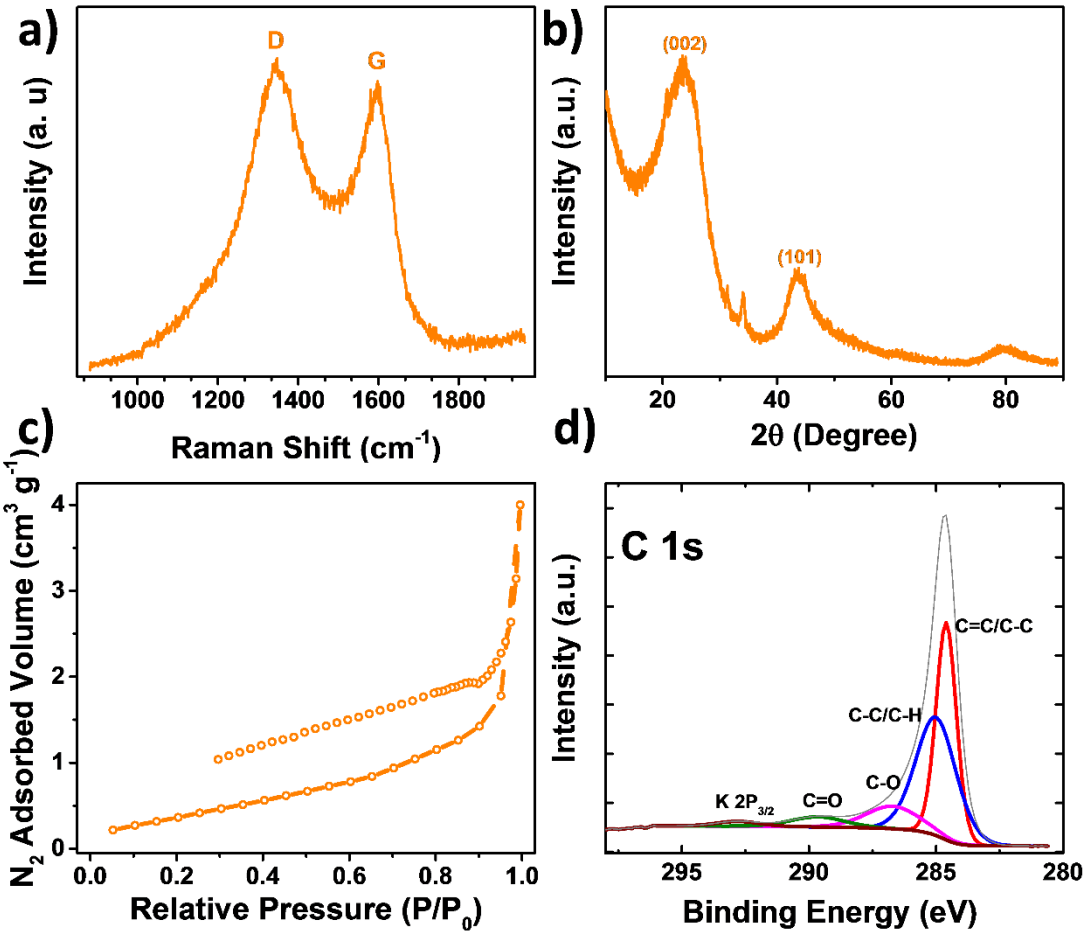


**Figure. 4-2.** (a) Raman spectrum; (b) X-ray diffraction pattern; (c) $N_2$ adsorption-desorption isotherm and (d) XP C1s core level spectra of AP-HC.

The structural properties of AP-HC are quite different from those of the apple waste derived hard carbon of our previous work in which the biomass contained pectin (A-HC)[175]. This observation is in accordance with the particular particle morphology observed via SEM in **Figure 4-1b** and **c**. The intensity ratio of the D and G bands ($I_D/I_G$ = 1.08), calculated average interlayer spacing ($d_{002}$ = 0.377 nm) and BET surface area

(1.54 $m^2 g^{-1}$) are decreased compared to A-HC material with $I_D/I_G$ = 1.26, $d_{002}$ = 0.385 nm and surface area of 187.3 $m^2 g^{-1}$.[70,175] Once more, the different structural properties can be explained with the very low content of pectin inside AP-HC. This facilitates the formation of a semifluid during carbonization which finally yields hard carbons with more graphitic character.[78] The reflections at about 31.4 °2θ and 34.1 °2θ in the XRD diffraction pattern of AP-HC (**Figure. 4-2b**) are originating from alkali impurities that have not been removed from the biomass.[230] The nitrogen adsorption desorption isotherm of AP-HC (**Figure. 4-2c**) can be classified as Type III, i.e. to a non-porous material.[231] The pore size distribution, indeed, confirms that AP-HC only contains few open pores. Considering the very low BET surface area and TEM images, results instead suggest that AP-HC contains substantial amount of closed pores. Additional pycnometry measurements and calculations were performed to determine the volume ratio of closed and open pores according to a published patent (detailed calculation in the end of the chapter).[120] The calculated volume ratio of closed and open pore for AP-HC is 22.8 % and 0.7 %, respectively, which once more confirms the substantial presence of closed pores. The XP C 1s core level spectra in Fig. 2d can be fitted with five peaks at binding energies of 286.6 eV, 285.1 eV, 286.7 eV, 290.5 eV and 293.5 eV, which are associated to C=C/C-C, C-C/C-H, C-O, C=O and K $2p_{3/2}$, respectively. Compared with A-HC,[70] AP-HC contains about 8% less C=C/C-C (45.4% *vs.* 53.7%) and 6% more C-C/C-H (38.3% *vs.* 32.0%) on the surface. The $I_D/I_G$ ratio of AP-HC is lower than that of A-HC, which shows that AP-HC contains more $sp^2$-carbon. The presence of the K $2p_{3/2}$ peak in XPS is in accordance with the additional reflection in XRD and once more suggests the presence of alkali impurities.

The electrochemical performance of AP-HC is shown in **Figure. 4-3**.

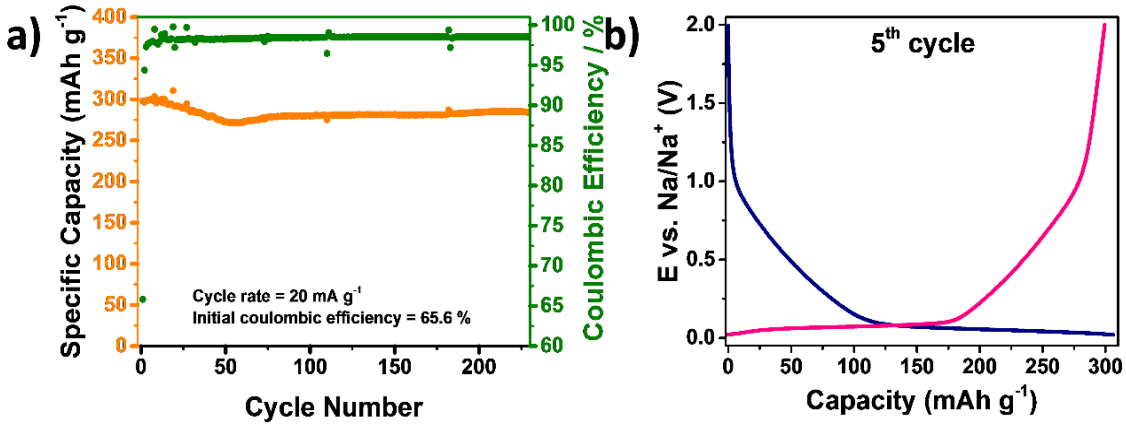


**Figure. 4-3.** Electrochemical performance of AP-HC. a) Long-term cycling performance at 0.1C and b) potential profile of the 5$^{th}$ cycle.

**Figure. 4-3a** shows that AP-HC delivers a good overall performance during the galvanostatic long-term cycling at 0.1C. In detail, AP-HC still delivers a specific capacity of 285 mAh g$^{-1}$ after 230 cycles, which corresponds to a capacity retention of 96% (*vs.* 2$^{nd}$ cycle). Interestingly, the capacity is also about 50 mAh g$^{-1}$ higher than that delivered by A-HC.[70,175]

AP-HC also shows a bit higher initial coulombic efficiency (65.6%) than A-HC (61.2%). However, the irreversible capacity is still too high considering the rather low BET surface area and open porosity. This may indicate that the irreversible capacity is mostly related to processes occurring in the bulk of the material rather than at the surface, indicating that closed pores and impurities have a strong impact.

AP-HC potential profile upon sodiation (**Figure. 4-3b**) is the one typical for hard carbons, exhibiting a slope between 2.00 V - 0.12 V (110 mAh g$^{-1}$) and a plateau between 0.12 V - 0.02 V (175 mAh g$^{-1}$). Interestingly, AP-HC delivers very similar capacities within the slope-like region but a much larger capacity within the plateau as

compared to A-HC (111 mAh $g^{-1}$, 108 mAh $g^{-1}$, respectively).[70] The similar extent of the sloping potential profile suggests that the particular surface morphology and lower BET surface area of AP-HC do not strongly affect the Na storage between 2.00 V - 0.12 V. Instead, the amount and nature of hetero atoms might play a more important role.

However, the different electrochemical behaviour at low potentials can provide some insights in the sodium storage mechanism in hard carbons, which is still controversially discussed.[62,83,86,92] The sodium storage along the plateau is commonly explained with charge accumulation in the hard carbon's porosity. AP-HC interestingly delivers much more capacity along the plateau than A-HC although it contains very little open porosity that is measurable by $N_2$ adsorption measurements. This indicates that open porosity does not play a major role for the sodium storage in this region. Instead, the amount of closed pores and their characteristics (inner surface, shape, and size) as well as the average interlayer spacing appear to have stronger impact. In any case, the Na- storage mechanism deserves to be investigated in greater detail in a future work.

### 4.4. Summary

Summarizing, we have synthesized a hard carbon from industrial waste, i.e. pectin-free apple pomace, via a very facile carbonization method. The hard carbon delivers a very competitive electrochemical performance with respect to the state-of-the-art despite being synthesized from very cheap and abundant waste.[117] Most importantly, the hard carbon exhibits a unique morphology and very interesting structural

properties, resulting in high sodium storage capacity and good retention upon cycling. Finally, the investigations enlightened the role of surface area and porosity on the sodium storage mechanism.

### 4.5. Calculation of closed and open pore ratio

**Equation 1** and **2** were used to calculate the ratio of closed and open pore, respectively.

$$R_{CP}(\%)=(1/d_{He}-1/2.26\ g/cm^3)/(V_{OP}+1/d_{He})\times 100 \quad (1);$$

$$R_{OP}(\%)=V_{OP}/(V_{OP}+1/d_{He})\times 100 \quad (2);$$

where $d_{He}$ is the bulk density measured via pycnometry with He, $V_{OP}$ is the open pore volume obtained from $N_2$ absorption-desorption measurements.

For AP-HC, $d_{He}$ is 1.740 g/cm$^3$, and $V_{OP}$ is 0.0040 cm$^3$/g. Accordingly, $R_{CP}$ is **22.8%** and $R_{OP}$ is **0.7%**.

# 5. Impact of acid treatment on hard carbons for SIBs

## 5.1 Introduction

Efficient electrochemical energy storage systems, such as rechargeable batteries and supercapacitors, are among the most compelling targets for a sustainable energy future.[232–234] Carbonaceous materials are considered appealing electrode candidates for alkali metal-ion batteries such as lithium-ion batteries (LIBs)[235], sodium-ion batteries (SIBs)[67] and potassium-ion batteries (KIBs)[236], and super capacitors[237]. A great deal of studies focus on designing carbon materials for these energy storage systems. Among them, particular interest is dedicated to carbon materials derived from bio-waste because of their sustainability.[238] In fact, about 40 million tonnes of unusable lignocellulosic biomass is produced every year, however, most of this material is thrown away,[239,240] or evern worse, burn in open air leading to air pollution and global warming[169]. Thus, the conversion of lignocellulosic biomass into valuable products is an important challenge towards a sustainable future.[183,239] Hence, approaches to increase the use of lignocellulosic biomass are highly desirable and urgently needed.[183,241] Considering its relatively high carbon content compared to other bio-waste materials, lignocellulosic biomass is an ideal precursor for the production of high added value carbon materials,[182,242] in alternative to biofuels, polymers and fine chemicals.

Most of the biomass-derived carbons are assemblies of highly defective graphene layers, which can be generally classified as non-graphitable activated carbons, or hard carbons in the battery field.[77,78] Several studies reported the implementation of

biomass-derived carbons in supercapacitors[243,244] and batteries[69,72,245,246], however, the establishment of a low-cost and sustainable synthesis method is still needed, especially for lignocellulosic biomass-derived carbons, but only a few studies are available.

Among the alkali-metal ion batteries, SIBs can employ only hard carbons as anode material. Indeed, although SIBs have the same working principle of LIBs[14,25], the full capacity of graphite cannot be achieved in SIBs because $Na^+$ ions do not intercalate into its structure except when co-intercalation of solvent molecules occurs as, for example, using glyme-based electrolytes[47,247]. However, in line with the low-cost and sustainability issues,[227,248] biomass-derived hard carbons play a key role in the development of SIBs.[10,69] As a result, several biomass derived materials have been reported as SIB anodes[71,175,211,228], among which, lignocellulosic precursors have drawn more and more attention[173,186,249–251]. Nonetheless, current studies on hard carbon anodes mainly focus on morphology control[252], heteroatom-doping[86,253] and annealing temperature regulation[83]. However, few studies focused on the chemical activation process although it may be a crucial step for hard carbon formation,[254] also impacting its electrochemical performance in SIBs.

Our recent studies revealed that using bio-wasted hard carbon for SIBs can efficiently decrease the environmental impact,[167,189] while exhibiting promising electrochemical performance[70,120]. It has been reported recently that the poor rate capability, which is considered as one of the main drawbacks in the implementation of hard carbon as anodes in SIBs,[255] may be improved by using ether-based electrolyte[256], introducing an artificial SEI[257] or doping foreign-heteroatoms into hard carbon materials[123,126]. However, up to date, a cost-effective and sustainable method to improve the hard carbon properties is still required. [69] In this context resides the motivation to find a

suitable strategy for the production of high performance and sustainable lignocellulosic (peanut shells)-derived hard carbon as anode for SIBs. In this work, the impact of the acid activation is studied, revealing a direct correlation between the acid treatment time and the electrochemical performance as anode in SIBs. Additionally, a long acid treatment enables the use of lower synthesis temperature, thus making the hard carbon production greener and more sustainable. Based on this new knowledge, a carbon anode is designed with an optimized synthesis procedure and a very promising rate capability of 122 mAh $g^{-1}$ at 10 C (2 A $g^{-1}$), which is an excellent performance compared with other methods[123,227,256].

## 5.2 Experimental section

### *5.2.1. Synthesis of biomass-derived hard carbon*

Grinded and dried (60°C) peanut shells (lignocellulosic precursor) were used as collected or subjected to acid treatment using phosphoric acid (85%) for 1 day, 6 days and 3 months. The peanut shell/phosphoric acid weight ratio was 14% (25g peanut shells in 100 mL phosphoric acid). The resulting materials were grinded with mortar and pestle and dried at 60°C. Following the precursors were carbonized at 1100℃ (heating rate 1℃ $min^{-1}$) under Argon flow for one hour in a Nabertherm P330 tube furnace with a rated power of 1.2 kW. Accordingly, the obtained materials are named LHC_0D, LHC_1D, LHC_6D and LHC_3M.

The LHC_$2W_{800}$ material was obtained following the same procedure, but with a thermal treatment at 800 ℃.

### *5.2.2. Material characterization*

The structure and morphology of the hard carbon materials were investigated by means of X-ray diffraction (XRD, Bruker D8 Advance diffractometer with Cu Kα radiation) and scanning electron microscopy (SEM, Zeiss Auriga®). The materials surface area and pore width were determined by nitrogen adsorption measurements accordinng to the Brunauer-Emmett-Teller (BET) method, using an ASAP 2020 (Accelerated Surface Area and Porosimetry Analyzer, Micrometrics). $N_2$ absorption-desorption isotherms of samples were determined and analyzed by Autosorb-iQ, Quantachrome. Raman measurements were performed with a confocal InVia Raman micro spectrometer with a 633 nm laser (Renishaw; each spectrum was taken as the average of three 10-second accumulations). Thermo Gravimetric Analysis (TG) was performed with a NETZSCH Libra® TG 209 F1 coupled with a mass spectrometer NETZSCH QMS 403D Aëolos®.

2D WAXS measurements were performed at a sample to detector distance of 6 cm using a Bruker Nanostar Small Angle Scattering (SAXS) instrument with evacuated beam path, Cu tube source (K-α1 + K-α2), and equipped with a 2048*2048 pixels 2D Vantec 2000 detector. WAXS data were corrected for flat field and spatial distortion.

### *5.2.3. Electrode preparation and cell assembly*

Electrodes were prepared with a dry composition of 80 wt.% hard carbon, 10 wt.% conductive carbon (SuperC65®, Imerys) and 10 wt.% sodium carboxymethyl cellulose (CMC, WALOCEL®CRT 2000 PPA 12, Dow Wolff Cellulosics). LHC_$2W_{800}$ electrodes were also made with a larger conductive carbon content (i.e., 70 wt.% hard carbon, 20 wt.% conductive carbon and 10 wt.%. CMC) and are named LHC_opt.

First, CMC was dissolved in deionized water to obtain a 5 wt.% solution. The conductive additive and hard carbon were added into the solution and the resulting mixture was dispersed via ball milling for 2.5 h (70 min and 10 min rest; 1 repetition; speed main disk: 400 rpm; speed rotating planets: -800 rpm). The obtained slurries (solid content: 14.3 %; wet thickness of 150 µm) were casted with a doctor blade on dendritic copper foil at room temperature. Afterwards the coated electrodes were dried at 80℃ for 10 minutes and then at room temperature overnight under ambient atmosphere. Disk electrodes (Ø = 12 mm) were punched and dried for 2 h at 20℃ and 10 h at 150 ℃ under vacuum in a glass oven. The average active material mass loading of the electrodes is around 1.5 mg $cm^{-2}$.

### *5.2.4 Electrochemical characterization*

Three-electrode Swagelok® cells were assembled using each of the various hard carbon electrodes as the working electrode (WE) and sodium metal (99.8%, Acros Organics) as the counter (CE) and reference (RE) electrodes. All potential values given in this manuscript refer to the $Na/Na^+$ quasi-reference electrode. Whatman® glass fiber GF/D disks were used as separator and soaked with 240 µL of electrolyte (1M $NaClO_4$ in EC: PC (1:1 wt.%)). Sodium perchlorate $NaClO_4$ (98% Sigma Aldrich) propylene carbonate (PC, Sigma Aldrich), and ethylene carbonate (EC, UBE) were used as received. Electrolyte preparation and cell assembly were carried out in a glove box (MBraun) with oxygen and water contents below 0.1 ppm.

Galvanostatic cycling tests, between 0.02 V and 2.0 V (vs $Na/Na^+$), were carried out with a battery tester (Maccor series 4000, U.S.A). The specific current of 200 mA $g^{-1}$ is defined as 1 C. All electrochemical tests were performed in climatic chambers at 20 ± 1 °C.

## 5.3. Results and discussions

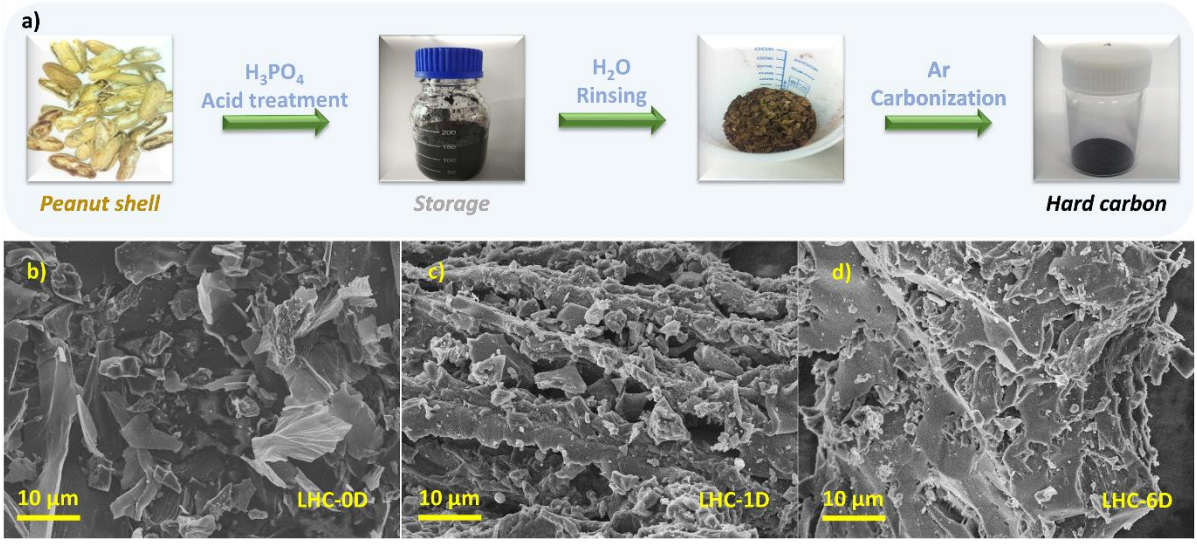


**Figure 5-1.** (a) Schematic of the synthesis method for hard carbons derived from peanut shells. See experimental section for further details. SEM images of b) LHC_0D, c) LHC_1D and d) LHC_6D.

Hard carbons were synthesized from peanut shells following the synthesis route shown in **Figure 5-1**. The peanut shells were either used as collected or soaked in phosphoric acid for 1 day and 6 days. The carbonization was performed at 1100 °C under Ar. Accordingly, the samples are named LHC_0D, LHC_1D, and LHC_6D, respectively. For comparison purposes, the earlier reported results obtained from peanut shells soaked for two weeks (LHC_2W) are also used in this manuscript[70].

The SEM images in **Figure 5-1** reveal the acid treatment impact on the morphology of the resulting hard carbon. LHC_0D (see **Figure 5-1b**), shows large particles still reflecting the original flake-like structure of the biomass precursor. The short term acid treatment, 1 day, strongly influences the morphology, as reported in **Figure 5-1c**. Indeed, the former structure characterizing the precursor is lost while several small

particles adhering to carbonized fibers are detected. A 6-days acid treatment leads to the disappearance of the small particles, still detected in LHC_1D (see **Figure 5-1d**), resembling the morphology of the 2 weeks acid treated sample (SEM images of LHC_2W are reported elsewhere). [70]

The different morphologies resulting from the various acid treatments, can be explained considering that peanut shells are composed of different polymer components including lignin (27-40 wt.%), cellulose (34-45 wt.%), and hemicellulose, and other components including proteins, inorganic salts, among others.[213,258] These components have different chemical stability towards phosphoric acid, which results in a step-wise components decomposition upon treatment time.[259] In particular, short process times mainly lead to disaggregation of the bio-structure (characterized by low acid stability) into small particles while prolonged treatments cause the removal and/or dissolution of more stable components.

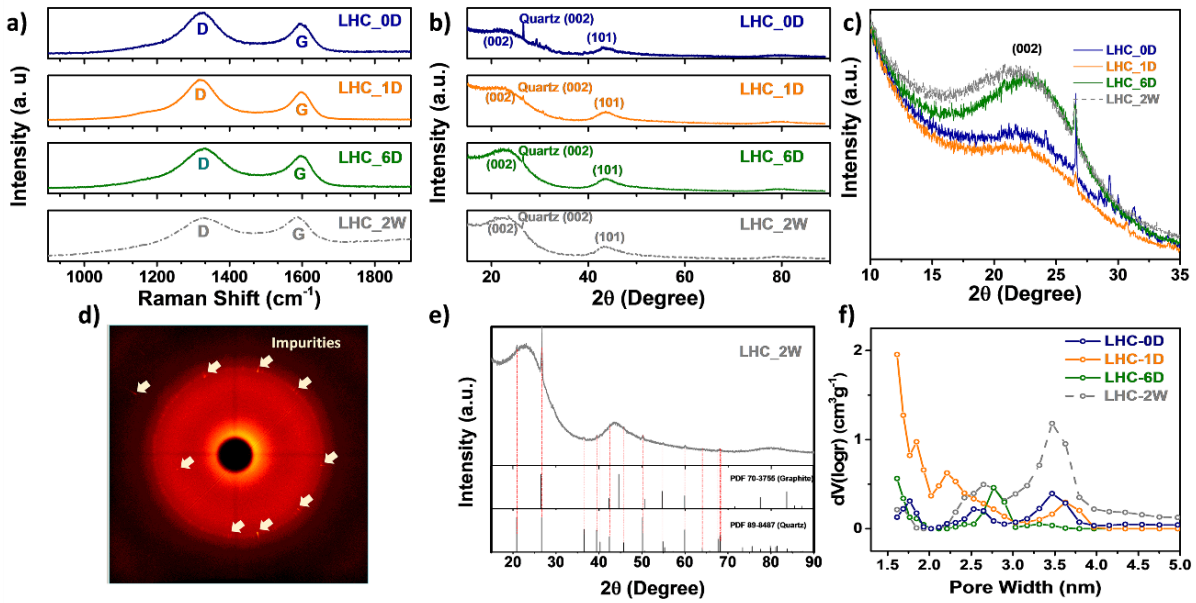


**Figure 5-2**. Structural characterization of LHC_0D, LHC_1D and LHC_6D compared with LHC_2W[70]. Comparison of Raman spectra (a), X-ray diffraction patterns (b) and normalized XRD patterns between a 2θ ranges from 10° to 35° (c). 2D plot for the

WAXS measurement (d) and XRD assignment (e) for LHC_2W. Comparison of DFT pore size distribution (f).

The synthesised hard carbons were characterized by Raman spectroscopy, XRD and DFT pore size analysis (**Figure 5-2 a-c)**. The gained information is summarized in **Table 5-1.**

**Table 5-1.** Characteristics of LHC_0D, LHC_1D, LHC_6D and compered with LHC_2W[70]

| | *LHC_0D* | *LHC_1D* | *LHC_6D* | *LHC_2W* |
|---|---|---|---|---|
| $I_D/I_G$ | **1.30** | **1.41** | **1.20** | **0.98** |
| **BET surface area ($m^2$ $g^{-1}$)** | **806** | **1127** | **445** | **29** |

By comparing the Raman spectra of the carbonized materials (see **Figure 5-2a**), it is seen that the $I_D/I_G$ ratio increased from 1.30 to 1.41, which indicates for a higher disorder degree most likely related to structural edges defects induced by the acid treatment. However, with longer acid treatments prior carbonisation, the $I_D/I_G$ ratio decreased to 1.20 (LHC_6D) and 0.98 (LHC_2W). This interesting finding indicates that long acid treatments improve the structural order of the carbonized material in a similar manner high annealing temperatures do, leading to a change of the structure from highly disordered to planar pseudo-graphitic microlites (higher pseudo-graphitic content)[157,174,228]. Thus, the acid treatment constitutes a valid alternative to the use of high carbonisation temperatures. The XRD analysis performed on the investigated

hard carbons (**Figure 5-2b),** enables the identification of impurities. As a matter of the fact, the XRD pattern of LHC_0D presents several peaks attributable to the presence of impurities such as $CaCO_3$ and $KCO_3$[230]. Similarly, LHC_1D shows detectable traces of inorganic impurities, while for the other hard carbons no impurities are detected, suggesting that the acid treatment process also induces a purification of the bio-derived hard carbon.

**Figure 5-2c** compares the 002 reflections of all materials showing that their intensity increases with increasing acid activation time. This indicates a higher crystallization in a similar fashion to that reported for increasing carbonization temperatures of hard carbons.[260] All three hard carbons show a peak at about 26.5° which is also observed for LHC_2W. Previous studies on carbon derived from peanut shells[70,261] and banana peels[71] also report a peak occurring in the same position, and assigned it to graphite. However, the 2D plots of SAXS (small-angle X-ray scattering) reported in **Figure 5-2d,** reveal clear individual impurity diffraction spots, thus indicating that the sharp peak at about 26.5° is related to small crystalline particles rather than the carbon structure (graphitic structure). As a matter of the fact, the assignment of the XRD reflections shown in **Figure 5-2e** clearly indicates that such a peak matches quartz (PDF 89-8487) very well, but not graphite (PDF 70-3755).

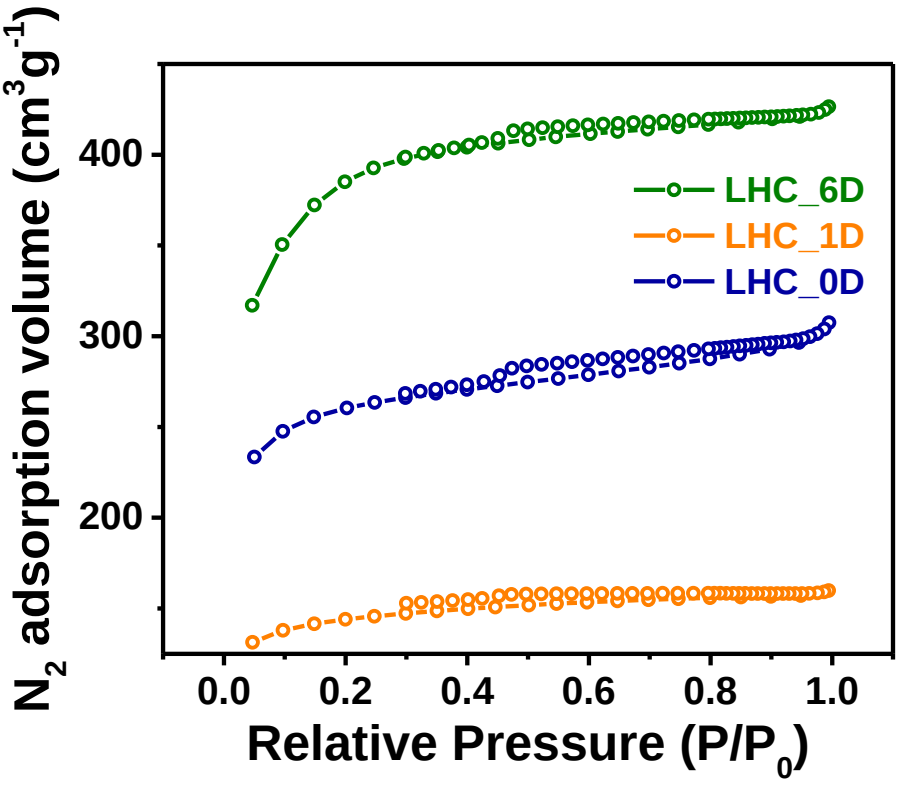


**Figure 5-3**. Nitrogen adsorption–desorption isotherms of LHC_0D, LHC_1D and LHC_6D

The nitrogen adsorption-desorption isotherms of the as-prepared hard carbons (see **Figure 5-3)** show isotherms assignable to a mix between type I and type IV[231], indicating that the three hard carbons are mostly characterized by a microporous character, but with the presence of mesopores. The resulting BET surface area is reported in **Table 5-1**. It is interestingly found that after one day of acid activation (LHC_1D), the surface area is increasing when compared with the untreated sample (LHC_0D), while with longer acid treatment (LHC_6D and LHC_2W) the surface area decreases with the treatment time. **Figure 5-2f** compares the DFT pore size distribution of LHC_0D, LHC_1D, LHC_6D with that of the LHC_2W[70]. LHC_0D shows a similar pore size distribution to LHC_2W, exhibiting two main contributions with pore size diameter at around 2.5 nm and 3.5 nm. After one day acid treatment (LHC_1D),

the content of pores with diameter ranging from 1.5 nm to 2.5 nm strongly increases, which is in good agreement with the well-known ability of phosphoric acid to generate microporosity.[262] When the acid treatment is prolonged to 6 days, the balance between micropores and mesopores changes, with the former decreasing as the later increases, and the trend persists also after 2 weeks of acid treatment (LCH_2W)[70]. To summarize, short term acid activation leads to highly microporous hard carbons, while longer acid activations tend to induce micropore closure, as reported by early studies via increasing carbonization temperature[88,263,264]. It is worth noting that the phosphoric acid activation is reported to increase the pore size from micropore to mesopore in lignocellulosic biomass derived carbons.[262,265,266] Hence, longer acid activation treatments can induce more mesopore but less micropore via pore closure and/or pore expansion, which is a similar effect on the porosity as it is reported for increasing carbonization temperatures.

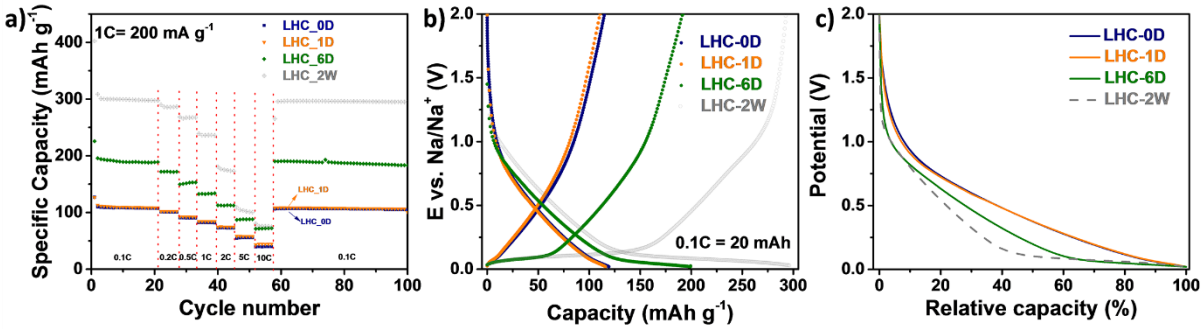


**Figure 5-4.** Comparison of the electrochemical performance of LHC_0D, LHC_1D, LHC_6D and compared with LHC_2W.[70] (a) Long-term cycling performance at various C-rates, (b) sodiation and desodiation profiles versus specific capacity and (c) sodiation profiles versus relative capacity. The last two panels refer to the 5$^{th}$ cycle in panel a (0.1 C-rate).

The long-term cycling performance at various C-rates of the investigated hard carbons is shown in **Figure 5-4a**. The associated coulombic efficiencies are shown in **Figure 5-5**. While the low rate (0.1C) capacity delivered by LHC_0D overlaps that of LHC_1D, a neat increase is observed with the materials exposed to longer acid treatments. In fact, LHC_6D and LHC_2W delivered twice and three time the capacity of the untreated (LHC_0D) and shortly acid treated (LHC-1D) materials. Such a large performance difference decreased, however, upon increasing C-rates. In fact, at 10 C rate all materials delivered the same, but rather low, capacity.

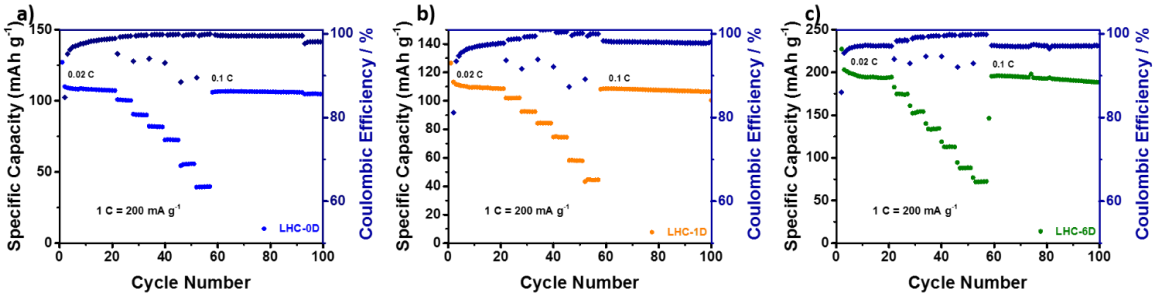


**Figure 5-5.** Long-term cycling performance at various C-rates of (a) LHC_0D, (b) LHC_1D and (c) LHC_6D.

Thus, longer acid treatment times substantially improve the specific capacity at low and intermediate current rates, but with limited benefit at high rates. The potential profiles of all materials at the 5$^{th}$ cycle (see **Figure 5-4b**) clearly evidence the occurrence of the low voltage plateau only in the materials subjected to longer acid treatments. On the other hand, LHC_0D and LHC_1D show almost overlapping potential profiles with a clear lack of the typical low voltage plateau typically observed in hard carbons, as better evidenced in **Figure 5-5c** where the sodiation profile of the materials are reported versus the relative capacity. The longer acid treatment leads to a substantial change in the voltage profile versus capacity plot, which is dominated by

the low voltage plateau for the materials exposed to the longest acid treatment (LHC_2W). On the other hand, only a slight capacity difference is observed in the sloping voltage profile region, indicating that the acid treatment does not strongly affect the sodium storage capacity in such a region. Indeed, the four carbon anodes present comparable potential profile in the sloping region.

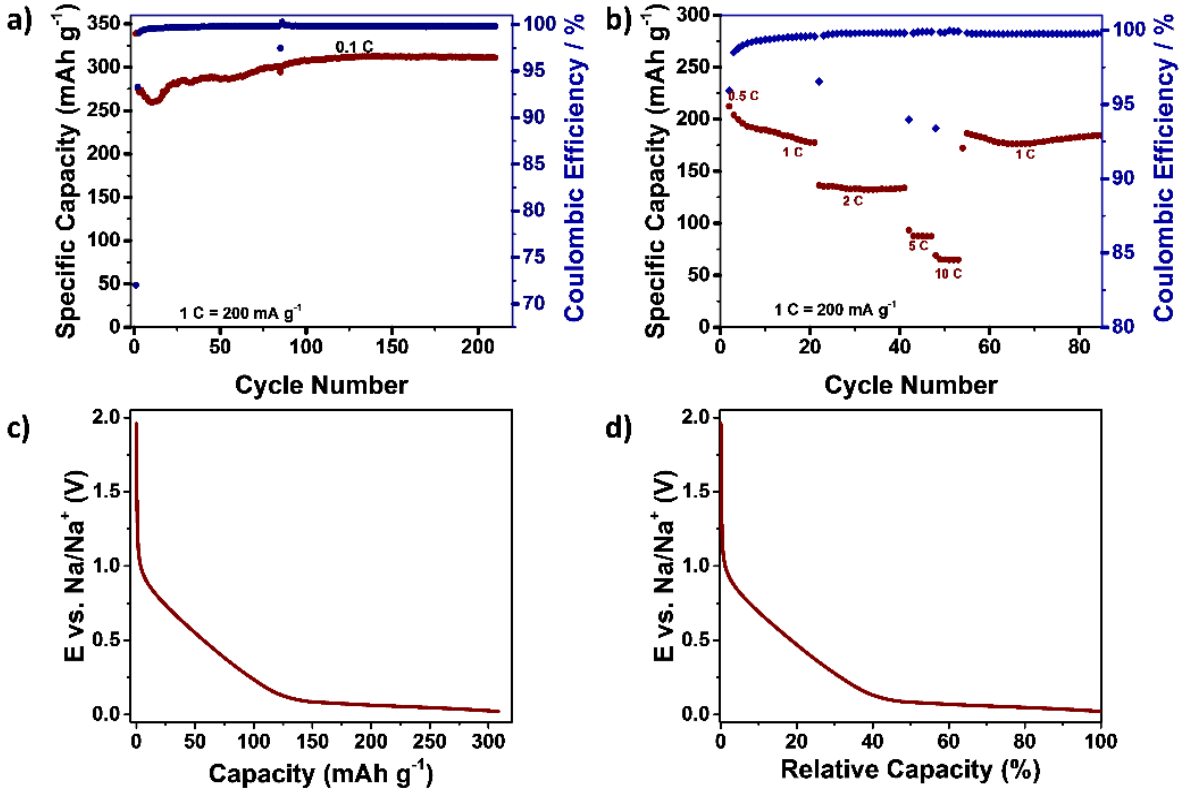


**Figure 5-6.** Electrochemical performance of LHC_3M. (a) Long-term cycling performance at constant C-rate (0.1C); (b) Delivered capacity at various C-rates; sodiation potential profile during the 150$^{th}$ cycle at 0.1 C-rate versus (c) specific capacity and (d) relative capacity.

Interestingly, when the acid treatment is prolonged to three months, the resulting hard carbon material showed a slightly higher specific capacity at 150$^{th}$ cycle than LHC_2W

(308 mAh $g^{-1}$ versus 298 mAh $g^{-1}$) when cycled at 0.1 C, however, with inferior rate capability and capacity retention (see **Figure 5-6**). This confirms that, in general, a prolonged acid treatment of the peanut shells precursor strongly affects the low rate delivered capacity, but not the high rate performance. Also, the limited additional capacity gained with the three months exposure to acid suggests two weeks as the optimal time for the activation process to occur.

Several studies investigated correlation between the carbonisation temperature of hard carbons from bio-waste and their electrochemical performance as anodes in SIBs. The general trend observed implies a linear correlation between the carbonisation temperature and the amount of $Na^+$ ions uptake in the low voltage region, which is the higher the temperature the longer is the low voltage plateau.[67,83,90,228] Interestingly, the acid treatment appears to exert the same effect, making feasible the synthesis of hard carbon materials for SIBs' anodes from lignocellulosic bio-waste at lower temperatures.

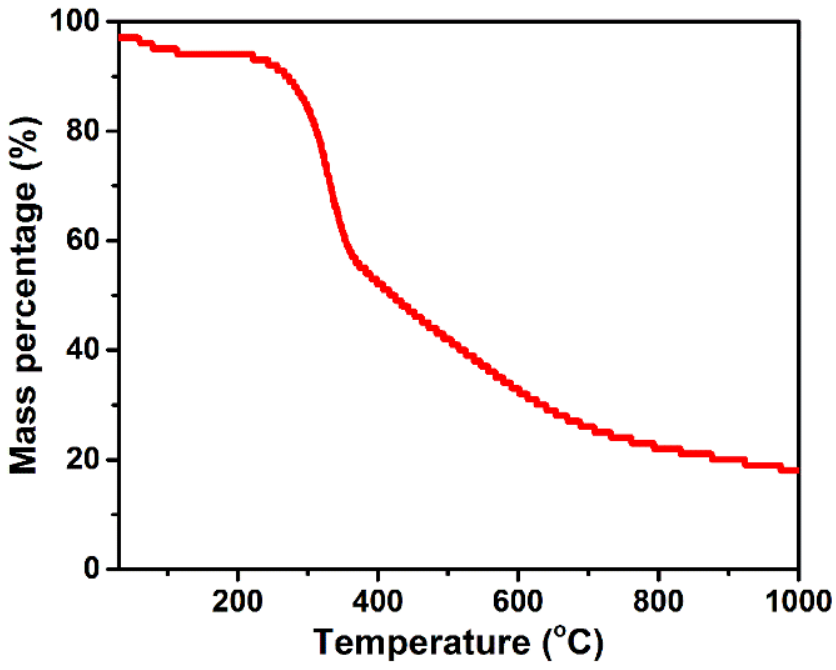

**Figure 5-7**. TGA (RT-1000 °C, 10 K $min^{-1}$, nitrogen medium) of the peanut shell precursor soaked in acid for 2 weeks.

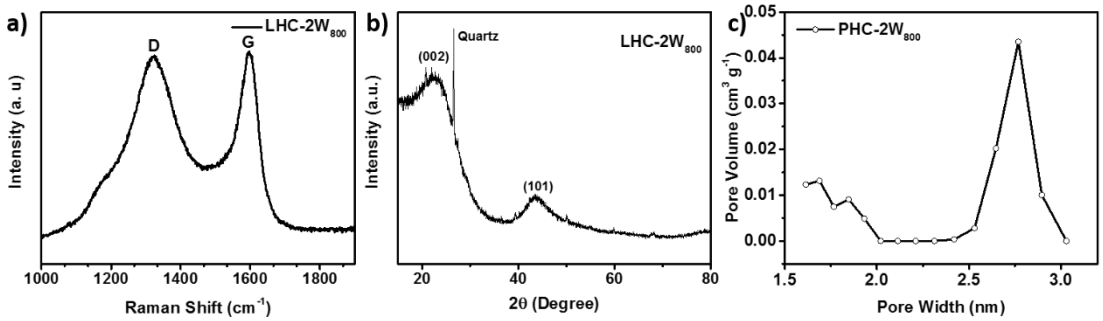


**Figure 5-8.** Structural characterization of LHC_2$W_{800}$: (a) Raman spectra, (b) X-ray diffraction pattern and (c) DFT pore size distribution.

To identify a suitable annealing temperature, TGA analysis coupled with mass spectrometry was performed on the precursor treated in phosphoric acid for two weeks. The results (see **Figure 5-7**) evidence a rather minor weight loss above 800 °C. Based on this observations, the carbonisation temperature was selected at 800 °C. The derived hard carbon material is named LHC_2$W_{800}$. Its physical characterization is reported in **Figure 5-8**. LHC_2$W_{800}$ shows similar $I_D/I_G$ ratio and position and intensity of the (002) reflection, but higher BET surface area and different DFT pore size distribution (i.e. smaller pores) like LHC_2$W^{70}$. Interestingly, LHC_2$W_{800}$ has similar pore size and surface area like LHC_6D, which was synthesized at higher carbonization temperature of 1100°C, but subjected to shorter acid treatment. Altogether, these evidences suggest that carbonization temperature and acid treatment time can have a similar effect on the porosity and the surface area of hard carbons.

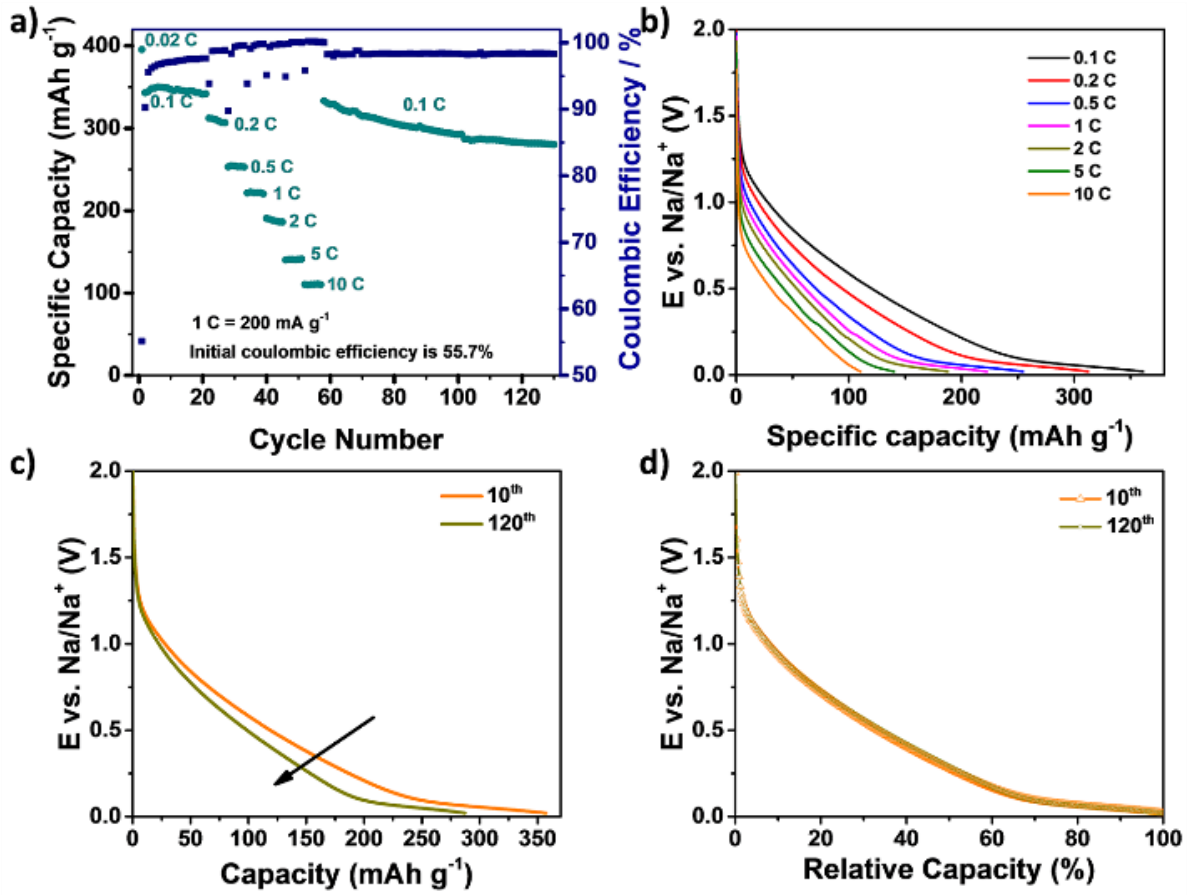


**Figure 5-9.** Rate capability (a) and sodiation potential profiles at selected current rate (b) of LHC_2W$_{800}$. Sodiation potential profiles (c) and relative potential profiles (d) of 10$^{th}$ and 120$^{th}$ cycle at 0.1C.

The electrochemical performance of LHC_2W$_{800}$ as anode material for SIBS is shown in **Figure 5-9**. Most of the reported studies on hard carbons annealed at temperature below or equal to 800 °C show limited electrochemical performance mostly deriving from the negligible low voltage plateau capacity[67,267]. The performance of LHC_2W$_{800}$ is, however, rather interesting due to the effects of the acid treatment. In fact, LHC_2W$_{800}$ shows specific capacities of 348 mAh g$^{-1}$, 306 mAh g$^{-1}$, 253 mAh g$^{-1}$, 221 mAh g$^{-1}$, 188 mAh g$^{-1}$, 140 mAh g$^{-1}$ and 110 mAh g$^{-1}$ at 0.1C, 0.2C, 0.5C, 1C, 2C, 5C and 10C, respectively. Additionally, its defective structure enables for a larger extent of the voltage slope region[86,135] leading to a better specific capacity at high current

rate[67,255]. At 10 C-rate, LHC_2W$_{800}$ uptakes $Na^+$ ions up to 110 mAh $g^{-1}$ against the 77 mAh $g^{-1}$ of LHC_2W. However, LHC_2W$_{800}$ shows a poor cycling stability due to the lower annealing temperature. In fact, after 120 cycles the specific capacity fades to only 283 mAh $g^{-1}$ (at 0.1C). The poor capacity retention upon cycling might have several reasons such as the relatively lower electronic conductive network, which is revealed by the steadily increasing IR-drop upon cycling (see **Figure 5-9c**), and/or the electrolyte decomposition caused by impurities[68,268–270]. To address the first issue, optimized electrodes (named LHC_opt) were made using 20 wt. % of conductive carbon additive. The related electrochemical performance of the LHC_opt electrodes is displayed in **Figure 5-10**.

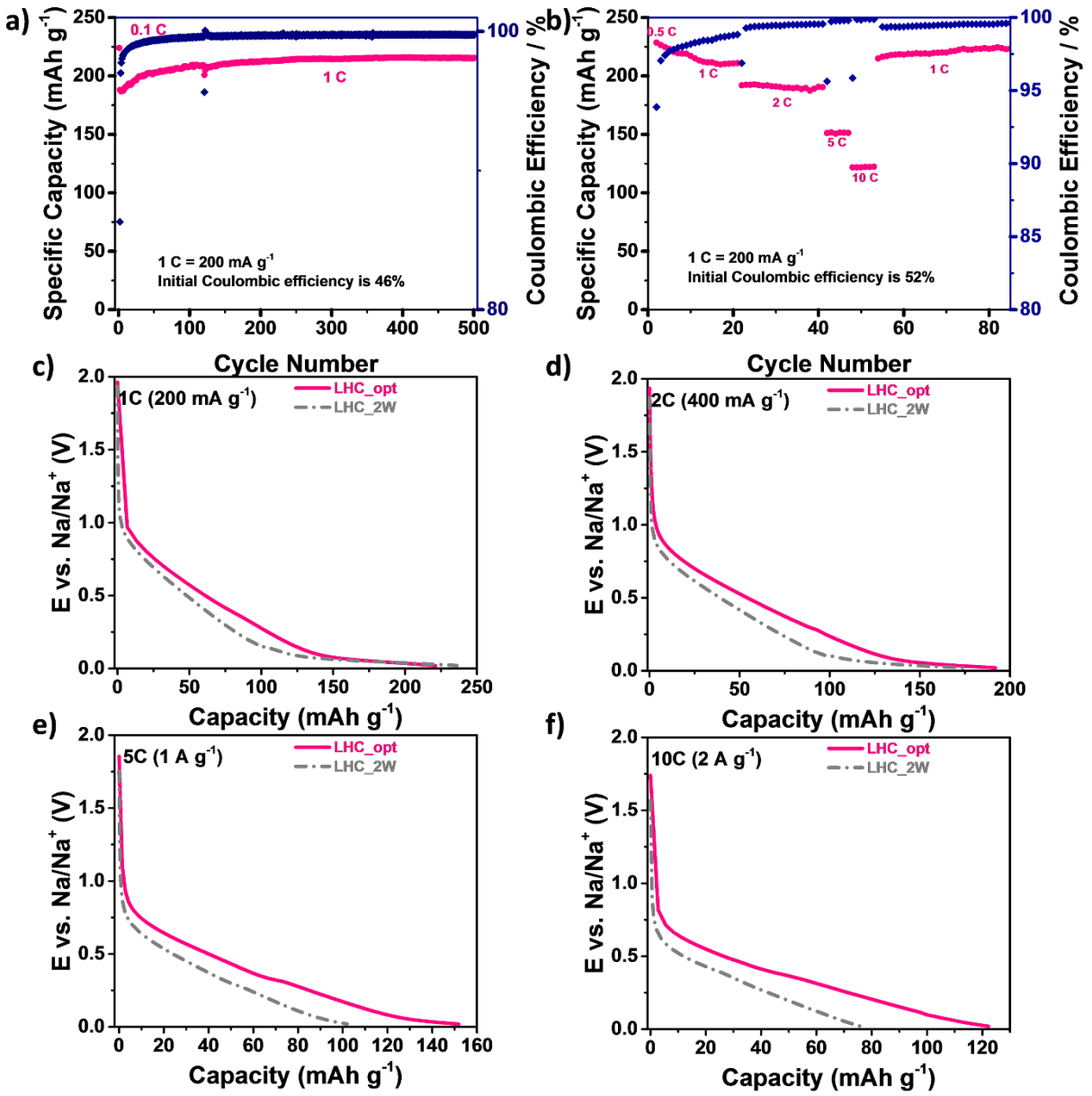


**Figure 5-10.** Gavanostatic cycling performance of LHC_opt: (a) long-cycling performance at 1C; (b) rate capability. Potential profiles of LHC_opt at selected current rates: (c) 1C; (d) 2C; (e) 5C and (f) 10C, compared with LHC-2W[70].

In particular, **Figure 5-10a** shows the long cycling performance at 1 C rate. In sharp contrast to the quick capacity fading of LHC_2W$_{800}$, LHC_opt shows an outstanding capacity retention (even an initial increase) up to 500 cycles, suggesting that the poor electronic conductivity is the reason for the poor cycling performance observed with

LHC_2W$_{800}$. **Figure 5-10b** illustrates the rate capability of LHC_opt, which is also compared to that of LHC_2W in **Figure 5-10(c-f)**. The sodiation capacity at 1C, 2C, 5C and 10C is 225 mAh $g^{-1}$, 193 mAh $g^{-1}$, 153 mAh $g^{-1}$ and 122 mAh $g^{-1}$ respectively. The comparison with the material carbonised at 1000°C (LHC_2W) shows that, with the exception of the lowest rate (1C), LHC_opt offers better $Na^+$ ion uptake performance. At the highest rate (10C), LHC_opt exhibits an uptake specific capacity of 122 mAh $g^{-1}$, which is 50% higher than that of LHC_2W (80 mAh $g^{-1}$). Also, the hard carbon annealed at 800 °C (LHC_opt) displayed a larger $Na^+$ ion uptake in the voltage slope region at all current densities, which results in its intrinsic safety towards the occurrence of Na metal plating on the electrode surface. Thus, the combination of long (two weeks) acid treatment and low temperature (800°C) carbonisation represents a valid strategy to synthesise high rate performance hard carbons for application as anode in SIBs. Although LHC_opt contains 20 wt.% of conductive carbon (see Experimental), however, it offers a better performance than LHC_2W even considering all carbonaceous material (i.e., hard carbon + carbon additive), which is 95 mAh $g^{-1}$ versus 65 mAh $g^{-1}$.

Since the cost of hard carbon from lignocellulosic precursors is mainly originating from the pyrolysis process, using a lower carbonisation temperature is greatly beneficial for the overall cost and sustainability[189]. Thus, in light of the reported results, the proposed synthesis represents a step further the sustainable and efficient production of hard carbon anodes for SIBs.

## 5.4. Summary

In this study, a suitable synthesis procedure to convert peanut shell bio-waste, i.e., a lignocellulosic biomass precursor, into hard carbons for application as high performance and sustainable anode materials in SIBs is reported. In particular, the impact of the acid treatment on the performance of the resulting hard carbons has been investigated in depth for the first time showing the existence of a strong correlation between the acid treatment's time and the $Na^+$ ion uptake characteristics. Hence, the acid treatment of the bio-waste precursor may be considered as an additional parameter to tailor the properties of hard carbons. In addition, it allows for lower carbonization temperatures, i.e., lower production cost, while yielding safer and better rate-performing anode materials, which uptake larger fractions of $Na^+$ ions in the voltage slope than in the low voltage plateau.

With this new knowledge, a more sustainable synthesis route (employing a long acid treatment, but lower annealing temperature with respect to that used for the untreated precursor) is proposed for the production of biomass-derived, high-rate hard carbon.

# 6. Conclusion

This thesis focused on the understanding and designing of sustainable hard carbon materials offering good electrochemical performance as anodes in sodium ion batteries.

Three important aspects of hard carbon anode materials were studied in detail.

The impact of different biomass waste sources on the structural properties and electrochemical performance of hard carbons is clarified in Chapter 3, unravelling and interlinking the properties of hard carbons with respect to the composition and structure of the biomass waste from which they are derived. In detail, a systematic structural and electrochemical investigation of hard carbons derived from three typical representatives of cellulosic biomass waste, namely corncobs (hemicellulose-linked), peanut shells (lignocellulose-linked) and waste apples (pectin-linked) is presented. The results show that a stable and reproducible electrochemical performance can be obtained for biowaste derived hard carbons. In particular, the hard carbon derived from peanut shells shows the best electrochemical performance with high specific capacities (298 mAh $g^{-1}$) and very high capacity retention (98% after 300 cycles). This performance is of great interest as lignocellulosic biomass waste cannot be recycled easily, e.g., it cannot be used for the generation of bio fuel.

The use of another industrial waste, pectin-free apple pomace, for the production of hard carbon was also pursued, finding that. it shows good electrochemical performance with high specific capacities (285 mAh $g^{-1}$) and high capacity retention (96% after 230 cycles). These results were far superior to those already reported in

the literature. The pectin-free apple pomace-derived hard carbon delivers a very competitive electrochemical performance with respect to the state-of-the-art anode material despite being synthesized from very cheap and abundant waste. Most importantly, the hard carbon exhibits a unique morphology and very interesting structural properties, which provided some insights in the sodium storage mechanism, i.e. the key roles of surface area and porosity.

Finally, the activation step (pre-treatment) of hard carbon precursors, which has a crucial effect on the electrochemical performance of the resulting material, was investigated. In particular, this study, dealing with the treatment of lignocellulosic materials in phosphoric acid, clarifies the impact of such a treatment on the structural properties and electrochemical performance of hard carbons, unravelling and interlinking the properties of the hard carbons to the structure of peanut shells for the first time. Hence, the acid treatment of the bio-waste precursor is identified as a key parameter to tailor the properties of hard carbons, allowing for lower carbonization temperatures, i.e., lower production cost, while yielding safer and better rate-performing anode materials compared with other recent results reported in the literature (122 mAh $g^{-1}$ vs. 76 mAh $g^{-1}$ at 10C).

# 7. Acknowledgement

This thesis would not be finished without the help and advice by many people. First of all, I would like to gratefully thank my supervisor, Professor Dr. Stefano Passerini, who kindly give me the opportunity to study and accomplish my PhD within his group. I highly appreciate his scientific support and trust during the whole process of my PhD study in Helmholtz Institute Ulm (HIU).I would like to express my gratitude also to Prof. Dr. Helmut Ehrenberg for being the second examiner of my thesis.

I would like to express many thanks to Dr. Daniel Buchholz, who introduced me the battery field to me from the very beginning. Dr. Buchholz, together with Dr. Ivana Hasa, whom I owe special gratitude to as well, explained and taught me in detail how to do and what to do in research.

Dr. Liming Wu, Dr. Guk-Tae Kim, Dr. Dominic Bresser, Tobias Eisenmann, Maral Hekmatfar, Katharina Thanner, Lucas Lodovico, Chenxi Geng, Dr. Luciana Gomes Chagas, Dr. Diogo Vieira Carvalho, Dr. Thomas Diemant and Dr. Damien Saurel, Dr. Ping Gao are acknowledged for their kind help and fruitful discussions for this thesis.

I would like to generally thank all of my colleagues for their support and the great atmosphere in the group.

I highly appreciate Dr. Markus Ding, Dr. Marlou Keller, Dr. Xinpei Gao, Dr. Nicholas Löffler, Dr. Christoph Vaalma, Yanjiao Ma and Yuan Ma for their time in exploring different countries and cities of the world with me, which coloured the whole period of my PhD.

I thank my mother, Ms. 金鑫 and my father, Mr. **窦延陆**, my grandparents (Ms.白桂兰, Ms. 蒋桂芳, Mr. 金绪臻) and all other family members for their love and support, Xie Xie.

# 8. Bibliography


(1) Nitta, N.; Wu, F.; Lee, J. T.; Yushin, G. Li-Ion Battery Materials: Present and Future. *Mater. Today* **2015**, *18* (5), 252–264.

(2) Palomares, V.; Serras, P.; Villaluenga, I.; Hueso, K. B.; Carretero-Gonzalez, J.; Rojo, T. Na-Ion Batteries, Recent Advances and Present Challenges to Become Low Cost Energy Storage Systems. *Energy Environ. Sci.* **2012**, *5* (3), 5884–5901.

(3) Vaalma, C.; Buchholz, D.; Passerini, S. Non-Aqueous Potassium-Ion Batteries: A Review. *Curr. Opin. Electrochem.* **2018**.

(4) Nishi, Y. The Development of Lithium Ion Secondary Batteries. *Chem. Rec.* **2001**, *1* (5), 406–413.

(5) Blomgren, G. E. The Development and Future of Lithium Ion Batteries. *J. Electrochem. Soc.* **2017**, *164* (1), A5019–A5025.

(6) Scrosati, B. History of Lithium Batteries. *J. Solid State Electrochem.* **2011**, *15* (7–8), 1623–1630.

(7) Yoshino, A. The Birth of the Lithium-Ion Battery. *Angew. Chemie Int. Ed.* **2012**, *51* (24), 5798–5800.

(8) Roberts, S.; Kendrick, E. The Re-Emergence of Sodium Ion Batteries: Testing, Processing, and Manufacturability. *Nanotechnol. Sci. Appl.* **2018**, *Volume 11*, 23–33.

(9) Zhang, H.; Hasa, I.; Passerini, S. Beyond Insertion for Na-Ion Batteries: Nanostructured Alloying and Conversion Anode Materials. *Adv. Energy Mater.* **2018**, *1702582*.

(10) Muñoz-Márquez, M. Á.; Saurel, D.; Gómez-Cámer, J. L.; Casas-Cabanas, M.; Castillo-Martínez, E.; Rojo, T. Na-Ion Batteries for Large Scale Applications: A Review on Anode Materials and Solid Electrolyte Interphase Formation. *Adv. Energy Mater.* **2017**, *1700463*, 1700463.

(11) Palomares, V.; Casas-Cabanas, M.; Castillo-Martínez, E.; Han, M. H.; Rojo, T. Update on Na-Based Battery Materials. A Growing Research Path. *Energy Environ. Sci.* **2013**, *6* (8), 2312.

(12) Wu, X.; Leonard, D. P.; Ji, X. Emerging Non-Aqueous Potassium-Ion Batteries: Challenges and Opportunities. *Chem. Mater.* **2017**, *29* (12), 5031–5042.

(13) Zou, X.; Xiong, P.; Zhao, J.; Hu, J.; Liu, Z.; Xu, Y. Recent Research Progress in Non-Aqueous Potassium-Ion Batteries. *Phys. Chem. Chem. Phys.* **2017**, *19* (39), 26495–26506.

(14) Nayak, P. K.; Yang, L.; Brehm, W.; Adelhelm, P. From Lithium-Ion to Sodium-Ion Batteries: Advantages, Challenges, and Surprises. *Angew. Chemie Int. Ed.* **2018**, *57* (1), 102–120.

(15) Kubota, K.; Komaba, S. Review—Practical Issues and Future Perspective for Na-Ion Batteries. *J. Electrochem. Soc.* **2015**, *162* (14), A2538–A2550.

(16) Kuze, S.; Kageura, J.; Matsumoto, S.; Nakayama, T.; Makidera, M.; Saka, M.; Yamaguchi, T.; Yamamoto, T.; Nakane, K. *Development of a Sodium Ion Secondary Battery, Sumitomo Chemical Co., Ltd.*; 2013.

(17) Barker, J.; Heap, R. J.; Roche, N.; Tan, C.; Sayers, R.; Liu, Y. *Low Cost Na-Ion Battery Technology*; Faradion Limited Advanced Energy Storage Solutions, 2013.

(18) French Network RS2E. http://www.energie-rs2e.com/en/news/na-ion-batteries-promising-prototype.

(19) Hasa, I.; Buchholz, D.; Passerini, S.; Hassoun, J. A Comparative Study of Layered Transition Metal Oxide Cathodes for Application in Sodium-Ion Battery. *ACS Appl. Mater. Interfaces* **2015**, *7* (9), 5206–5212.

(20) Hasa, I.; Passerini, S.; Hassoun, J. Toward High Energy Density Cathode Materials for Sodium-Ion Batteries: Investigating the Beneficial Effect of Aluminum Doping on the P2-Type Structure. *J. Mater. Chem. A* **2017**, *5* (9), 4467–4477.

(21) Zhang, H.; Hasa, I.; Qin, B.; Diemant, T.; Buchholz, D.; Behm, R. J.; Passerini, S. Excellent Cycling Stability and Superior Rate Capability of Na3V2(PO4)3 Cathodes Enabled by Nitrogen-Doped Carbon Interpenetration for Sodium-Ion Batteries. *ChemElectroChem* **2017**, *2*.

(22) Zhang, H.; Hasa, I.; Buchholz, D.; Qin, B.; Passerini, S. Effects of Nitrogen Doping on the Structure and Performance of Carbon Coated Na3V2PO43cathodes for Sodium-Ion Batteries. *Carbon N. Y.* **2017**, *124*, 334–341.

(23) Han, M. H.; Gonzalo, E.; Singh, G.; Rojo, T. A Comprehensive Review of Sodium Layered Oxides: Powerful Cathodes for Na-Ion Batteries. *Energy Environ. Sci.* **2015**, *8* (1), 81–102.

(24) Masquelier, C.; Croguennec, L. Polyanionic (Phosphates, Silicates, Sulfates) Frameworks as Electrode Materials for Rechargeable Li (or Na) Batteries. *Chem. Rev.* **2013**, *113* (8), 6552–6591.

(25) Hasa, I.; Hassoun, J.; Passerini, S. Nanostructured Na-Ion and Li-Ion Anodes for Battery Application: A Comparative Overview. *Nano Res.* **2017**, *10* (12), 3942–3969.

(26) Hasa, I.; Verrelli, R.; Hassoun, J. Transition Metal Oxide-Carbon Composites as Conversion Anodes for Sodium-Ion Battery. *Electrochim. Acta* **2015**, *173*, 613–618.

(27) Dahbi, M.; Yabuuchi, N.; Kubota, K.; Tokiwa, K.; Komaba, S. Negative Electrodes for Na-Ion Batteries. *Phys. Chem. Chem. Phys.* **2014**, *16* (29), 15007.

(28) Luo, W.; Shen, F.; Bommier, C.; Zhu, H.; Ji, X.; Hu, L. Na-Ion Battery Anodes: Materials and Electrochemistry. *Acc. Chem. Res.* **2016**, *49* (2), 231–240.

(29) Ponrouch, a.; Monti, D.; Boschin, a.; Steen, B.; Johansson, P.; Palacín, M. R. Non-Aqueous Electrolytes for Sodium-Ion Batteries. *J. Mater. Chem. A* **2015**, *3* (1), 22–42.

(30) Ponrouch, A.; Marchante, E.; Courty, M.; Tarascon, J.-M.; Palacín, M. R. In Search of an Optimized Electrolyte for Na-Ion Batteries. *Energy Environ. Sci.* **2012**, *5* (9), 8572.

(31) Hasa, I.; Passerini, S.; Hassoun, J. Characteristics of an Ionic Liquid Electrolyte for Sodium-Ion Batteries. In *Journal of Power Sources*; 2016; Vol. 303, pp 203–207.

(32) Monti, D.; Jònsson, E.; Palacìn, M. R.; Johansson, P. Ionic Liquid Based Electrolytes for Sodium-Ion Batteries: Na+ Solvation and Ionic Conductivity. *J. Power Sources* **2014**, *245*, 630–636.

(33) Goodenough, J. B. U.S. Patent 4,302,518 (Issued 1980/3/31).

(34) H. Ikeda, K. Narukawa, H. N. Japanese Patent 1769661 (Issued 1981/6/18).

(35) Nishi, Y. Past, Present and Future of Lithium-Ion Batteries. In *Lithium-Ion Batteries*; Elsevier, 2014; pp 21–39.

(36) Nobuhara, K.; Nakayama, H.; Nose, M.; Nakanishi, S.; Iba, H. First-Principles Study of Alkali Metal-Graphite Intercalation Compounds. *J. Power Sources* **2013**, *243*, 585–587.

(37) Fredenhagen, K.; Cadenbach, G. Die Bindung von Kalium Durch Kohlenstoff. *Zeitschrift für Anorg. und Allg. Chemie* **1926**, *158* (1), 249–263.

(38) Rüdorff, W.; Schulze, E. Über Alkaligraphitverbindungen. *Zeitschrift für Anorg. und Allg. Chemie* **1954**, *277* (3–4), 156–171.

(39) Jache, B.; Adelhelm, P. Use of Graphite as a Highly Reversible Electrode with Superior Cycle Life for Sodium-Ion Batteries by Making Use of Co-Intercalation Phenomena. *Angew. Chemie - Int. Ed.* **2014**, *53* (38), 10169–10173.

(40) Kim, H.; Hong, J.; Yoon, G.; Kim, H.; Park, K.-Y.; Park, M.-S.; Yoon, W.-S.; Kang, K. Sodium Intercalation Chemistry in Graphite. *Energy Environ. Sci.* **2015**, *8* (10), 2963–2969.

(41) Wan, W.; Wang, H. Study on the First-Principles Calculations of Graphite Intercalated by Alkali Metal (Li, Na, K). *Int. J. Electrochem. Sci.* **2015**, *10* (4), 3177–3184.

(42) Liu, Y.; Merinov, B. V.; Goddard, W. A. Origin of Low Sodium Capacity in Graphite and Generally Weak Substrate Binding of Na and Mg among Alkali and Alkaline Earth Metals. *Proc. Natl. Acad. Sci.* **2016**, *113* (14), 3735–3739.

(43) Okamoto, Y. Density Functional Theory Calculations of Alkali Metal (Li, Na, and K) Graphite Intercalation Compounds. *J. Phys. Chem. C* **2014**, *118* (1), 16–19.

(44) Metrot, A.; Guerard, D.; Billaud, D.; Herold, A. New Results about the Sodium-Graphite System. *Synth. Met.* **1980**, *1* (4), 363–369.

(45) Avdeev, V. V.; Nalimova, V. A.; Semenenko, K. N. Sodium-Graphite System at High Pressures. *Synth. Met.* **1990**, *38* (3), 363–369.

(46) Sleppy, W. C. Reaction of Sodium with Graphite at 400°. *Inorg. Chem.* **1966**, *5* (11), 2021–2023.

(47) Hasa, I.; Dou, X.; Buchholz, D.; Shao-Horn, Y.; Hassoun, J.; Passerini, S.; Scrosati, B. A Sodium-Ion Battery Exploiting Layered Oxide Cathode, Graphite Anode and Glyme-Based Electrolyte. *J. Power Sources* **2016**, *310*, 26–31.

(48) Klein, F.; Jache, B.; Bhide, A.; Adelhelm, P. Conversion Reactions for Sodium-Ion Batteries. *Phys. Chem. Chem. Phys.* **2013**, *15* (38), 15876–15887.

(49) Zuo, X.; Zhu, J.; Müller-Buschbaum, P.; Cheng, Y.-J. Silicon Based Lithium-Ion Battery Anodes: A Chronicle Perspective Review. *Nano Energy* **2017**, *31* (October 2016), 113–143.

(50) Feng, K.; Li, M.; Liu, W.; Kashkooli, A. G.; Xiao, X.; Cai, M.; Chen, Z. Silicon-Based Anodes for Lithium-Ion Batteries: From Fundamentals to Practical Applications. *Small* **2018**, *14* (8).

(51) Komaba, S.; Matsuura, Y.; Ishikawa, T.; Yabuuchi, N.; Murata, W.; Kuze, S. Redox Reaction of Sn-Polyacrylate Electrodes in Aprotic Na Cell. *Electrochem. commun.* **2012**, *21* (1), 65–68.

(52) Dou, X.; Buchholz, D.; Weinberger, M.; Diemant, T.; Kaus, M.; Indris, S.; Behm, R. J.; Wohlfahrt-Mehrens, M.; Passerini, S. Study of the Na Storage Mechanism in Silicon Oxycarbide-Evidence for Reversible Silicon Redox Activity. *Small Methods* **2018**, 1800177.

(53) Yabuuchi, N.; Kubota, K.; Dahbi, M.; Komaba, S. Research Development on Sodium-Ion Batteries. *Chaical Rev.* **2014**.

(54) Hwang, J.-Y.; Myung, S.-T.; Sun, Y.-K. Sodium-Ion Batteries: Present and Future. *Chem. Soc. Rev.* **2017**, *46* (12), 3529–3614.

(55) Doeff, M. M.; Ma, Y.; Visco, S. J.; Jonghe, L. C. De. Electrochemical Insertion of Sodium into Carbon. **1993**, *140* (12), 169–170.

(56) Stevens, D. A.; Dahn, J. R. High Capacity Anode Materials for Rechargeable Sodium-Ion Batteries. *J. Electrochem. Soc.* **2000**, *147* (4), 1271.

(57) Mabuchi, A. A Survey on the Carbon Anode Materials for Rechargeable Lithium Batteries. *Tanso* **1994**, *165*, 298–306.

(58) Stevens, D. A. Mechanisms for Sodium Insertion in Carbon Materials, Dalhousie University, 2000.

(59) Sorlie, M. .; Oye, H. A. 1989,625. *Light Met.* **1989**, *625*.

(60) Nixon. J. C. Bull. Proc. Australas. Inst. Min. Metall. 1987,292, 85. *J. C. Bull. Proc. Australas. Inst. Min. Met.* **1987**, *292*, 85.

(61) Ma, Y.; Doeff, M. M.; Visco, S. J.; Jonghe, L. C. De. Rechargeable Na / NaxCo02 and NalsPb4 / NaxCo02 Polymer Electrolyte Cells. *J. Electrochem. Soc.* **1993**, *140* (10), 2726–2733.

(62) Stevens, D. A.; Dahn, J. R. The Mechanisms of Lithium and Sodium Insertion in Carbon Materials. *J. Electrochem. Soc.* **2001**, *148* (8), A803.

(63) Thomas, P.; Billaud, D. Sodium Electrochemical Insertion Mechanisms in Various Carbon Fibres. *Electrochim. Acta* **2001**, *46* (22), 3359–3366.

(64) Alcántara, R.; Lavela, P.; Ortiz, G. F.; Tirado, J. L. Carbon Microspheres Obtained from Resorcinol-Formaldehyde as High-Capacity Electrodes for Sodium-Ion Batteries. *Electrochem. Solid-State Lett.* **2005**, *8* (4), A222.

(65) Balogun, M. S.; Luo, Y.; Qiu, W.; Liu, P.; Tong, Y. A Review of Carbon Materials and Their Composites with Alloy Metals for Sodium Ion Battery Anodes. *Carbon N. Y.* **2016**, *98*, 162–178.

(66) Bommier, C.; Mitlin, D.; Ji, X. Internal Structure – Na Storage Mechanisms – Electrochemical Performance Relations in Carbons. *Prog. Mater. Sci.* **2018**, *97*, 170–203.

(67) Wahid, M.; Puthusseri, D.; Gawli, Y.; Sharma, N.; Ogale, S. Hard Carbons for Sodium-Ion Battery Anodes: Synthetic Strategies, Material Properties, and Storage Mechanisms. *ChemSusChem* **2018**, *11* (3), 506–526.

(68) Irisarri, E.; Ponrouch, A.; Palacin, M. R. Review—Hard Carbon Negative Electrode Materials for Sodium-Ion Batteries. *J. Electrochem. Soc.* **2015**, *162* (14), A2476–A2482.

(69) Saurel, D.; Orayech, B.; Xiao, B.; Carriazo, D.; Li, X.; Rojo, T. From Charge Storage Mechanism to Performance: A Roadmap toward High Specific Energy Sodium-Ion Batteries through Carbon Anode Optimization. *Adv. Energy Mater.* **2018**, *1703268*, 1–33.

(70) Dou, X.; Hasa, I.; Hekmatfar, M.; Diemant, T.; Behm, R. J.; Buchholz, D.; Passerini, S. Pectin, Hemicellulose, or Lignin? Impact of the Biowaste Source on the Performance of Hard Carbons for Sodium-Ion Batteries. *ChemSusChem* **2017**, *10* (12), 2668–2676.

(71) Memarzadeh Lotfabad, E.; Ding, J.; Cui, K.; Kohandehghan, A.; Kalisvaart, W. P.; Hazelton, M.; Mitlin, D.; Lotfabad, E. M.; Ding, J.; Cui, K.; Kohandehghan, A.; Kalisvaart, W. P.; Hazelton, M.; Mitlin, D. High Density Sodium and Lithium Ion Battery Anodes from Banana Peels. *ACS Nano* **2014**, *8* (7), 7115–7129.

(72) Hou, H.; Qiu, X.; Wei, W.; Zhang, Y.; Ji, X. Carbon Anode Materials for Advanced Sodium-Ion Batteries. *Adv. Energy Mater.* **2017**, *7* (24), 1–30.

(73) James J. McTighe. Manufacture of Hard Carbon. 338542, 1886.

(74) Harris, P. J. F. Rosalind Franklin's Work on Coal, Carbon, and Graphite. *Interdiscip. Sci. Rev.* **2001**, *3*, 204–210.

(75) Franklin, R. E. The Interpretation of Diffuse X-Ray Diagrams of Carbon. *Acta Crystallogr.* **1950**, *3* (2), 107–121.

(76) Franklin, R. E. The Structure of Graphitic Carbons. *Acta Crystallogr.* **1951**, *4* (3), 253–261.

(77) Franklin, R. E. Crystallite Growth in Graphitizing and Non-Graphitizing Carbons. *Proc. R. Soc. A Math. Phys. Eng. Sci.* **1951**, *209* (1097), 196–218.

(78) Dahn, J. R.; Zheng, T.; Liu, Y.; Xue, J. S. Mechanisms for Lithium Insertion in Carbonaceous Materials. *Science (80-. ).* **1995**, *270* (5236), 590–593.

(79) Marsh, H.; Rodríguez-Reinoso, F. *Active Carbon*; Elsevier, 2006; Vol. 44.

(80) Anderson, P. W. Absence of Diffusion in Certain Random Lattices. *Phys. Rev.* **1958**, *109* (5), 1492–1505.

(81) Hernndez-Montoya, V.; Garca-Servin, J.; José Iván Bueno-López. *Thermal Treatments and Activation Procedures Used in the Preparation of Activated Carbons, Lignocellulosic Precursors Used in the Synthesis of Activated Carbon - Characterization Techniques and Applications in the Wastewater Treatment*; Dr. Virginia Hernández Montoya, Ed.; InTech, 2012.

(82) Derbyshire, E. J.; Jagtoyen, M.; McEnaney, B.; Sethuraman, A. R.; Stencel, J. M.; Taulbee, D.; Thwaites, M. . W. The Production of Activated Carbons from Coals by Chemical Activation. *Fuel Div. Prepr. Am. Chem. Soc.* **1991**, *36*, 1072–1080.

(83) Zhang, B.; Ghimbeu, C. M.; Laberty, C.; Vix-Guterl, C.; Tarascon, J.-M. Correlation Between Microstructure and Na Storage Behavior in Hard Carbon. *Adv. Energy Mater.* **2016**, *6* (1), 1501588.

(84) Marsh, H. *Introduction to Carbon Science*, 1st ed.; Marsh, H., Ed.; Butterworths, 1989.

(85) Martynenko, A. True, Particle, and Bulk Density of Shrinkable Biomaterials: Evaluation from Drying Experiments. *Dry. Technol.* **2014**, *32* (11), 1319–1325.

(86) Li, Z.; Bommier, C.; Chong, Z. Sen; Jian, Z.; Surta, T. W.; Wang, X.; Xing, Z.; Neuefeind, J. C.; Stickle, W. F.; Dolgos, M.; Greaney, P. A.; Ji, X. Mechanism of Na-Ion Storage in Hard Carbon Anodes Revealed by Heteroatom Doping. *Adv. Energy Mater.* **2017**, *7* (18), 1602894.

(87) van Schalkwijk, W. A.; Scrosati, B. *Advances in Lithium-Ion Batteries*; Kluwer Academic Publishers, 2002.

(88) Buiel, E. R.; George, A. E.; Dahn, J. R. Model of Micropore Closure in Hard Carbon Prepared from Sucrose. *Carbon N. Y.* **1999**, *37* (9), 1399–1407.

(89) Wahid, M.; Gawli, Y.; Puthusseri, D.; Kumar, A.; Shelke, M. V.; Ogale, S. Nutty Carbon: Morphology Replicating Hard Carbon from Walnut Shell for Na Ion Battery Anode. *ACS Omega* **2017**, *2* (7), 3601–3609.

(90) Li, Y.; Paranthaman, M. P.; Akato, K.; Naskar, A. K.; Levine, A. M.; Lee, R. J.; Kim, S.-O.; Zhang, J.; Dai, S.; Manthiram, A. Tire-Derived Carbon Composite Anodes for Sodium-Ion Batteries. *J. Power Sources* **2016**, *316*, 232–238.

(91) Navarro-Suárez, A. M.; Saurel, D.; Sánchez-Fontecoba, P.; Castillo-Martínez, E.; Carretero-González, J.; Rojo, T. Temperature Effect on the Synthesis of Lignin-Derived Carbons for Electrochemical Energy Storage Applications. *J. Power Sources* **2018**, *397*, 296–306.

(92) Qiu, S.; Xiao, L.; Sushko, M. L.; Han, K. S.; Shao, Y.; Yan, M.; Liang, X.; Mai, L.; Feng, J.; Cao, Y.; Ai, X.; Yang, H.; Liu, J. Manipulating Adsorption-Insertion Mechanisms in Nanostructured Carbon Materials for High-Efficiency Sodium Ion Storage. *Adv. Energy Mater.* **2017**, *7* (17), 1700403.

(93) Harris, P. J. F. New Perspectives on the Structure of Graphitic Carbons. *Crit. Rev. Solid State Mater. Sci.* **2005**, *30* (4), 235–253.

(94) Li, Z.; Jian, Z.; Wang, X.; Rodríguez-Pérez, I. A.; Bommier, C.; Ji, X. Hard Carbon Anodes of Sodium-Ion Batteries: Undervalued Rate Capability. *Chem. Commun.* **2017**, *53* (17), 2610–2613.

(95) Stratford, J. M.; Allan, P. K.; Pecher, O.; Chater, P. A.; Grey, C. P. Mechanistic Insights into Sodium Storage in Hard Carbon Anodes Using Local Structure Probes. *Chem. Commun.* **2016**, *52* (84), 12430–12433.

(96) Harris, P. J. F. Fullerene-like Models for Microporous Carbon. *J. Mater. Sci.* **2013**, *48* (2), 565–577.

(97) Lusk, M. T.; Wu, D. T.; Carr, L. D. Graphene Nanoengineering and the Inverse Stone-Thrower-Wales Defect. *Phys. Rev. B* **2010**, *81* (15), 155444.

(98) Robinson, J. T.; Zalalutdinov, M. K.; Cress, C. D.; Culbertson, J. C.; Friedman, A. L.; Merrill, A.; Landi, B. J. Graphene Strained by Defects. *ACS Nano* **2017**, *11* (5), 4745–4752.

(99) Wang, X.; Sun, G.; Routh, P.; Kim, D.-H.; Huang, W.; Chen, P. Heteroatom-Doped Graphene Materials: Syntheses, Properties and Applications. *Chem. Soc. Rev.* **2014**, *43* (20), 7067–7098.

(100) Banhart, F.; Kotakoski, J.; Krasheninnikov, A. V. Structural Defects in Graphene. *ACS Nano* **2011**, *5* (1), 26–41.

(101) Wang, H.; Wang, H.; Chen, Y.; Liu, Y.; Zhao, J.; Cai, Q.; Wang, X. Phosphorus-Doped Graphene and (8, 0) Carbon Nanotube: Structural, Electronic, Magnetic Properties, and Chemical Reactivity. *Appl. Surf. Sci.* **2013**, *273* (2), 302–309.

(102) Yang, Z.; Yao, Z.; Li, G.; Fang, G.; Nie, H.; Liu, Z.; Zhou, X.; Chen, X.; Huang, S. Sulfur-Doped Graphene as an Efficient Metal-Free Cathode Catalyst for Oxygen Reduction. *ACS Nano* **2012**, *6* (1), 205–211.

(103) Morita, R.; Gotoh, K.; Fukunishi, M.; Kubota, K.; Komaba, S.; Nishimura, N.; Yumura, T.; Deguchi, K.; Ohki, S.; Shimizu, T.; Ishida, H. Combination of Solid State NMR and DFT Calculation to Elucidate the State of Sodium in Hard Carbon Electrodes. *J. Mater. Chem. A* **2016**, *4* (34), 13183–13193.

(104) Vicarelli, L.; Heerema, S. J.; Dekker, C.; Zandbergen, H. W. Controlling Defects in Graphene for Optimizing the Electrical Properties of Graphene Nanodevices. *ACS Nano* **2015**, *9* (4), 3428–3435.

(105) Telling, R. H.; Ewels, C. P.; El-Barbary, A. A.; Heggie, M. I. Wigner Defects Bridge the Graphite Gap. *Nat. Mater.* **2003**, *2* (5), 333–337.

(106) Savage, G. *Carbon-Carbon Composites*; Springer Netherlands: Dordrecht, 1993.

(107) Nazri, G.-A.; Pistoia, G. *Lithium Batteries: Science and Technology*; 2009.

(108) Ban, L. L.; Crawford, D.; Marsh, H. Lattice-Resolution Electron Microscopy in Structural Studies of Non-Graphitizing Carbons from Polyvinylidene Chloride (PVDC). *J. Appl. Crystallogr.* **1975**, *8* (4), 415–420.

(109) Townsend, S. J.; Lenosky, T. J.; Muller, D. A.; Nichols, C. S.; Elser, V. Negatively Curved Graphitic Sheet Model of Amorphous Carbon. *Phys. Rev. Lett.* **1992**, *69* (6), 921–924.

(110) Terzyk, A. P.; Furmaniak, S.; Harris, P. J. F.; Gauden, P. A.; Włoch, J.; Kowalczyk, P.; Rychlicki, G. How Realistic Is the Pore Size Distribution Calculated from Adsorption Isotherms If Activated Carbon Is Composed of Fullerene-like Fragments? *Phys. Chem. Chem. Phys.* **2007**, *9* (44), 5919.

(111) Harris, P. J. F.; Tsang, S. C. High-Resolution Electron Microscopy Studies of Non-Graphitizing Carbons. *Philos. Mag. A* **1997**, *76* (3), 667–677.

(112) Dahn, J. R.; Xing, W.; Gao, Y. The “Falling Cards Model” for the Structure of Microporous Carbons. *Carbon N. Y.* **1997**, *35* (6), 825–830.

(113) Harris, P. J. F. Structure of Non-Graphitising Carbons. *Int. Mater. Rev.* **1997**, *42* (5), 206–218.

(114) Xing, W.; Xue, J. S.; Zheng, T.; Gibaud, A.; Dahn, J. R. Correlation Between Lithium Intercalation Capacity and Microstructure in Hard Carbons. *J. Electrochem. Soc.* **1996**, *143* (11), 3482.

(115) Ruthven, D. M. *Principles of Adsorption and Adsorption Processes*; 1984.

(116) Deng, Y.; Dong, S.; Li, Z.; Jiang, H.; Zhang, X.; Ji, X. Applications of Conventional Vibrational Spectroscopic Methods for Batteries Beyond Li-Ion. *Small Methods* **2018**, *2* (8), 1700332.

(117) Zhao, C.; Lu, Y.; Li, Y.; Jiang, L.; Rong, X.; Hu, Y.-S.; Li, H.; Chen, L. Novel Methods for Sodium-Ion Battery Materials. *Small Methods* **2017**, *1* (5), 1600063.

(118) Thommes, M.; Kaneko, K.; Neimark, A. V.; Olivier, J. P.; Rodriguez-Reinoso, F.; Rouquerol, J.; Sing, K. S. W. Physisorption of Gases, with Special Reference to the Evaluation of Surface Area and Pore Size Distribution (IUPAC Technical Report). *Pure Appl. Chem.* **2015**, *87* (9–10), 1051–1069.

(119) Kano, A.; Hojo, N.; Fujimoto, M. Negative-Electrode Active Material for Sodium-Ion Secondary Battery, Method for Manufacturing Said Negative Material, and Sodium-Ion Secondary Battery. US009755237B2, 2017.

(120) Dou, X.; Geng, C.; Buchholz, D.; Passerini, S. Research Update : Hard Carbon with Closed Pores from Pectin-Free Apple Pomace Waste for Na-Ion Batteries. *APL Mater.* **2018**, *6* (4), 047501.

(121) Dou, X.; Hasa, I.; Saurel, D.; Jauregui, M.; Buchholz, D.; Rojo, T.; Passerini, S. Impact of the Acid Treatment on Lignocellulosic Biomass Hard Carbon for Sodium-Ion Battery Anodes. *ChemSusChem* **2018**.

(122) Zheng, F.; Yang, Y.; Chen, Q. High Lithium Anodic Performance of Highly Nitrogen-Doped Porous Carbon Prepared from a Metal-Organic Framework. *Nat. Commun.* **2014**, *5* (May), 1–10.

(123) Xu, D.; Chen, C.; Xie, J.; Zhang, B.; Miao, L.; Cai, J.; Huang, Y.; Zhang, L. A Hierarchical N/S-Codoped Carbon Anode Fabricated Facilely from

Cellulose/Polyaniline Microspheres for High-Performance Sodium-Ion Batteries. *Adv. Energy Mater.* **2016**, *6* (6), 1–7.

(124) Zhang, S. W.; Lv, W.; Luo, C.; You, C. H.; Zhang, J.; Pan, Z. Z.; Kang, F. Y.; Yang, Q. H. Commercial Carbon Molecular Sieves as a High Performance Anode for Sodium-Ion Batteries. *Energy Storage Mater.* **2016**, *3*.

(125) Jian, Z.; Hwang, S.; Li, Z.; Hernandez, A. S.; Wang, X.; Xing, Z.; Su, D.; Ji, X. Hard–Soft Composite Carbon as a Long-Cycling and High-Rate Anode for Potassium-Ion Batteries. *Adv. Funct. Mater.* **2017**, *27* (26), 1–6.

(126) Wang, M.; Yang, Y.; Yang, Z.; Gu, L.; Chen, Q.; Yu, Y. Sodium-Ion Batteries: Improving the Rate Capability of 3D Interconnected Carbon Nanofibers Thin Film by Boron, Nitrogen Dual-Doping. *Adv. Sci.* **2017**, *4* (4).

(127) Shenderova, O. A.; Zhirnov, V. V.; Brenner, D. W. Carbon Nanostructures. *Crit. Rev. Solid State Mater. Sci.* **2002**, *27* (3–4), 227–356.

(128) Marsh, H.; Crawford, D. Structure in Graphitizable Carbon from Coal-Tar Pitch HTT 750–1148 K. Studied Using High Resolution Electron Microscopy. *Carbon N. Y.* **1984**, *22* (4–5), 413–422.

(129) Shinn, J. H. From Coal to Single-Stage and Two-Stage Products : A Reactive Model of Coal Structure. *Fuel* **1984**, *63*, 1187–1196.

(130) Kvick, Å. X-Ray Diffraction, Materials Science Applications. *Encycl. Spectrosc. Spectrom.* **2017**, 648–655.

(131) Iwashita, N. *X-Ray Powder Diffraction*; Tsinghua University Press Limited., 2016.

(132) Cowlard, F. C.; Lewis, J. C. Vitreous Carbon — A New Form of Carbon. *J. Mater. Sci.* **1967**, *2* (6), 507–512.

(133) Warren, B. E. X-Ray Diffraction in Random Layer Lattices. *Phys. Rev.* **1941**, *59* (9), 693–698.

(134) Lipson, H.; Langford, J. I.; Hu, H.-C. Trigonometric Intensity Factors. In *International Tables for Crystallography*; Prince, E., Ed.; International Union of Crystallography: Chester, England, 2006; Vol. C, pp 596–598.

(135) Bommier, C.; Surta, T. W.; Dolgos, M.; Ji, X. New Mechanistic Insights on Na-Ion Storage in Nongraphitizable Carbon. *Nano Lett.* **2015**, *15* (9), 5888–5892.

(136) Kipling, J. J.; Sherwood, J. N.; Shooter, P. V.; Thompson, N. R. Factors Influencing the Graphitization of Polymer Carbons. *Carbon N. Y.* **1964**, *1* (3), 315–320.

(137) Stevens, D. A.; Dahn, J. R. An In Situ Small-Angle X-Ray Scattering Study of Sodium Insertion into a Nanoporous Carbon Anode Material within an Operating Electrochemical Cell. *J. Electrochem. Soc.* **2000**, *147* (12), 4428–4431.

(138) Glatter, V. O.; Kratky, O. Small Angle X-Ray Scattering. *Small Angle X-ray Scatt.* **1982**, *36* (5), 1985.

(139) Porod, G. Die Roentgenkleinwinkelstreuung von Dichtgepackten Kolloiden Systemen - I. Teil. *Kolloid-Zeitschrift* **1951**, *124* (2), 83–114.

(140) Gibaud, A.; Xue, J. S.; Dahn, J. R. A Small Angle X-Ray Scattering Study of Carbons Made from Pyrolyzed Sugar. *Carbon N. Y.* **1996**, *34* (4), 499–503.

(141) Schroeder, M.; Menne, S.; Ségalini, J.; Saurel, D.; Casas-Cabanas, M.; Passerini, S.; Winter, M.; Balducci, A. Considerations about the Influence of the Structural and Electrochemical Properties of Carbonaceous Materials on the Behavior of Lithium-Ion Capacitors. *J. Power Sources* **2014**, *266*, 250–258.

(142) Prehal, C.; Weingarth, D.; Perre, E.; Lechner, R. T.; Amenitsch, H.; Paris, O.; Presser, V. Tracking the Structural Arrangement of Ions in Carbon Supercapacitor Nanopores Using in Situ Small-Angle X-Ray Scattering. *Energy Environ. Sci.* **2015**, *8* (6), 1725–1735.

(143) Nishikawa, K. Pore Structure Analyses of Carbons by Small-Angle X-Ray Scattering. In *Carbon Alloys*; Elsevier, 2003; pp 175–188.

(144) Stevens, D. A.; Dahn, J. R. High Capacity Anode Materials for Rechargeable Sodium-Ion Batteries. *J. Electrochem. Soc.* **2000**, *147* (4), 1271–1273.

(145) Buiel, E.; Dahn, J. R. Reduction of the Irreversible Capacity in Hard-Carbon Anode Materials Prepared from Sucrose for Li-Ion Batteries. *J. Electrochem. Soc.* **1998**, *145* (6), 1977–1981.

(146) Komaba, S.; Murata, W.; Ishikawa, T.; Yabuuchi, N.; Ozeki, T.; Nakayama, T.; Ogata, A.; Gotoh, K.; Fujiwara, K. Electrochemical Na Insertion and Solid Electrolyte Interphase for Hard-Carbon Electrodes and Application to Na-Ion Batteries. *Adv. Funct. Mater.* **2011**, *21* (20), 3859–3867.

(147) Smith, A. J.; MacDonald, M. J.; Ellis, L. D.; Obrovac, M. N.; Dahn, J. R. A Small Angle X-Ray Scattering and Electrochemical Study of the Decomposition of Wood during Pyrolysis. *Carbon N. Y.* **2012**, *50* (10), 3717–3723.

(148) Dahbi, M.; Kiso, M.; Kubota, K.; Horiba, T.; Chafik, T.; Hida, K.; Matsuyama, T.; Komaba, S. Synthesis of Hard Carbon from Argan Shells for Na-Ion Batteries. *J. Mater. Chem. A* **2017**, *5* (20), 9917–9928.

(149) Simone, V.; Boulineau, A.; de Geyer, A.; Rouchon, D.; Simonin, L.; Martinet, S. Hard Carbon Derived from Cellulose as Anode for Sodium Ion Batteries: Dependence of Electrochemical Properties on Structure. *J. Energy Chem.* **2016**, *25* (5), 761–768.

(150) Morcrette, M.; Chabre, Y.; Vaughan, G.; Amatucci, G.; Leriche, J.-B.; Patoux, S.; Masquelier, C.; Tarascon, J.-M. In Situ X-Ray Diffraction Techniques as a Powerful Tool to Study Battery Electrode Materials. *Electrochim. Acta* **2002**, *47* (19), 3137–3149.

(151) Sharma, N.; Pang, W. K.; Guo, Z.; Peterson, V. K. In Situ Powder Diffraction Studies of Electrode Materials in Rechargeable Batteries. *ChemSusChem* **2015**, *8* (17), 2826–2853.

(152) Luo, W.; Jian, Z.; Xing, Z.; Wang, W.; Bommier, C.; Lerner, M. M.; Ji, X. Electrochemically Expandable Soft Carbon as Anodes for Na-Ion Batteries. *ACS Cent. Sci.* **2015**, *1* (9), 516–522.

(153) Wu, J.-B.; Lin, M.-L.; Cong, X.; Liu, H.-N.; Tan, P.-H. Raman Spectroscopy of Graphene-Based Materials and Its Applications in Related Devices. *Chem. Soc. Rev.* **2018**, 1822–1873.

(154) Marino, C.; Cabanero, J.; Povia, M.; Villevieille, C. Biowaste Lignin-Based Carbonaceous Materials as Anodes for Na-Ion Batteries. *J. Electrochem. Soc.* **2018**, *165* (7), A1400–A1408.

(155) Pimenta, M. A.; Dresselhaus, G.; Dresselhaus, M. S.; Cançado, L. G.; Jorio, A.; Saito, R. Studying Disorder in Graphite-Based Systems by Raman Spectroscopy. *Phys. Chem. Chem. Phys.* **2007**, *9* (11), 1276–1291.

(156) Ferrari, A. C. Raman Spectroscopy of Graphene and Graphite: Disorder, Electron–phonon Coupling, Doping and Nonadiabatic Effects. *Solid State Commun.* **2007**, *143* (1–2), 47–57.

(157) Ferrari, A. C.; Robertson, J. Interpretation of Raman Spectra of Disordered and Amorphous Carbon. *Phys. Rev. B* **2000**, *61* (20), 14095–14107.

(158) Bokobza, L.; Bruneel, J.-L.; Couzi, M. Raman Spectra of Carbon-Based Materials (from Graphite to Carbon Black) and of Some Silicone Composites. *C* **2015**, *1* (1), 77–94.

(159) Knight, D. S.; White, W. B. Characterization of Crystalline Quality of Diamond Films by Raman Spectroscopy. *J. Mater. Res.* **1989**, *4* (2), 385–393.

(160) Caŋado, L. G.; Takai, K.; Enoki, T.; Endo, M.; Kim, Y. A.; Mizusaki, H.; Jorio, A.; Coelho, L. N.; Magalhães-Paniago, R.; Pimenta, M. A. General Equation for the Determination of the Crystallite Size La of Nanographite by Raman Spectroscopy. *Appl. Phys. Lett.* **2006**, *88* (16), 2–5.

(161) Vázquez-Santos, M. B.; Geissler, E.; László, K.; Rouzaud, J. N.; Martínez-Alonso, A.; Tascón, J. M. D. Comparative XRD, Raman, and TEM Study on Graphitization of PBO-Derived Carbon Fibers. *J. Phys. Chem. C* **2012**, *116* (1), 257–268.

(162) Sadezky, A.; Muckenhuber, H.; Grothe, H.; Niessner, R.; Pöschl, U. Raman Microspectroscopy of Soot and Related Carbonaceous Materials: Spectral Analysis and Structural Information. *Carbon N. Y.* **2005**, *43* (8), 1731–1742.

(163) Herdman, J. D.; Connelly, B. C.; Smooke, M. D.; Long, M. B.; Miller, J. H. A Comparison of Raman Signatures and Laser-Induced Incandescence with Direct Numerical Simulation of Soot Growth in Non-Premixed Ethylene/Air Flames. *Carbon N. Y.* **2011**, *49* (15), 5298–5311.

(164) Ding, J.; Wang, H.; Li, Z.; Kohandehghan, A.; Cui, K.; Xu, Z.; Zahiri, B.; Tan, X.; Lotfabad, E. M.; Olsen, B. C.; Mitlin, D. Carbon Nanosheet Frameworks Derived from Peat Moss as High Performance Sodium Ion Battery Anodes. *ACS Nano* **2013**, *7* (12), 11004–11015.

(165) Gupta, A. K.; Nisoli, C.; Lammert, P. E.; Crespi, V. H.; Eklund, P. C. Curvature-Induced D-Band Raman Scattering in Folded Graphene. *J. Phys. Condens. Matter* **2010**, *22* (33).

(166) Vaalma, C.; Buchholz, D.; Weil, M.; Passerini, S. A Cost and Resource Analysis of Sodium-Ion Batteries. *Nat. Rev. Mater.* **2018**, *3*, 18013.

(167) Peters, J.; Buchholz, D.; Passerini, S.; Weil, M. Life Cycle Assessment of Sodium-Ion Batteries. *Energy Environ. Sci.* **2016**, *9* (5), 1744–1751.

(168) Streets, D. G.; Yarber, K. F.; Woo, J.-H.; Carmichael, G. R. Biomass Burning in Asia: Annual and Seasonal Estimates and Atmospheric Emissions. *Global Biogeochem. Cycles* **2003**, *17* (4), 1099.

(169) Yevich, R.; Logan, J. A. An Assessment of Biofuel Use and Burning of Agricultural Waste in the Developing World. *Global Biogeochem. Cycles* **2003**, *17* (4), 1–5.

(170) Huang, R. J.; Zhang, Y.; Bozzetti, C.; Ho, K. F.; Cao, J. J.; Han, Y.; Daellenbach, K. R.; Slowik, J. G.; Platt, S. M.; Canonaco, F.; Zotter, P.; Wolf, R.; Pieber, S. M.; Bruns, E. A.; Crippa, M.; Ciarelli, G.; Piazzalunga, A.; Schwikowski, M.; Abbaszade, G.; Schnelle-Kreis, J.; Zimmermann, R.; An, Z.; Szidat, S.; Baltensperger, U.; El Haddad, I.; Prevot, A. S. High Secondary Aerosol Contribution to Particulate Pollution during Haze Events in China. *Nature* **2014**, *514* (7521), 218–222.

(171) Zhu, X.; Jiang, X.; Liu, X.; Xiao, L.; Cao, Y. A Green Route to Synthesize Low-Cost and High-Performance Hard Carbon as Promising Sodium-Ion Battery Anodes from Sorghum Stalk Waste. *Green Energy Environ.* **2017**, *2* (3), 310–315.

(172) Górka, J.; Vix-Guterl, C.; Matei Ghimbeu, C. Recent Progress in Design of Biomass-Derived Hard Carbons for Sodium Ion Batteries. *C* **2016**, *2* (4), 24.

(173) Lv, W.; Wen, F.; Xiang, J.; Zhao, J.; Li, L.; Wang, L.; Liu, Z.; Tian, Y. Peanut Shell Derived Hard Carbon as Ultralong Cycling Anodes for Lithium and Sodium Batteries. *Electrochim. Acta* **2015**, *176*, 533–541.

(174) Wang, K.; Jin, Y.; Sun, S.; Huang, Y.; Peng, J.; Luo, J.; Zhang, Q.; Qiu, Y.; Fang, C.; Han, J. Low-Cost and High-Performance Hard Carbon Anode Materials for Sodium-Ion Batteries. *ACS Omega* **2017**, *2* (4), 1687–1695.

(175) Wu, L.; Buchholz, D.; Vaalma, C.; Giffin, G. A.; Passerini, S. Apple-Biowaste-Derived Hard Carbon as a Powerful Anode Material for Na-Ion Batteries. *ChemElectroChem* **2016**, *3* (2), 292–298.

(176) Hong, K.; Qie, L.; Zeng, R.; Yi, Z.; Zhang, W.; Wang, D.; Yin, W.; Wu, C.; Fan, Q.; Zhang, W.; Huang, Y. Biomass Derived Hard Carbon Used as a High Performance Anode Material for Sodium Ion Batteries. *J. Mater. Chem. A* **2014**, *2* (32), 12733.

(177) Gaddam, R. R.; Yang, D.; Narayan, R.; Raju, K. V. S. N.; Kumar, N. A.; Zhao, X. S. Biomass Derived Carbon Nanoparticle as Anodes for High Performance Sodium and Lithium Ion Batteries. *Nano Energy* **2016**, *26*, 346–352.

(178) Tang, W.; Zhang, Y.; Zhong, Y.; Shen, T.; Wang, X.; Xia, X.; Tu, J. Natural Biomass-Derived Carbons for Electrochemical Energy Storage. *Mater. Res. Bull.* **2017**, *88*, 234–241.

(179) Li, Y.; Xu, S.; Wu, X.; Yu, J.; Wang, Y.; Hu, Y.-S.; Li, H.; Chen, L.; Huang, X. Amorphous Monodispersed Hard Carbon Micro-Spherules Derived from Biomass as a High Performance Negative Electrode Material for Sodium-Ion Batteries. *J. Mater. Chem. A* **2015**, *3* (1), 71–77.

(180) Zhang, N.; Liu, Q.; Chen, W.; Wan, M.; Li, X.; Wang, L.; Xue, L.; Zhang, W. High Capacity Hard Carbon Derived from Lotus Stem as Anode for Sodium Ion Batteries. *J. Power Sources* **2018**, *378* (December 2017), 331–337.

(181) Sen, S.; Patil, S.; Argyropoulos, D. S. Thermal Properties of Lignin in Copolymers, Blends, and Composites: A Review. *Green Chem.* **2015**, *17* (11), 4862–4887.

(182) Upton, B. M.; Kasko, A. M. Strategies for the Conversion of Lignin to High-Value Polymeric Materials: Review and Perspective. *Chem. Rev.* **2016**, *116* (4), 2275–2306.

(183) Kai, D.; Tan, M. J.; Chee, P. L.; Chua, Y. K.; Yap, Y. L.; Loh, X. J. Towards Lignin-Based Functional Materials in a Sustainable World. *Green Chem.* **2016**, *18* (5), 1175–1200.

(184) Wang, S.; Dai, G.; Yang, H.; Luo, Z. Lignocellulosic Biomass Pyrolysis Mechanism: A State-of-the-Art Review. *Prog. Energy Combust. Sci.* **2017**, *62*, 33–86.

(185) IOANNIDOU, O.; ZABANIOTOU, A. Agricultural Residues as Precursors for Activated Carbon Production—A Review. *Renew. Sustain. Energy Rev.* **2007**, *11* (9), 1966–2005.

(186) Zhang, H.; Zhang, W.; Ming, H.; Pang, J.; Zhang, H.; Cao, G.; Yang, Y. Design Advanced Carbon Materials from Lignin-Based Interpenetrating Polymer Networks for High Performance Sodium-Ion Batteries. *Chem. Eng. J.* **2018**, *341*, 280–288.

(187) Saavedra Rios, C. del M.; Simone, V.; Simonin, L.; Martinet, S.; Dupont, C. Biochars from Various Biomass Types as Precursors for Hard Carbon Anodes in Sodium-Ion Batteries. *Biomass and Bioenergy* **2018**, *117* (July), 32–37.

(188) Alonso, D. M.; Wettstein, S. G.; Dumesic, J. A. Bimetallic Catalysts for Upgrading of Biomass to Fuels and Chemicals. *Chem. Soc. Rev.* **2012**, *41* (24), 8075–8098.

(189) Baldinelli, A.; Dou, X.; Buchholz, D.; Marinaro, M.; Passerini, S.; Barelli, L. Addressing the Energy Sustainability of Biowaste-Derived Hard Carbon Materials for Battery Electrodes. *Green Chem.* **2018**, *20* (7), 1527–1537.

(190) Jin, Y.; Sun, S.; Ou, M.; Liu, Y.; Fan, C.; Sun, X.; Peng, J.; Li, Y.; Qiu, Y.; Wei, P.; Deng, Z.; Xu, Y.; Han, J.; Huang, Y. High-Performance Hard Carbon Anode: Tunable Local Structures and Sodium Storage Mechanism. *ACS Appl. Energy Mater.* **2018**, acsaem.8b00354.

(191) Bai, P.; He, Y.; Zou, X.; Zhao, X.; Xiong, P.; Xu, Y. Elucidation of the Sodium-Storage Mechanism in Hard Carbons. *Adv. Energy Mater.* **2018**, *1703217*, 1703217.

(192) Matei Ghimbeu, C.; Górka, J.; Simone, V.; Simonin, L.; Martinet, S.; Vix-Guterl, C. Insights on the Na+ion Storage Mechanism in Hard Carbon: Discrimination between the Porosity, Surface Functional Groups and Defects. *Nano Energy* **2018**, *44* (October 2017), 327–335.

(193) Wu, C. M.; Pan, P. I.; Cheng, Y. W.; Liu, C. P.; Chang, C. C.; Avdeev, M.; Lin, S. kang. The Mechanism of the Sodiation and Desodiation in Super P Carbon Electrode for Sodium-Ion Battery. *J. Power Sources* **2017**, *340*, 14–21.

(194) Qiao, Y.; Ma, M.; Liu, Y.; Li, S.; Lu, Z.; Yue, H.; Dong, H.; Cao, Z.; Yin, Y.; Yang, S. First-Principles and Experimental Study of Nitrogen/Sulfur Co-Doped Carbon Nanosheets as Anodes for Rechargeable Sodium Ion Batteries. *J. Mater. Chem. A* **2016**, *4* (40), 15565–15574.

(195) Li, Z.; Ma, L.; Surta, T. W.; Bommier, C.; Jian, Z.; Xing, Z.; Stickle, W. F.; Dolgos, M.; Amine, K.; Lu, J.; Wu, T.; Ji, X. High Capacity of Hard Carbon Anode in Na-Ion Batteries Unlocked by $PO_x$ Doping. *ACS Energy Lett.* **2016**, 395–401.

(196) Wang, S.; Kakumoto, T.; Matsumura, Y. Mechanism of Lithium Insertion into Disordered Carbon. *Synth. Met.* **1999**, *103*, 2308–2309.

(197) Wu, Y.; Wan, C.; Jiang, C.; Fang, S.; Jiang, Y. Mechanism of Lithium Storage in Low Temperature Carbon. *Carbon N. Y.* **1999**, *37*, 1901–1908.

(198) Xiang, H.; Fang, S.; Jiang, Y. Mechanism of Lithium Insertion in Carbons Pyrolyzed at Low Temperature. *Chinese Sci. Bull.* **1999**, *44* (5), 385–390.

(199) Sato, K.; Noguchi, M.; Demachi, A.; Oki, N.; Endo, M. A Mechanism of Lithium Storage in Disordered Carbons. *Science (80-. ).* **1994**, *264* (5158), 556–558.

(200) Xiao, L.; Cao, Y. Delineating Adsorption-Insertion Mechanism in Hard Carbon Materials for Sodium Ion Storage. *Meet. Abstr. 2017-02 486* **2017**.

(201) Elia, G. A.; Hasa, I.; Hassoun, J. Characterization of a Reversible, Low-Polarization Sodium-Oxygen Battery. *Electrochim. Acta* **2016**, *191*, 516–520.

(202) Adelhelm, P.; Hartmann, P.; Bender, C. L.; Busche, M.; Eufinger, C.; Janek, J. From Lithium to Sodium: Cell Chemistry of Room Temperature Sodium–air and Sodium–sulfur Batteries. *Beilstein J. Nanotechnol.* **2015**, *6*, 1016–1055.

(203) Marsh, H.; Wynne-Jones, W. F. K. THE SURFACE PROPERTIES OF CARBON-I THE EFFECT OF ACTIVATED DIFFUSION. *Carbon N. Y.* **1964**, *1*, 269–279.

(204) Tsai, P.; Chung, S.-C.; Lin, S.; Yamada, A. Ab Initio Study of Sodium Intercalation into Disordered Carbon. *J. Mater. Chem. A* **2015**, *3* (18), 9763–9768.

(205) Ragauskas, A. J.; Williams, C. K.; Davison, B. H.; Britovsek, G.; Cairney, J.; Eckert, C. A.; Frederick, W. J.; Hallett, J. P.; Leak, D. J.; Liotta, C. L.; Mielenz,

J. R.; Murphy, R.; Templer, R.; Tschaplinski, T. The Path Forward for Biofuels and Biomaterials. *Science* **2006**, *311* (5760), 484–489.

(206) Huber, G. W.; Iborra, S.; Corma, A. Synthesis of Transportation Fuels from Biomass: Chemistry, Catalysts, and Engineering. *Chem. Rev.* **2006**, *106* (9), 4044–4098.

(207) United Nations Environmental Programme. *Converting Waste Agricultural Biomass into a Resource*; 2009.

(208) Pan, H.; Hu, Y.-S.; Chen, L. Room-Temperature Stationary Sodium-Ion Batteries for Large-Scale Electric Energy Storage. *Energy Environ. Sci.* **2013**, *6* (8), 2338–2360.

(209) Irisarri, E.; Ponrouch, A.; Palacin, M. R. Review—Hard Carbon Negative Electrode Materials for Sodium-Ion Batteries. *J. Electrochem. Soc.* **2015**, *162* (14), A2476–A2482.

(210) Wang, L.; Schnepp, Z.; Titirici, M. M. Rice Husk-Derived Carbon Anodes for Lithium Ion Batteries. *J. Mater. Chem. A* **2013**, *1* (17), 5269–5273.

(211) Ou, J.; Zhang, Y.; Chen, L.; Zhao, Q.; Meng, Y.; Guo, Y.; Xiao, D. Nitrogen-Rich Porous Carbon Derived from Biomass as a High Performance Anode Material for Lithium Ion Batteries. *J. Mater. Chem. A* **2015**, *3* (12), 6534–6541.

(212) Gibson, L. J. The Hierarchical Structure and Mechanics of Plant Materials. *J. R. Soc. Interface* **2012**, *9* (76), 2749–2766.

(213) Sun, Y.; Cheng, J. Hydrolysis of Lignocellulosic Materials for Ethanol Production: A Review. *Bioresour. Technol.* **2002**, *83* (1), 1–11.

(214) Nawirska, A.; Kwaśniewska, M. Dietary Fibre Fractions from Fruit and Vegetable Processing Waste. *Food Chem.* **2005**, *91* (2), 221–225.

(215) Tanyildizi, M. Ş. Modeling of Adsorption Isotherms and Kinetics of Reactive Dye from Aqueous Solution by Peanut Hull. *Chem. Eng. J.* **2011**, *168* (3), 1234–1240.

(216) Shaukat, S. S. *Progress in Biomass and Bioenergy Production*; 2011.

(217) Qin, W.; Wu, L.; Zheng, Z.; Dong, C.; Yang, Y. Lignin Hydrolysis and Phosphorylation Mechanism during Phosphoric Acid-Acetone Pretreatment: A DFT Study. *Molecules* **2014**, *19* (12), 21335–21349.

(218) Kim, C.; Yang, K. S.; Kojima, M.; Yoshida, K.; Kim, Y. J.; Kim, Y. A.; Endo, M. Fabrication of Electrospinning-Derived Carbon Nanofiber Webs for the Anode Material of Lithium-Ion Secondary Batteries. *Adv. Funct. Mater.* **2006**, *16* (18), 2393–2397.

(219) Gass, M. H.; Bangert, U.; Bleloch, A. L.; Wang, P.; Nair, R. R.; Geim, a K. Free-Standing Graphene at Atomic Resolution. *Nat. Nanotechnol.* **2008**, *3* (11), 676–681.

(220) Li, W.; Zeng, L.; Yang, Z.; Gu, L.; Wang, J.; Liu, X.; Cheng, J.; Yu, Y. Free-Standing and Binder-Free Sodium-Ion Electrodes with Ultralong Cycle Life and

High Rate Performance Based on Porous Carbon Nanofibers. *Nanoscale* **2014**, *6* (2), 693–698.

(221) Eshetu, G. G.; Diemant, T.; Grugeon, S.; Behm, R. J.; Laruelle, S.; Armand, M.; Passerini, S. In-Depth Interfacial Chemistry and Reactivity Focused Investigation of Lithium-Imide- and Lithium-Imidazole-Based Electrolytes. *ACS Appl. Mater. Interfaces* **2016**, *8* (25), 16087–16100.

(222) Qi, X.; Blizanac, B.; DuPasquier, A.; Lal, A.; Niehoff, P.; Placke, T.; Oljaca, M.; Li, J.; Winter, M. Influence of Thermal Treated Carbon Black Conductive Additive on the Performance of High Voltage Spinel Cr-Doped LiNi0.5Mn1.5O4 Composite Cathode Electrode. *J. Electrochem. Soc.* **2015**, *162* (3), A339–A343.

(223) Mérel, P.; Tabbal, M.; Chaker, M.; Moisa, S.; Margot, J. Direct Evaluation of the Sp3 Content in Diamond-like-Carbon Films by XPS. *Appl. Surf. Sci.* **1998**, *136* (1–2), 105–110.

(224) Xing, W. Study of Irreversible Capacities for Li Insertion in Hard and Graphitic Carbons. *J. Electrochem. Soc.* **1997**, *144* (4), 1195.

(225) Vogt, L. O.; El Kazzi, M.; Jämstorp Berg, E.; Pérez Villar, S.; Novák, P.; Villevieille, C. Understanding the Interaction of the Carbonates and Binder in Na-Ion Batteries: A Combined Bulk and Surface Study. *Chem. Mater.* **2015**, *27* (4), 1210–1216.

(226) Bakandritsos, A.; Steriotis, T.; Petridis, D. High Surface Area Montmorillonite - Carbon Composites and Derived Carbons. *Chem. Mater* **2004**, *143* (10), 1551–1559.

(227) Li, Y.; Hu, Y. S.; Qi, X.; Rong, X.; Li, H.; Huang, X.; Chen, L. Advanced Sodium-Ion Batteries Using Superior Low Cost Pyrolyzed Anthracite Anode: Towards Practical Applications. *Energy Storage Mater.* **2016**, *5*, 191–197.

(228) Liu, P.; Li, Y.; Hu, Y.-S.; Li, H.; Chen, L.; Huang, X. A Waste Biomass Derived Hard Carbon as a High-Performance Anode Material for Sodium-Ion Batteries. *J. Mater. Chem. A* **2016**, *4* (34), 13046–13052.

(229) Canteri-Schemin, M. H.; Fertonani, H. C. R.; Waszczynskyj, N.; Wosiacki, G. Extraction of Pectin from Apple Pomace. *Brazilian Arch. Biol. Technol.* **2005**, *48* (2), 259–266.

(230) Du, S.; Yang, H.; Qian, K.; Wang, X.; Chen, H. Fusion and Transformation Properties of the Inorganic Components in Biomass Ash. *Fuel* **2014**, *117* (PARTB), 1281–1287.

(231) Sing, K. S. W. Reporting Physisorption Data for Gas/Solid Systems with Special Reference to the Determination of Surface Area and Porosity (Recommendations 1984). *Pure Appl. Chem.* **1985**, *57* (4), 603–619.

(232) Chu, S.; Majumdar, A. Opportunities and Challenges for a Sustainable Energy Future. *Nature* **2012**, *488* (7411), 294–303.

(233) Armand, M.; Tarascon, J.-M. Building Better Batteries. *Nature* **2008**, *451* (7179), 652–657.

(234) Tarascon, J. M.; Armand, M. Issues and Challenges Facing Rechargeable Lithium Batteries. *Nature* **2001**, *414* (6861), 359–367.

(235) Yao, F.; Pham, D. T.; Lee, Y. H. Carbon-Based Materials for Lithium-Ion Batteries, Electrochemical Capacitors, and Their Hybrid Devices. *ChemSusChem* **2015**, *8* (14), 2284–2311.

(236) Vaalma, C.; Giffin, G. A.; Buchholz, D.; Passerini, S. Non-Aqueous K-Ion Battery Based on Layered K 0.3 MnO 2 and Hard Carbon/Carbon Black. *J. Electrochem. Soc.* **2016**, *163* (7), 1295–1299.

(237) Chen, X.; Paul, R.; Dai, L. Carbon-Based Supercapacitors for Efficient Energy Storage. *Natl. Sci. Rev.* **2017**, *4* (3), 453–489.

(238) Lee, B.; Ko, Y.; Kwon, G.; Lee, S.; Ku, K.; Kim, J. Exploiting Biological Systems : Toward Eco-Friendly and High-Efficiency Rechargeable Batteries. *Joule* **2018**, *2* (1), 61–75.

(239) Sanderson, K. Lignocellulose: A Chewy Problem. *Nature* **2011**, *474* (7352 SUPPL.).

(240) Himmel, M. E.; Ding, S.-Y.; Johnson, D. K.; Adney, W. S.; Nimlos, M. R.; Brady, J. W.; Foust, T. D. Biomass Recalcitrance: Engineering Plants and Enzymes for Biofuels Production. *Science (80-. ).* **2007**, *315* (5813), 804–807.

(241) Alonso, D. M.; Hakim, S. H.; Zhou, S.; Won, W.; Hosseinaei, O.; Tao, J.; Garcia-Negron, V.; Motagamwala, A. H.; Mellmer, M. A.; Huang, K.; Houtman, C. J.; Labbé, N.; Harper, D. P.; Maravelias, C.; Runge, T.; Dumesic, J. A. Increasing the Revenue from Lignocellulosic Biomass: Maximizing Feedstock Utilization. *Sci. Adv.* **2017**, *3* (5), e1603301.

(242) Mohamad Nor, N.; Lau, L. C.; Lee, K. T.; Mohamed, A. R. Synthesis of Activated Carbon from Lignocellulosic Biomass and Its Applications in Air Pollution Control—a Review. *J. Environ. Chem. Eng.* **2013**, *1* (4), 658–666.

(243) Lu, H.; Zhao, X. S. Biomass-Derived Carbon Electrode Materials for Supercapacitors. *Sustain. Energy Fuels* **2017**, *1*, 1265–1281.

(244) Enock, T. K.; King'ondu, C. K.; Pogrebnoi, A.; Jande, Y. A. C. Status of Biomass Derived Carbon Materials for Supercapacitor Application. *Int. J. Electrochem.* **2017**, *2017*, 1–14.

(245) Wang, J.; Nie, P.; Ding, B.; Dong, S.; Hao, X.; Dou, H.; Zhang, X. Biomass Derived Carbon for Energy Storage Devices. *J. Mater. Chem. A* **2017**, *5* (6), 2411–2428.

(246) Gao, Z.; Zhang, Y.; Song, N.; Li, X. Biomass-Derived Renewable Carbon Materials for Electrochemical Energy Storage. *Mater. Res. Lett.* **2017**, *5* (2), 69–88.

(247) Kim, H.; Hong, J.; Yoon, G.; Kim, H.; Park, K.-Y.; Park, M.-S.; Yoon, W.-S.; Kang, K. Sodium Intercalation Chemistry in Graphite. *Energy Environ. Sci.* **2015**, *8* (10), 2963–2969.

(248) Palomares, V.; Serras, P.; Villaluenga, I.; Hueso, K. B.; Carretero-Gonzalez, J.; Rojo, T. Na-Ion Batteries, Recent Advances and Present Challenges to

Become Low Cost Energy Storage Systems. *Energy Environ. Sci.* **2012**, *5* (3), 5884–5901.

(249) Wang, H.; Yu, W.; Shi, J.; Mao, N.; Chen, S.; Liu, W. Biomass Derived Hierarchical Porous Carbons as High-Performance Anodes for Sodium-Ion Batteries. *Electrochim. Acta* **2016**, *188*, 103–110.

(250) Tenhaeff, W. E.; Rios, O.; More, K.; McGuire, M. A. Highly Robust Lithium Ion Battery Anodes from Lignin: An Abundant, Renewable, and Low-Cost Material. *Adv. Funct. Mater.* **2014**, *24* (1), 86–94.

(251) Li, Y.; Hu, Y.-S.; Titirici, M.-M.; Chen, L.; Huang, X. Hard Carbon Microtubes Made from Renewable Cotton as High-Performance Anode Material for Sodium-Ion Batteries. *Adv. Energy Mater.* **2016**, *6* (18), 1600659.

(252) Roberts, A. D.; Li, X.; Zhang, H. Porous Carbon Spheres and Monoliths: Morphology Control, Pore Size Tuning and Their Applications as Li-Ion Battery Anode Materials. *Chem. Soc. Rev.* **2014**, *43* (13), 4341–4356.

(253) Li, Z.; Ma, L.; Surta, T. W.; Bommier, C.; Jian, Z.; Xing, Z.; Stickle, W. F.; Dolgos, M.; Amine, K.; Lu, J.; Wu, T.; Ji, X. High Capacity of Hard Carbon Anode in Na-Ion Batteries Unlocked by $PO_x$ Doping. *ACS Energy Lett.* **2016**, *1* (2), 395–401.

(254) Xing, Z.; Qi, Y.; Tian, Z.; Xu, J.; Yuan, Y.; Bommier, C.; Lu, J.; Tong, W.; Jiang, D. E.; Ji, X. Identify the Removable Substructure in Carbon Activation. *Chem. Mater.* **2017**, *29* (17), 7288–7295.

(255) Li, Z.; Jian, Z.; Wang, X.; Rodríguez-Pérez, I. A.; Bommier, C.; Ji, X. Hard Carbon Anodes of Sodium-Ion Batteries: Undervalued Rate Capability. *Chem. Commun.* **2017**, *53* (17), 2610–2613.

(256) Zhu, Y.-E.; Yang, L.; Zhou, X.; Li, F.; Wei, J.; Zhou, Z. Boosting the Rate Capability of Hard Carbon with an Ether-Based Electrolyte for Sodium Ion Batteries. *J. Mater. Chem. A* **2017**, *5* (20), 9528–9532.

(257) Bai, P.; He, Y.; Xiong, P.; Zhao, X.; Xu, K.; Xu, Y. Long Cycle Life and High Rate Sodium-Ion Chemistry for Hard Carbon Anodes. *Energy Storage Mater.* **2018**.

(258) Brown, P.; Atly Jefcoat, I.; Parrish, D.; Gill, S.; Graham, E. Evaluation of the Adsorptive Capacity of Peanut Hull Pellets for Heavy Metals in Solution. *Adv. Environ. Res.* **2000**, *4* (1), 19–29.

(259) Zhang, Y.-H. P.; Ding, S.-Y.; Mielenz, J. R.; Cui, J.-B.; Elander, R. T.; Laser, M.; Himmel, M. E.; McMillan, J. R.; Lynd, L. R. Fractionating Recalcitrant Lignocellulose at Modest Reaction Conditions. *Biotechnol. Bioeng.* **2007**, *97* (2), 214–223.

(260) Emmerich, F. G. Evolution with Heat Treatment of Crystallinity in Carbons. *Carbon N. Y.* **1995**, *33* (12), 1709–1715.

(261) Ding, J.; Wang, H.; Li, Z.; Cui, K.; Karpuzov, D.; Tan, X.; Kohandehghan, A.; Mitlin, D. Peanut Shell Hybrid Sodium Ion Capacitor with Extreme Energy-Power Rivals Lithium Ion Capacitors. *Energy Environ. Sci.* **2015**, *8* (3), 941–955.

(262) Baquero, M. C.; Giraldo, L.; Moreno, J. C.; Suárez-García, F.; Martínez-Alonso, A.; Tascón, J. M. D. Activated Carbons by Pyrolysis of Coffee Bean Husks in Presence of Phosphoric Acid. *J. Anal. Appl. Pyrolysis* **2003**, *70* (2), 779–784.

(263) Buiel, E. On the Reduction of Lithium Insertion Capacity in Hard-Carbon Anode Materials with Increasing Heat-Treatment Temperature. *J. Electrochem. Soc.* **1998**, *145* (7), 2252.

(264) Kipling, J. J.; Sherwood, J. N.; Shooter, P. V.; Thompson, N. R. The Pore Structure and Surface Area of High-Temperature Polymer Carbons. *Carbon N. Y.* **1964**, *1* (3), 321–328.

(265) Suárez-García, F.; Martínez-Alonso, A.; Tascón, J. M. . Porous Texture of Activated Carbons Prepared by Phosphoric Acid Activation of Apple Pulp. *Carbon N. Y.* **2001**, *39* (7), 1111–1115.

(266) Molina-Sabio, M.; RodRíguez-Reinoso, F.; Caturla, F.; Sellés, M. J. Porosity in Granular Carbons Activated with Phosphoric Acid. *Carbon N. Y.* **1995**, *33* (8), 1105–1113.

(267) Hasegawa, G.; Kanamori, K.; Kannari, N.; Ozaki, J. ichi; Nakanishi, K.; Abe, T. Hard Carbon Anodes for Na-Ion Batteries: Toward a Practical Use. *ChemElectroChem* **2015**, *2* (12), 1917–1920.

(268) Bommier, C.; Leonard, D.; Jian, Z.; Stickle, W. F.; Greaney, P. A.; Ji, X. New Paradigms on the Nature of Solid Electrolyte Interphase Formation and Capacity Fading of Hard Carbon Anodes in Na-Ion Batteries. *Adv. Mater. Interfaces* **2016**, *3* (19), 1–10.

(269) Ponrouch, A.; Marchante, E.; Courty, M.; Tarascon, J.-M.; Palacín, M. R. In Search of an Optimized Electrolyte for Na-Ion Batteries. *Energy Environ. Sci.* **2012**, *5* (9), 8572.

(270) Mueller, F.; Bresser, D.; Paillard, E.; Winter, M.; Passerini, S. Influence of the Carbonaceous Conductive Network on the Electrochemical Performance of ZnFe2O4 Nanoparticles. *J. Power Sources* **2013**, *236*, 87–94.